Title
Toward the Space-Time Limit

Author
Rios, Laura

Publication Date
2017

UNIVERSITY OF CALIFORNIA,
IRVINE

Toward the Space-Time Limit

DISSERTATION

submitted in partial satisfaction of the requirements
for the degree of

DOCTOR OF PHILOSOPHY

in Chemistry

by

Laura Rios

Dissertation Committee:
Professor V. Ara Apkarian, Chair
Associate Professor Eric O. Potma
Associate Professor Matthew D. Law

2017

DEDICATION

For

Professor W.C. Herndon, who taught me that spinning in an office chair
while snacking on cherries is the best way to discuss science.

and

Nick A. Valilis, whose best was never so good he could not conceive a better.
Your indomitable spirit has propelled me through graduate school.
We miss you very much.

⋱

Though she be but little, she is fierce!
A Midsummer's Night's Dream, Act 3, scene ii

⋱

This is presented as a work of fiction and is dedicated to nobody.
Charles Bukowski

TABLE OF CONTENTS

LIST OF FIGURES

Page

LIST OF TABLES

Page

ACKNOWLEDGMENTS

I would like to thank the following wonderful people, whose contributions to this work are so immense, they cannot be quantified with even the most precise of lasers.

Mi familia: Mami, Vati, Gegi, Alis, and Nani.

My friends: Alison O'Connor, Kate Rodriguez, Nuri and Nick Valilis, Micah Ellowitz, Adriana and Manny Quiñones, Alex Knaust, Erin Alcorn, Alba Alfonso García, Trenton Salk, Katie Kirby and Marco Allodi, Kevin Crampton, Lindsay Cameron, Lisa Olshanky, Prasoon Saurabh, Nick Broten, Ingmar Saberi, Nat Kadunce, Julia Hammond, Joanna Yau, Claire Gilpin, Natasha Kozlyuk, Sarah Garcia, Xuan Mei, and Ian Walker.

My better half: Dr. Ian Finneran. I look forward to a lifetime of (accidentally) tickling your feet, and dragging the cats off your pillow. Te quiero.

I would also like to thank my exceptional lab partners, Nicholas Tallarida and Dr. Joonhee Lee. Without their help, these very difficult experiments would have been impossible to undertake. Joonhee's guidance and Nick's insightful questions have greatly aided me throughout my graduate career. Joonhee, Nick, and myself worked together to collect the data and create the figure in Chapter 2. Joonhee and Dr. Shawn Perdue took the initial data that prompted our follow-up measurements. Figures 2.3, 2.4, 2.5, 2.7 and 2.8 were all reprinted with small modifications with permission from ACS publications. The statistical analysis was also divided amongst us. In Chapter 3, Nick's Mathematica skills helped me create Figure 3.4. All other figures in Chapter 3 were reprinted with permission from ACS publications. I would like to thank Nick in particular for his analysis of the cross-correlation and generating Figures 4.7 and Figure 4.9, reprinted here with permission from ACS Publications with some modifications. The data analysis and experimental data collection we did together as well. In Chapter 5, the data presented was also taken by the team. We had many long nights staring at various computers, and losing our minds over crashed tips. I thank them from the bottom of my heart.

I humbly acknowledge my advisers and mentors who have supported me along the way: Prof. Eric O. Potma, Prof. Matt Law, Dr. Danielle Watt, Dr. Lori Greene, Prof. Stella Quiñones, Prof. Albert R. Matlin, Prof. Robert Q. Thompson, Prof. Mahesh Narayan, Prof. Sergey Nizkorodov, Dr. Phong Luong, Prof. Roger McWilliams, Amy Bue and Raslyn Rendon.

At this point, I should thank Joonhee once again–he really belongs in every category (and possibly also in his own category). PREEEEESENT.

Finally, I would like to express my sincere gratitude for my graduate advisor, Prof. V. Ara Apkarian. I will always admire your enthusiasm for boldly venturing into the unknown.

I acknowledge funding from the NSF Graduate Research Fellowship program (DGE-1321846) and from NSF-CCI CaSTL (CHE-1414466).

CURRICULUM VITAE

Laura Rios

EDUCATION

Doctor of Philosophy in Chemistry **2017**
University of California, Irvine *Irvine, CA*

Bachelor of Arts in Chemistry **2012**
Oberlin College *Oberlin, OH*

RESEARCH EXPERIENCE

NSF Graduate Research Fellow **2013–2017**
University of California, Irvine *Irvine, California*

Student Research Assistant **2009–2012**
Oberlin College *Oberlin, Ohio*

Student Research Intern **2007–2010**
University of Texas at El Paso (UTEP) *El Paso, Texas*

Research and Engineering Apprenticeship Program **2006–2007**
Army Research Office/UTEP *El Paso, Texas*

TEACHING EXPERIENCE

Graduate Teaching Assistant, general chemistry **2012–2013**
University of California, Irvine *Irvine, California*

Graduate Teaching Assistant, Physical Chemistry Laboratory **2013–2014**
University of California, Irvine *Irvine, California*

COSMOS Graduate Teaching Assistant **2013**
University of California, Irvine *Irvine, California*

General Chemistry tutor **2009–2012**
Oberlin College *Oberlin, Ohio*

FELLOWSHIPS AND AWARDS

Ford Foundation Dissertation Fellowship, Awardee **2017**
University of California, Irvine *Irvine, California*

National Science Foundation Graduate Research Fellowship **2013–2017**
University of California, Irvine *Irvine, California*

Chemistry at the Space-Time Limit Diversity Fellowship **2012–2013**
University of California, Irvine *Irvine, California*

NSF Computation and Modeling S-STEM Scholar **2010–2012**
Oberlin College *Oberlin, Ohio*

Graduate Student Outstanding Oral Presentation **2015**
Sponsored by SACNAS and *Washington, D.C.*

The American Society for Biochemistry and Molecular Biology

UC Irvine Chemistry Department Service Award **2014**
University of California, Irvine *Irvine, California*

Hypercube Scholar Award **2012**
Oberlin College *Oberlin, Ohio*

LEADERSHIP AND OUTREACH

President of OSA/SPIE student chapter **2015-2017**
University of California, Irvine *Irvine, California*

Vice-President of OSA/SPIE student chapter **2014-2015**
University of California, Irvine *Irvine, California*

DECADE PLUS Mentor **2016-2017**
University of California, Irvine *Irvine, California*

DECADE Physical Sciences Student Council **2016-2017**
Chemistry Department student representative *Irvine, California*

Boys and Girls Club Volunteer Teacher **2012-2016**
University of California, Irvine *Irvine, California*

REFEREED JOURNAL PUBLICATIONS

Hovering and Twirling of Thiol-tethered Molecules by Confinement Between Surfaces **June 2016**
Journal of Physical Chemistry Letters

Hydroxylamine catalyzed Nazarov cyclizations of divinyl ketones **Nov 2015**
Tetrahedron Letters

Isomerization of One Molecule Observed through Tip-Enhanced Raman Spectroscopy **Sept 2015**
Nano Letters

Single Electron Bipolar Conductance Switch Driven by the Molecular Aharonov-Bohm Effect **May 2014**
ACS Nano

Visualizing Capsaicinoids: Colorimetric Analysis of Chili Peppers **Jan 2012**
Journal of Chemical Education

From Folklore to Molecular Pharmacophores: Cultivating STEM Students among Young, First-Generation Female Mexican-Americans **Oct 2010**
Journal of Chemical Education

CONFERENCE PRESENTATIONS

Tickling electrons with light **Oct 2016**
SACNAS National Conference 2016

Bias-dependent motion of thiol-tethered azobenzene molecules on Au(111) **July 2016**
Physical Electronics Conference

Isomerization of a single molecule on an STM tip. **Dec 2015**
Pacifichem: The International Chemical Congress of Pacific Basin Societies

Manipulation of Light and Electrons with Submolecular Resolution. SACNAS National Conference 2015	**Oct 2015**
A single Jahn-Teller active electron as a multi-throw multipolar conductance switch. American Physical Society	**April 2014**
Imaging vibronic dynamics at the STM junction: Manipulation of light and current through a single electron on a single molecule. Dynamics, Interactions, and Electronic Transitions at Surfaces Conference	**Oct 2014**
Novel cyclization mechanism for the Nazarov reaction: mechanistic computational studies. ACS meeting-in-miniature	**Oct 2011**

ABSTRACT OF THE DISSERTATION

Toward the Space-Time Limit

By

Laura Rios

Doctor of Philosophy in Chemistry

University of California, Irvine, 2017

Professor V. Ara Apkarian, Chair

A chemical reaction is fundamentally initiated by the restructuring of a chemical bond. Chemical reactions occur so quickly that their exact trajectory is unknown. To unlock the secret, first one would seek to know the inner working of a single molecule, and therein, a single chemical bond. However, the task is no small feat. Single molecule studies require exquisite spatial resolution afforded by relatively new technologies, and ultrafast laser techniques. The overarching theme of my dissertation will be the path towards achieving the space-time limit in chemistry: namely, the ability to record the structural changes of individual molecules during a reaction, one event at a time.

A scanning tunneling microscope (STM) is used to image the molecules and manipulate their electronic environments. STM has the capacity to create topographical images of molecules with Ångström (10^{-10} m – the size of an atom) resolution, and can also probe the molecule electronically by use of a tunneling current (I_t). STM images reflect the changes in the potential energy surface (PES), and help us understand how molecules interact with surfaces and each other, thereby accessing the fundamental problem of catalysis and chemical reactions. In addition to seeing the molecule, we use Raman spectroscopy to track its molecular changes with chemical specificity. I combine these experimental tools to investigate tip-enhanced Raman spectra (TERS) of single molecules within the confines of a STM.

These methods were used to report the conformational change of a single azobenzene-thiol derivative molecule. Although we were able to definitely isolate a single molecule signature, imaging the single molecule in real space and time proved elusive. Additionally, I report on a conductance switch based on the observable change of the topographic STM images of a radical anion mediated by the spin flip of a single electron on a single molecule. This is effectively the smallest achievable architecture of molecular electronics, negating the need for heat dissipation in small systems. A related work found how physisorption potentials of molecules to metals could be experimentally visually verified and modeled by STM, thus allowing us to use the STM tip as a driver for molecular motion on surfaces.

Throughtout this work, we noted that a dominant feature of single molecule chemistry are intensity and spectral fluctuations that are difficult to characterize, as the molecule contorts wildly when it experiences distinct and powerful electromagnetic fields and field gradients. This much is evident in the last experiment, and chapter, of this thesis. Raman spectra associated with cobalt (II) tetraphenyl porphyrin (CoTPP) axially coordinated with bipyridyl ethylene (BPE) were captured with Raman mapping with nanometer resolution. However, the stochastic apperance of Raman lines and low resolution images made it difficult to ascertain which molecule we captured. The preliminary results as well as follow-up conrol experiments are discussed.

While each experiment constitutes in and of itself an important, individual contribution, their sum establishes the principles of seeing single-molecule chemistry.

Chapter 1

Introduction

1.1 Defining the Space-Time Limit

To begin, I must first establish the “space-time limit” with a discussion of the physical and experimental confines governing single molecule chemistry. By understanding the experimental expectations, and deviations from expectations, we gain insight into the single molecule realm. The motivation for attempting the difficult task of visualizing a single molecule reaction is two-fold: one, to delve into the physics of chemical reaction to answer the general question of how and why does chemistry occur; and two, to satisfy an intense curiosity. What lies in a quantum universe folded into our own?

Spectroscopic investigation of single molecules started only relatively recently. The first instance of optical detection of a single molecule was in 1989 by Moerner et al., where a *p*-terphenyl crystal was doped with pentacene molcules at cryogenic temperatures. The single molecule signature in this work was captured by absorption spectroscopy techniques, where the excitation laser was scanned over the ZPLs in the wings of the inhomogeneously broadened lines [1]. Single impurities in crystals were also investigated using fluorescence spectroscopy [2]. Further work in this lab has highlighted the motivation of seeking answers in the single molecule realm: hidden heterogeneities [3]. In condensed matter physics and electronics, it is often taken for granted that out of thousands of purported active sites, only a few will exhibit the desired behavior (*e.g.* heterogeneities which hamper rectification properties in solar panels [4]). Evidently, hidden hetereogeneities exist that alter the potential energy surface (PES) enough to create a variety of chemical/physical processes that can occur in even microscopically identical sites. In ensemble measurements, we obtain the average behavior; for single molecule experiments, we can start to tease apart how individuals behave in isolation. Eventually, this knowledge may help us understand some of the nuances of solid state devices.

Beyond solid state experiments, biological sciences researchers have also made significant headway into the single molecule regime. Using typically fluorescence techniques (*e.g.* fluorescence-correlation spectroscopy, fluorescent resonance energy transfer (FRET) [5, 6, 7]), and mass spectrometry [8]. However, this limit is distinct from the one I pursue, since many biologically relevant single molecules such as proteins and DNA cages are quite large, typically in the kDa region [9]. Additionally, fluorescent techniques are a resonant process. The incident laser prompts an electronic transition, and after a resonance lifetime, the molecule returns to the ground state by emitting the absorbed energy as photons.

A different spectroscopic technique, Raman scattering, can be employed with generality. Raman scattering is a non-resonant process, so the energy of the photon is not crucial to obtaining a spectrum of the molecule. For the majority of incident photons, the molecule will scatter photons with the same energy as the incident energy in a Rayleigh scattering process. A small part of incident energy– about 1 in a million photons– can vibrationally excite the molecule, which will re-scatter with a shifted energy from the incident photons– this is the Raman scattering portion, and is indicative of the types of vibrations present in the molecule [10]. Of course, Raman scattering may also be excited resonantly, giving rise to a more complex spectrum with overtones and combination bands as the molecular accesses a real excited state instead of a coherence [11].

Raman spectroscopy has a long and well-studied history, beginning with its discovery by Sir C.V. Raman in 1928, where it was first observed by his unaided eye, then ultimately verified with a pocket spectroscope [12]. As an analytical tool, Raman spectroscopy was used extensively in the 1930's as a way to nondestructively determine structures of molecules. The first use of Raman spectroscopy for single molecule studies by Soper on rhodamine 6G began around the same time as many other single molecule experiments [13].

In the last decade, significant strides have been made towards the space-time limit. The first ultrafast microscopy of interface GaAs quantum dots was achieved in 2002 [14], and single molecule pump-probe detection was achieved shortly thereafter [15]. Despite the inherent difficulties, even room temperature studies have seen success [16], as have broadband explorations [17] and many other configurations and techniques [18, 19, 20].

Despite these significant advances and body of knowledge, the field finds itself at odds with respect to the fundamental mechanism offering submolecular resolution. Even the most cited papers have yet to propose a widely accepted and rigorous interpretation of results [21, 22, 23]. It is evident that a paradigm shift must occur before more progress can be made. The statistical nature of single molecule experiments necessitates looking beyond the static picture of the average, and scrutinizing minute fluctuations in data.

1.1.1 Single molecule limit

To elucidate the revised expectations, let us first consider the random walk model. For an individual, its trajectory of back, and forth, and back is evident to the observer. For two individuals, things get rapidly more complicated. Individual A may go back and back and forward, where as Individual B may go forward, back, and forward once again. As we increase the number of individuals to billions and billions of actors, the variations in their random walks average out and we are left with a characteristic signal: this is an ensemble-averaged measurement.

A great advantage of single-molecule work over ensemble-averaged measurements is the emergence of the actual distribution of the experimental parameter. A kinetic scheme describes the discrete changes in the energy landscape that prompted by underlying stochatic processes. For an ensemble measurement, the differences in the kinetic scheme of fundamental inherent process driving the chemical rection are averaged out. Therefore, the researcher interested in isolating the driving processes much search for a single molecule kinetic scheme. For a detailed explanation of kinetic schemes, please see the discussion by Liljeroth [24].

To bring the space-time limit to the single molecule level, an additional layer of complexity clouds the path. Clearly, an enhancement of the molecular signal is required to observe single molecule chemistry. Several increasingly in-depth experiments conducted by Fleischmann, Albrecht, and Jeanmaire [25, 26, 27] established a method for introducing sufficient enhancement of the scattered Raman field to be able to observe single molecule signal. Early experiments relied on roughening a silver electrode to serve as the cathode in electrochemical experiments[28]. Initially, Fleischmann attributed this to the increased surface area on the cathode due to roughening, allowing for augmented adsorption of interrogated molecules [25]. In a pivotal sequent experiment, Jeanmaire and Van Duyne found an approximately $10^5 - 10^6$-fold increase of the Raman signal in comparison to the signal expected for a monolayer of pyridine adsorbed on a smooth Ag surface [27]. Initially, Van Duyne and several co-workers offered an image field model as an explanation for the enhancement [29, 30, 31]. While it was used to justify enhanced Raman signals for a number of years [32], the theory has gradually evolved to invoke classical electromagnetism (EM) instead [33]. It is known that placing a metal surface in an external electric field will create a collective oscillation of the free electrons (*i.e.* plasmons). When confined spatially, we further refine the definition to localized surface plasmons (LSPs). The general mechanism by which the LSP enhances the scattered Raman signal was termed (appropriately) surface-enhanced Raman spectroscopy (SERS). In addition to the EM mechanism, the million-fold increase in Raman signal is also attributed to a chemical enhancement mechanism by charge transfer [34, 35].

A sharp tip can be used instead of a roughened surface, which may aid in general for imaging molecules as well as enhancing Raman signals. Roughened surfaces, or other more refined SERS geometries such as paired metal nanospheres, create "hot spots" by the classical electromagnetic mechanism known as the lightning rod effect [36, 37]. A sharp metal tip acts as a discontinuity in an external electric field, and the accumulation of charges at the apex create a strong local electric field, which can enhance the Raman signal of a molecule in the vicinity of the tip. This is known as tip-enhanced Raman spectroscopy (TERS). Wessel first offered TERS as a powerful contender to seek single molecule Raman spectra [38]. Indeed, TERS has several advantages over SERS. While SERS required a roughened, coinage metal surface, TERS offers identical, if not superior enhancement for various surfaces such as metals [39, 40], semiconductors [41], and insulators [42].

However, the main limitation of TERS revolves around the very tool that offers the advantages: the metallic tip. Its exact role in the enhancement mechanism is not well understood beyond what researchers have already determined in general terms as described above [43, 44]. Many hypotheses are present in the literature about the nuances of the chemical and EM enhancement mechanisms[45, 46, 47]. There is also some question as to whether the current single molecule studies address the difficult in differentiating between a target molecule and decomposed, carbonaceous species [48]. Nevertheless, it is evident that this remains a crucial engineering problem as well as a scientific one [46, 49].

1.1.2 Space limit

In order to see chemistry in the act, we must be able to resolve a chemical bond. The breaking and making of chemical bonds is the fundamental first step of a chemical reaction. A good starting point to develop an intuition for the spatial scales required to see chemistry is the Bohr radius, the most probable distance between the proton and electron of a hydrogen atom in its ground state. Its value is 0.529 Å. A C-C bond, the longest bond for a carbon covalent bond, is 1.54 Å (0.154 nm). Thus, we must be able to observe the world with a subnanometer magnifying glass. The optical microscope, so useful for delving into the micron world of biology, is here hampered by the diffraction barrier. Arising from the fundamental, wave nature of light, the diffraction barrier bars a microscope to resolve anything less than roughly half the wavelength of the light used for imaging. For a 532 nm laser, ideal resolution would go no further than ~ 265 nm: hardly useful for the question posed.

The most obvious, but potentially tricky, approach is to not employ an optical microscope at all. In 1981, Bining and Rohrer at IBM invented the scanning tunneling microscope (STM) which uses an atomically sharp metal tip hovering $\sim 5-7$ Å from the surface of a metal substrate [50]. After applying a voltage bias across the tip-sample junction, a tunneling current (I_t) is established as electrons from the tip states tunnel through the vacuum to the metal substrate. I_t is a function of tip position, sample bias, and the local density of states (LDOS). Applying the solutions of the Schrödinger equation for the familiar 1D tunneling problem to the tip-vacuum-substrate junction, one can determine how I_t scales with the distances between the tip and metal sample [51]. The current is exponentially dependent on the change in distance that it experiences, evident in the solution to this problem given in Equation 1.1. Here, $\kappa = \sqrt{\frac{2m(E-U_z)}{\hbar}}$. This mechanism of accessing spatial resolution circumvents the diffraction limit by using electrons instead of light to image.

$$I = I_0 \exp[2\kappa(z - z_0)] \tag{1.1}$$

To date, STM has been used extensively in the burgeoning nanoworld. It can effectively image and manipulate single molecules [52], single atoms [53], and even single electron pairs [54]. STM can also manipulate atoms and probe the underlying PES. There is also significant precedent for using STM to induce and image chemical reactions as well, usually by functionalizing the tip with a molecule of a particularly characteristic vibration (*e.g.* CO) [55]. Another useful tool in STM is scanning tunneling spectroscopy (STS). In STS, one fixes the tip height on a feature in the image, and scans I_t as a function of the voltage differences between the tip and sample (sample bias, V_B). The sample bias sets the electron energy, and typically the tip is virtually grounded such that a $V_B < 0$ denotes electrons tunneling from tip to sample. The result is an I-V curve, which is then differentiated to obtain the differential conductance curve (dj/dV). This unique spectrum corresponds to the LDOS. Thus, STS gains access to an energy-resolved spectrum of the electronic states a few electron-volts (eV) on either side of the Fermi level [56].

Is there a limit to the spatial resolution afforded by STM? Because the resolution ultimately depends on the wavefunction overlap between the tip and the LDOS, there are is no steadfast, scrutable physical resolution criteria as with optical microscopy [57]. There is significant variation in the structure of the tip due to the way they are currently fabricated, and as such resolution varies from tip to tip rather than by an explicit physical limitation. This fact is demonstrated by the often experimentally usurped vertical resolution limit of the Fermi level LDOS corrugation amplidtude explained by the s-wave model [58]. This theoretical limit is given by

$$\Delta Z \approx (\frac{2}{k}) \exp[2Z \left(k - \sqrt{k^2 + \frac{\pi^2}{a^2}} \right)] \tag{1.2}$$

where Z is the vertical distance from the sample surface to the curvature of the tip, k is the decay constant, and a is the fundamental periodicity of the corrugation for the metal under inspection. Although Equation 1.2 predicts a vertical resolution of $\sim 0.03\,\text{Å}$ for Al(111), experiments have found the limit is closer to $0.1\,\text{Å}$ [59]. Clearly, the s-wave model is too simplistic, and the topograph cares about more than just the s-wave solution.

On the other hand, lateral resolution is given roughly by $\left[\left(2\text{Å}\right)(R+d)\right]^{1/2}$ where R is the tip radius of curvature and d is the tip-sample gap [58]. Experimentally, the best resolution obtained is 0.1 nm laterally and 0.01nm in depth [60]. However, there are several practical issues which require forethought and planning. One subtle point is the nature of the image itself. The STM obtains images of a convolution of tip, molecule, and metal states, or, an electron density– chemical bonds are not directly imaged, unlike in atomic force microscopy (AFM).

The choice of the molecule must be made with these limitations in mind. Molecules must be able to adhere to a crystalline metal surface. Of those molecules that adhere to metals, there is a further requirement if STM is to be employed for TERS: molecules must align with the tip dipole in order to achieve optimum tip enhancement. Experimental and theoretical findings both scaffold an argument wherein the main molecular dipole must be aligned to the tip dipole [61, 62]. If this is truly the case, and there is no way to get around this need for enhancement, then direct imaging and single molecule study would be mostly at odds. So while Raman spectroscopy is a general technique, our STM offers some exclusivity in terms of the molecules and systems we can easily analyze.

An important experimental limit is the structure of the tip. It is difficult to alter the shape of the tip, and therefore the goodness of the image *in situ*; field emissions and poking the metal surface gently are an STM user's only way of changing the tip shape, but those changes are not controllable. Even engineering a useful tip is cumbersome, as detailed in the Appendix.

Despite some experimental obstacles, the power of STM in spatial resolution, energy-resolved spectra, and manipulation of the PES makes it uniquely able to study single molecule chemistry. Therefore, we pursue the space limit with this tool in our arsenal.

1.1.3 Time limit

The fastest process a camera can capture is determined by its shutter speed. The very best camera engineered at MIT has picosecond resolution [63]. Let us consider a very simple reaction that, appropriately, allows us to see: the activation of the visual pigment rhodopsin in the human eye for monochromatic vision. According to time-resolved IR spectroscopic experiments, the formation of the initial photoproducts occurs on the order of 200 fs [64, 65]. To be able to monitor this reaction, evidently we need a clocking probe in addition to a camera.

In 1960, the invention of the ruby laser by Maiman [66] provided the key to the ultrafast probe we need. The speed with which technologies overtook the last innovation was impressive. The first ruby laser was continuous wave, but only a year later McClung working in R.W. Hellwarth's group managed to get nanosecond laser pulses by Q-switching [67]. With the shortening of the laser pulse came the intensification of the peak power. Soon thereafter, mode-locking techniques had progressed to the point where picosecond pulses were now possible [68]. By 1991, solid-state Ti:sapphire self-mode-locked lasers could achieve 60 femtosecond (fs) pulses [69], and six years later 5 fs pulses at up to 1 MHz repetition rate were achieved [70]. It was 30 years from the patent of the first laser, to having femtosecond resolution.

The advances were quick, but the use of laser spectroscopy to study chemical processes greatly the generation of fs pulses. Nonradiative process were able to be directly measured by picosecond pulses, including the photophysical rates of intersystem crossing in dyes [71] and internal conversion in biological systems [72]. "Femtochemistry," a termed coined by Professor Ahmed H. Zewail, was on the horizon. In his Nobel prize address, he describes the three major scaffolds of femtochemistry: coherence of the molecule (*i.e.* a single molecule does not dephase), of the ensemble (*i.e.* the inhomogenous dephasing time of the ensemble is long with respect to fs preparation), and of the trajectory [73]. Ultrafast lasers allow us to couple the latter two, creating a coherent molecular trajectory out of an incoherent ensemble measurement. This was demonstrated first by our team at CaSTL [74].

Obviously, the rapid pace of advancement has not overcome all experimental difficulties. As mentioned, compressing a laser pulse also greatly increases the peak power, the maximum optical power of a pulse [75]. For a 1 mJ pulse with a 100 fs pulse width, one obtains 10 GW (10×10^9 watts) of peak power. Therefore, heating and destruction of samples in single molecule junctions is an important issue to address [76]. Other sources of damage include plasmonic heating [77],joule heating by electrical field ($\propto \sigma |E|^2$, so E is enhanced by more than 1000 times) [78], and tip-induced heating due to the confinement of such large peak power to small junctions [79]. The effect of local heating in single-molecular electronic transport [80, 81] also means some experimental results are readily interpreted on merely the basis of decomposition. Lately, researchers have gotten around this problem by employing a terahertz system coupled to an STM junction to create a straightforward spatial probe [82, 83], but this does not provide a spectral signature.

As in chess, now that we have established the rules, it is time to play.

1.2 Thesis Outline

1.2.1 First principle: Scanning tunneling microscopy reveals dynamic information in addition to static images.

With some practical and theoretical limits of STM-TERS established, one may also seek out limiting architectures for the spatial scales one may expect our specific experimental setup to measure accurately.

Based on previous experiments in CaSTL detailing Jahn-Teller (JT) dynamics of a lone electron, we continued to explore the zinc (II) etioporphyrin (ZEP) dianion [84]. Since we are in the dynamical, rather than static, JT limit (*i.e.* the vibration frequency is greater than the stabilization energy), the molecule does not adopt its distorted coordinates permanently. Instead, the phased superposition of the skeletal deformations generate a *pseudorotation*. The overall molecular structure does not rotate; instead, the rotation of atoms about their equilibrium position produces a molecule identical to the original [85]. The pseudorotation effectively drags the orbital about the macrocycle, mimicking the physical characterization of a particle on a disk. The interaction between the electronic and nuclear motions describes the vibronic coupling of the system. Furthermore, the vibronic potential associated with this coupling constitutes a conical intersection, a vector potential which determines the phase of the electron as it rotates about the singularity of the cone, where the two potential energies intersect.

In this experiment, we added a new layer of understanding to this problem. Once again, it begins with a distinctive topography, and recognition of the fact that an STM topography is a representation of the LDOS. The constant current STM topography of its initial (OFF) state can be measured directly, and its topography is straightforwardly understood as the LDOS of the ground state of the conductance switch. The dj/dV curve of a ZEP molecule shows the simultaneity of an opening of the dianion resonance states, increase in frequency of a bistable conductance switch, and electroluminscence (EL) photon count at $V_b = 2.0$ V. The state with an increased or decreased conductance (the ON state) is transient. We re-construct the ON state by recognizing that the additional, but small (~ 1 meV), splitting of the vibronic states is due to the phase accumulated with the electron orbiting about a singularity. This is termed the molecular Aharonov-Bohm effect, so–called by Mead [86] in reference to its similarity to an earlier, reported eponymous effect [87]. The experiment detailed in this section provides evidence for this interpretation.

1.2.2 Second principle: STM can observe and manipulate the underlying potential energy surface

Evidently, it is important to recognize also the role of the tip in the environment of the investigated molecule. In this experiment, an azobenzene derivative with a thioalkane tether (ABT) is anchored on one end with a strong Au-S bond, and in principle the rest of the molecule is free to explore the PES. I made several interesting observations of the dynamics of ABT on Au(111):

- At high coverage, ABT molecules will link together across the fcc portions of the "herringbone" reconstruction. At low coverage, ABT molecules will preferentially adhere to the screw dislocation and kinks on the surface.
- Further, low bias scans of isolated ABT molecules will induce a hindered rotation, though the molecule remains tethered by its sulfur atom. We dub this "twirling" to differentiate between the more strictly defined term "rotation," which necessitates motion about a symmetry axis.
- Depending on its adsorption site, the molecule may take on various shapes, but interestingly, there are versions that appear as disks, and others as perfect hexagons, mimicking the six-fold symmetry of the Au(111) surface. These molecules are distinct in their height and length profiles, leading me to conclude that some molecule "hover" before twirling (these will look like concentric circles), and others will lay with the azobenzene head flat (disks)

Since all these behaviors are reversibly bias dependent, I created a Morse potential model that describes at which tip-sample distance once may expect to see a disk or hexagon. In this model, the tip potential is included in the overall potential experienced by the molecule. Based off of previous work on physisorption potentials of benzene [88] I was able to create a consistent picture that explain the various images we saw at different tip-sample distances. Further, I was also able to describe the barrier to rotation by classically inverting the STM image and observing the change to the potential landscape [89]. This work constitutes an important insight into the role of van der Waals forces in STM.

1.2.3 Third principle: Single molecule behavior is by its nature distinct from ensemble measurements.

While Raman spectroscopy is employed for its specificity to chemical bonds, the nature of the spectrum is fundamentally different in a single molecule measurement. For example, Raman line intensities can greatly vary in single molecule measurements due to the orientation dependence of the Raman scattering tensor. In this experiment, the same ABT molecule on Au(111) is investigated spectroscopically. Using a continuous wave (cw) 532 nm laser, we sought to capture the trans-cis isomerization of ABT, but instead we had to content ourselves with the following experimental observations:

- At high coverage, ABT molecules link together and extend laterally outward from a common Au adatom.
- Even at high coverage, where thousands of molecules are observed in STM images, a Raman spectrum was unattainable.
- Suddenly, we captured a spectrum with random, significant fluctuations in intensity *and* wavenumber.
- We also observed an anti-correlated trajectory of two distinct spectra, characteristic of a two-level system within a single molecule.

In the first instances of randomly fluctuating spectra, we were able to determine that line positions were indeed shifting by more than their linewidths (*i.e.* were “meandering”). Equally interesting, the suddenness of the appearance of the Raman spectrum reminds the chemist of heterogeneous catalysis. We attributed these observations into a cohesive picture: a single ABT molecule found its way to a Ag atom on the tip, and experienced such strong fields that its spectrum was continuously changing. We cautiously named the two-level system the structural isomerization of ABT. In another instance we are able to pick up and then deposit a single ABT molcule onto a Ag tip affirm our hypothesis: while the molecule is picked up, vibrational lines grow in intensity, and once deposited back on the surface, we no longer see its vibrational spectrum.

In light of theoretical analysis accomplished by our collaborators Jensen et al., we have tweaked this explanation: the two spectra seen in the bistable trajectory are more consistent with the neutral and cationic spectrum of the molecule, with the latter resulting from a charge transfer between ABT and a silver adatom. Evidently, single molecule measurements require analysis breaking with traditional paradigms, which means a revised view of the statistical methods previously employed to discuss single molecule events.

Although we were able to definitely isolate the single molecule signature, imaging the single molecule in real space and time proved elusive. Below, I outline the last experiment undertaken with this in mind.

1.2.4 Principle 4: The crucial role of a well-engineered tip in spatially dependent TERS still requires study.

After recognizing the importance of the tip in single molecule measurements, our lab undertook an extensive engineering project. In order to determine the features which make a silver or gold scanning tip useful, we must first develop a population from which to draw observations. Tip engineering is tiresome and inefficient, so we designed two new etching methods which would allow for quicker rough etching of silver tips. This process is described in the Appendix for the interested researcher.

An argon ion etching station was also designed and built, with the focus on minute tuning of the tip apex. Based on experimental observations, we note that cleaner tips do not exhibit their own spectrum (previously, "carbonaceous species" [48, 90], and therefore we can be sure that the vibrational lines we see belong to the molecule. The last step in smoothing the tip is an *in vacuo* sputtering mechanism, along with a load-lock system that would allow for faster transfer of new tips to the STM chamber.

With the newest crop of highly engineering tips, we were able to capture spatially dependent Raman maps of cobalt (II) tetraphenylporphyrin (CoTPP) and bipyridyl ethylene (BPE) at liquid nitrogen temperatures ($T =\sim 80\ K$). Raman maps show that distinctive spectra can be seen that belong to either species with a lateral resolution of one nanometer. However, as in the case with ABT, the spectra do not strictly adhere to the ensemble spectrum. Remarkably, we observe combination bands and overtones although the free BPE molecule does not posses electronic resonances in the spectral window of relevance. Our preliminary evidence prompts a more complex model explicitly invoking the gap mode of the plasmonic junction than previously understood, although theory is ongoing.

Chapter 2

Conductance switch mediated by the spin-flip of a single electron

2.1 Background

The ability of STM to access dynamics has been used extensively in molecular electronics. Molecular electronics is a field generally concerned with the functionality of molecules as circuit elements.

As early as the 1950s, the possibility of constructing complex electronic functions by building materials from their atoms and molecules for an exact purpose [91]. Generally, the notion of "molecular engineering" has dominated molecular electronics, and new functionalities are brought forth daily. For example, metal-oxide nanowires with optional configuration as resistors or field-effect transistors have been proposed as chemical/biological sensors [92]. Becuse we are building from constituent parts, functionality in many areas can be tailored, as with high-capacitance, high-permittivity organic gate dielectric materials [93], tuned graphene nanoribbon semiconducting materials [94], and many, many other examples [95]. Chemical modification of molecular circuit elements remains an active field, and now it is possible to create an exactly functional molecular element [96].

Seemingly terminally specific, study of molecular electronics can even provide insight into theoretical exploration of electronics, such as the the appearance of the memristor [97]. It is also a field directly applicable to usable technologies: liquid crystal displays serve as an established example [98].

A particular important aspect of molecular electronic is a conductance switch, whereby the conductivity (ability of element to shuttle electrons around) changes over a setpoint. Because electrons are, in principle, the smallest available circuit element, a change in its transport would be crucial to control for many molecular devices. Conductance switches have been observed for a huge variety of systems and geometries, including phthalocynanin on a NaCl bilayer [99], Cu/HfO_2 interfaces [100], and metal-organic cuboctahedra mimicking liquid bilayer membranes [101].

Reed et al. first observed conductance switching in a single-molecule wherein they used a mechanically controllable break junction (MCBJ) to form a metal-molecule-metal configuration with benzene-1,4-dithiol molecules, resembling a quantum dot system [102]. Reed presented a quantitative analysis of the molecule's electron transport capabilities.

Ambient condition MCBJ has been the forerunner in experimental techniques [103], but there has been forays into electrodeposition methods [104], nanopore techniques [105], and electromigration methods [106]. In our case, we use scanning tunneling microscope (STM), exploring its exquisite spatial resolution capabilities for the purposes of detailing the localization of the switch. The use of STM in this field has been met with come setbacks such as tip instability [107], but remains a tool with promise for its ability to study electronic transport properties with the use of repeated current-voltage measurements.

Voltage control in the molecular junction appears to be a largely material aspect [108].

Improving the exact nature of the distinction between stochastic switching, which is an entirely statistical problem, and voltage-driven conductance changes should prove crucial to the development of nanodevices.

A logical progression in the development of molecular electronics as discussed above is an architecture in which the functionality of a single electron may be used to control electron transport. Here, we report on the realization of this limit in a single molecule.

In previous work in this lab, the dynamical motion of a single electron and molecule was observed and characterized the conical intersection of a Jahn-Teller active dianion of zinc (II) etioporphyrin (ZEP) [84]. STM images demonstrate the transformation of the STM topography according to the vibronic motion of the orbiting lone electron of ZEP$^-$. ZEP is a symmetric molecule: to a good approximation, it obeys D_{4h} symmetry. At $V_B = 1.8$ V, ZEP readily reduces to ZEP$^-$ on an insulating (oxide) layer. The unpaired electron occupies a doubly degenerate orbital. Due to the ensuing energetic instablility, the molecule undergoes a slight distortion in order to break the symmetry and lower overall energy. The distortions stem from the coupling of the doubly degenerate state to asymmetric vibrations, one corresponding to rectangular deformation and the other, to a rhomboid deformation of the hydrocarbon macrocycle. This can be visualized by simplifying ZEP to a square, where each corner replaces a pyrrole unit. As described in Section 1.2.1, the phased superposition of the rhomboid and rectangular deformation creates a pseudorotation.

The most widely accepted mechanism for pseudorotation is the Berry mechanism, which invokes interconversion between ligands in highly symmetric molecules [109]. Because a pseudorotation is a cyclic motion where the ionic coordinates travel along a closed orbit, an orbital magnetic moment emerges. The ionic magnetic moment is partially screened by the electrons which also participate in the cyclic motion as they follow the ions. Since the movement of the ions is relatively slow, the motion can be regarded as a cyclic adiabatic process, and thus a geometric phase is accumulated [110, 111].

Within the context of the geometric phase, the mathematical identity between the dynamical JT effect [112] and the quantum phase of current on a vector potential yields [87], was collected under the banner of the molecular Aharonov–Bohm effect. This is the crux of our single electron switch. In the limit of weak spin–orbit coupling, the spin-vibronic interaction becomes important. The spin-flip induced by resonant scattering of tunneling electrons drives the transfer between the two sheets of the adiabatic potential from which the geometric phase arises. Functional mapping of our small switch allow the reconstruction of the spin–vibronic densities and the controlling Hamiltonian.

2.2 Experimental Details

2.2.1 General setup

To collect as much of the radiation emitting from the STM junction, the STM sample sits atop a parabolic mirror. When the tip is in the focus of the mirror, the radiation emitting from the tip-sample junction emerges collimated. The radius of curvature of a properly engineered STM tip is on the order of $\sim$ 50 nm, yet the cw laser has a minimum spot size of a $\sim 10\,\mu$m. Much of the tip is illuminated, and so we must select out the scattered light from just the tip-sample junction. To accomplish this, we also put in a spatial filter. The parabolic mirror sits on XYZ piezo motors, which can translate the mirror laterally until a symmetric parabolic mirror image (PMI) is observed on the liquid nitrogen (LN2)-cooled CCD. The three shadows come from the piezo stacks holding up the sample.

In Figure 2.1, the schematic illustrates how the collimated light captured by the parabolic mirror is directed towards the CCD/spectrometer. The major components of the spatial filter are also shown. A notch filter (NF) is used to shut out remaining laser light for experiments where Raman spectra are taken (not the case in this chapter, but will be relevant for the rest of the thesis). The inset of black and white images shows experimentally observed EL images (top row) as we adjust the parabolic mirror, and their corresponding calculated images using explicit simulations (Zemax OpticStudio 14.2) of the image of the sectored mirror formed at the CCD plane. Evidently, the tip apex and the focus of the parabola can be overlapped with near-diffraction limited precision of less than 3 μm. The arrangement allows precise pre-alignment of the collection optical line by monitoring the image of EL from the silver tip apex, which is enhanced by the junction plasmon, as explained in the lab's previous work on this molecule [113].

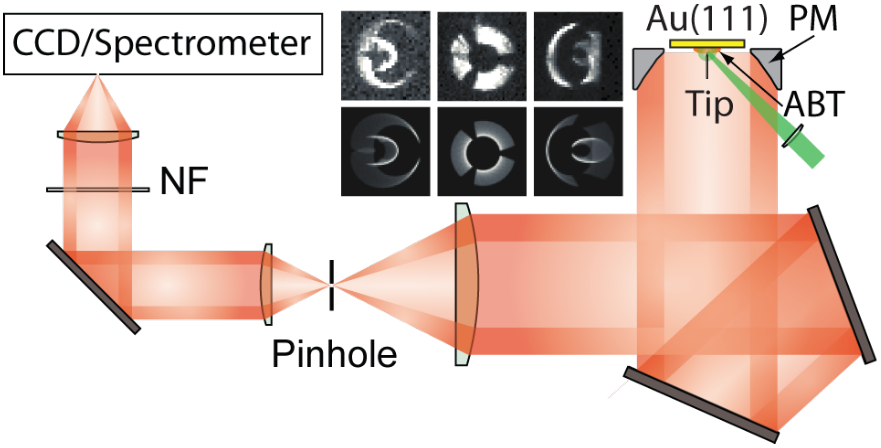

Figure 2.1: The general setup allows for maximum radiation capture from the tip-sample junction. The images are obtained through EL captured on the CCD (top row) and their simulation (bottom row) are for the PM offset from the focus by 35, 0, and +30 μm laterally and 14 μm vertically.

2.2.2 Sample preparation

In a UHV-STM chamber ($P = 4 \times 10^{-11}$ torr), an atomically flat NiAl(110) sample surface was prepared by sputtering and annealing to 600℃ several times until a smooth surface was observed. The Ag tip used as the probe was similarly sputtered and annealed. A thin layer of aluminum oxide, Al_2O_3 measuring 5 Å was then grown on the surface. These procedures are fairly standard [114]. Substantial coverage of Al_{203}, and small, isolated islands of metal surface were observed. Al$_{203}$ is required for two reasons: one, ZEP readily reduces on Al$_2$O$_3$, and its anion is stable for long periods of time, which is useful for experiments where long traces are recorded; two, Al$_2$O$_3$ is an insulator, effectively decoupling the molecule from the metal substrate. Finally, ZEP is thermally sublimed by heating the holding crucible at 2.4 A for 25 minutes, and exposing the sample to the molecule for 2.5 minutes.

2.2.3 Collecting switching data

On the metal surface, the molecule has a four-fold symmetry, resembling a clover, where the large electron densities correspond to the pyrrole units of the molecular macrocycle (Figure 2.2(b)). At biases above $\sim 2.0\ V$, molecules on the oxide layer assume a distinctive "saddle" shape, with small and big lobes (SL and BL), approximately perpendicular to one another, evident in Figure 2.2(c). A sample bias of 2.0 V marks the opening of the dianion resonance states, so the saddle shape is the ZEP dianion.

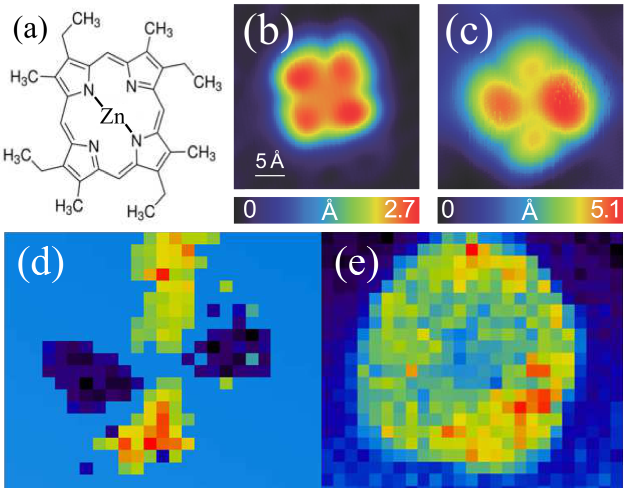

Figure 2.2: (a) Chemical drawing of Zn etioporphyrin (b) STM topogrpahy taken at low bias, which shows large electron densities concentrated over each pyrrole unit (c) ZEP molecule atop oxide layer. From the color bar, it is evident that this molecule has higher electron densities concentrated on two lobes. (d) Map of the switching behavior where the red/orange/green hues denote positive switching, and blue/purple/black palette denotes negative switching. (e) EL of ZEP

At this sample bias, the molecule exhibits bistable conductance switching (whereby conductance either increases or decreases over a set point). Both behaviors are spatially dependent. Positive conductance switching occurs over the SL of the ZEP anion, whereas negative conductance switching occurs over BL (Figure 2.2(d)). A concomitant feature is electroluminescence (EL) from the molecules on the oxide layer (Figure 2.2(e)).

To collect data for statistical analysis, we placed the STM tip on one lobe at a time, instead of scanning. After defining the setpoint current and the sample bias (ranging from 1.6 V to 2.1 V, where we observe resonance), we turned off the feedback and recorded current traces for up to a minute with 10 μs resolution at biases $\geq$ 1.5 V. In these instances, the switching residence time was less than 0.5 ms. For low-bias experiments ($\leq$ 1.9 V), the current trace was recorded for 5 minutes with a 1 ms resolution. These low-bias experiments exhibited switches were less fleeting, lasting upwards of 1 ms. Traces were recorded for a set point current of 20-70 pA at intervals of 10 pA.

2.2.4 Mapping

To create maps of the conductance switching (*e.g.* Figure 2.2(d)), we place our tip over each pixel and record the time profile. A LabView program deconvolutes each trace to determine whether the interrogated area is undergoing positive or negative conductance switching. We immediately note that negative switching is largely localized to the BL, but we observe broken symmetry of the switching amplitude maps with regards to the positive switching. Similar maps of EL are recorded (*e.g.* Figure 2.2(e))

Functional maps which describe the connection between vibronic structue and dynamic function are imaged by functional mapping (Figure 2.5). The maps are extracted from an extensive data set consisting of 0.5 s-long current traces digitized every 500 μs, recorded on a 38 $\times$ 38 pixel spatial grid.

2.3 Statistical Analyis

After collecting the relevant data, we can combine all the observations to detail the interrelated phenomena. In Figure 2.3(a), their relationship to the dianion resonance states is seen with the dj/dV curve and concomitant increase in frequency of the switch (shown in purple dots), and the EL photon count (in green).

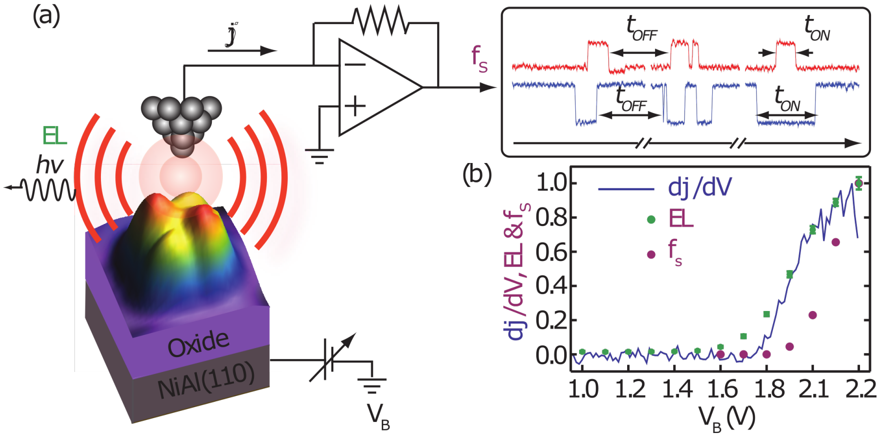

Figure 2.3: ZnEtio dianion as a light-emitting, conductance switch. (a) The time traces of the tunneling current show positive (red) or negative (blue) switching, depending on tip placement inside the molecule. (b) The normalized differential conductance curve, dj/dVvsV (blue curve), shows the onset of the dianion resonance near 1.8 eV. The photon count (green dots) and switching frequency (purple dots) track the same resonance.

From the time profiles recorded on a grid point, at a given bias and tip current, we generate histograms of the amount of time the molecule spends in the switched state (ON state) and at the set point (OFF state). We denote these on-times (t_{ON} in Figure 2.3) and off-times ($t_{O}FF$ in Figure 2.3), respectively. We also generate histograms of the conductance switch amplitude, or pulse height distribution (PHD). Examples of extracted PHDs are shown in Figure 2.4(b). The PHD is distinctly bimodal, indicating the switch comprises a two-level system. As we approach resonant biases, the ON state becomes less well-defined as its lifetime shortens beyond the response of our preamplifier. In order to analyze these traces, we reconstruct the pulse profiles using the Laplace transform of the square wave, and fitting it directly. Figure 2.4(c)-(f) shows that the extracted of on- and off-times decay exponentially with time, indicating a Markovian (*i.e.* memoryless) switch. For now, I assert this as fact, and leave a more explicit explanation to the Appendix. The data are representative of the same measurements carried out on 10 different molecules of similar topography.

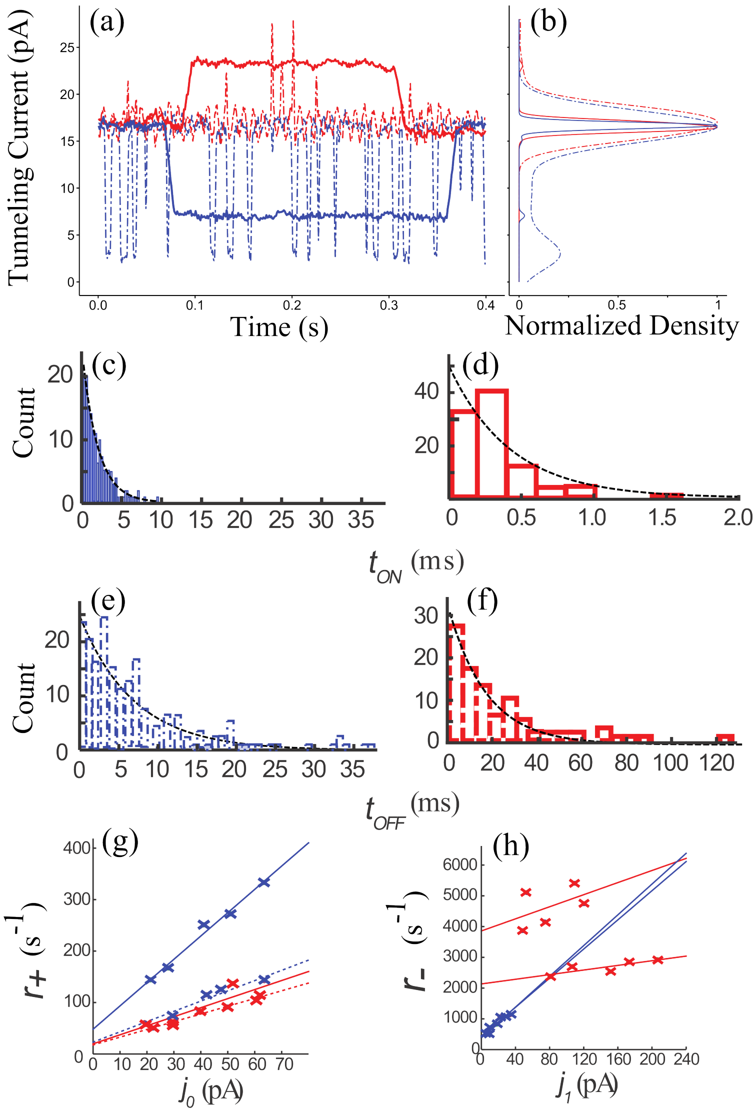

Figure 2.4: Reduction of the data. Time-traces recorded at $j_0 = 20$ pA and $V_b = 2.2$ V, on the four numbered contacts in (a) are shown in (b). The contact points are off-centered from individual lobes to maximize the switching activity as illustrated in Figure 3b. The traces are vertically offset for clarity. (c) Bimodal pulse height distribution at T4 identifies dichotomous negative switching. (d) The PHD at T3 shows a distribution of on states amplitudes, due to response time limitation. (e and f) Histograms of on/off-time distributions at T4 and T3 show Markovian distributions (exponential fits). (g and h) The linear current dependence of the extracted transition rates, $r_/pm = {}^1/\tau_{0/1}$: (g) r_+ vs j_0 and (h) r_- vs j_1.

The oscilloscope traces were imported into R, a freely available software, and ON/OFF discriminator lines were imposed 4 standard deviations from the OFF current baseline (j_0). The ON current level, j_1 is slightly more difficult to determine since the positive switches are short-lived, and so the ON states are ill-defined. Potential sources of error that were quantifiable and integrated into the analysis were the rise-time of our preamplifier, and the noise level in the current. Once the ON and OFF current levels are calculated, we obtain the frequency of switching.

2.3.1 Kinetics

Our model is that of a simple opposing reaction mechanism, with rate constants for the reverse and forward rate defined conventionally. Let us consider a two-state system, in which we go from a state 0 to a state 1, (*e.g.*, conductance states):

$$0 \underset{r_-}{\overset{r_+}{\rightleftharpoons}} 1 \tag{2.1}$$

where $r_\pm$ denote the forward and reverse rate constants. They are related to the time an electron is said to reside in each potential well by a decay parameter, τ:

$$r_+ = 1/\tau_0 \tag{2.2}$$

$$r_- = 1/\tau_1 \tag{2.3}$$

These can be refined to define the decay time from one state to another by a simple exponential decay, and thus the probability as a function of time of being in either the ON or OFF (1 or 0) state:

$$P_{0/1}(t) = \frac{1}{\tau_{0/1} e^{-t/\tau_{0/1}}} \tag{2.4}$$

These rate constants are further decomposed into spontaneous and stimulated portions:

$$\begin{aligned} r_+ &= j_0\sigma_{01} + k_{01} \\ r_- &= j_1\sigma_{10} + k_{10} \end{aligned} \tag{2.5}$$

where σ can be understood as a type of quantum yield describing the number of switches that occur per injected electron, and together with the ON or OFF current levels, j_1 and j_0 respectively, describe the current-driven rate of switching. The intercepts for each process, k, describes the spontaneous switching rate. We obtain a value for the rate constants by plotting $\tau_{0/1}$ against the current levels $j_{0/1}$ and obtaining a linear fit.

As mentioned, the extracted current-dependent linear rates are decompositions of the rate constants r_+ and r_-. A table summarizing the linear fits shows how the kinetics differ on each lobe. These data offer us another way or describing the curve-crossing associated with electrons spinning around on a JT-active surface.

Lobe	k_{01}	σ_{01}	k_{10}	σ_{10}
1	18.33	0.24	3859.07	1.57
2	23.25	0.32	383.31	4.00
3	19.843	0.28	2136.23	0.60
4	48.262	0.73	428.36	3.80

Table 2.1: Stimulated transition probability per electron (σ) in units of $(\times 10^{-6})/e$ and spontaneous rate constant, k

The spontaneous relaxation rate back to the ground state yields a consistent value on the BLs of $k_{10} = 400 \pm 30$ s^{-1}. However, k_{10} values recorded near the SLs are an order of magnitude larger and show greater sensitivity to topography and variation from molecule to molecule. Having established that the kinetics is that of a two-level system, a single spontaneous lifetime would be expected for the excited state. We recognize that the systematic variation in k_{10} is due to perturbation by the tip. Specifically, where the switching polarity is positive, the LDOS expands against the tip. Thus, Pauli repulsion can be expected to raise the potential energy.

2.3.2 Functional mapping and reconstruction of j_1 topography

Besides our kinetic analysis, we are also able to examine our degree of controllability in the experiment. Even though we are observing a stochastic process, we can control the rate of switching using the current and bias; the polarity of switch by tip placement; and the duty cycle of the switch.

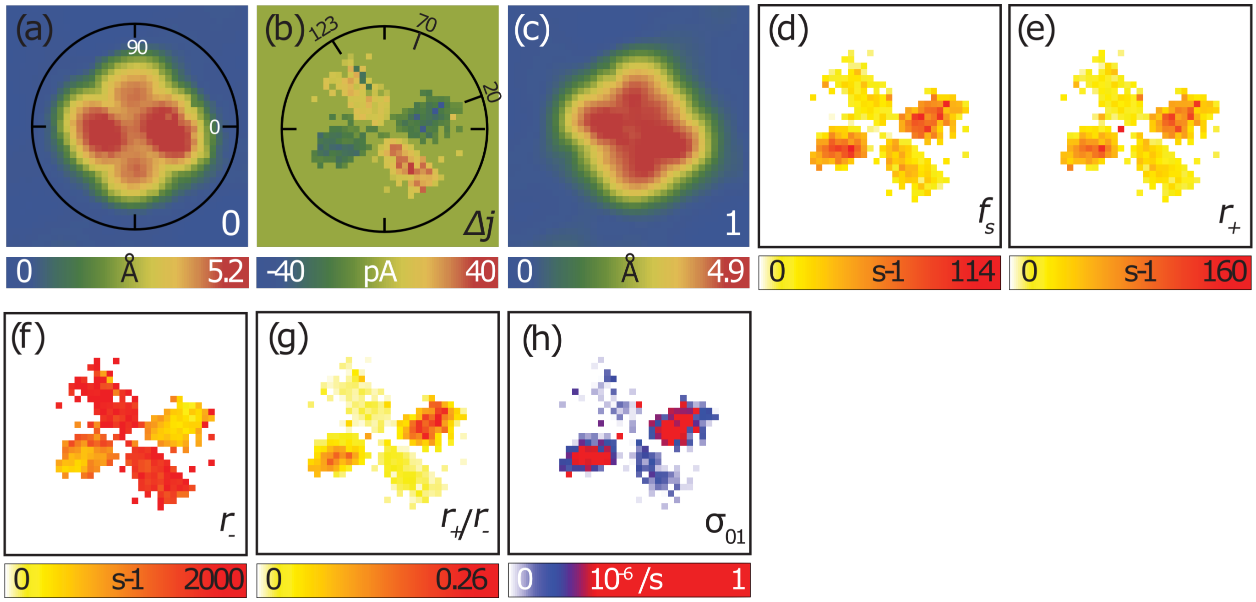

Figure 2.5: (a) 42 Å × 42 Å topography of the 0-state, at $j_0 = 20$ pA; (b) the switching amplitude, δj; (c) topography of the 1-state; (d) switching frequency; (e) on-rate (r_+); (f) off-rate (r_-); (g) duty cycle (r_+/r_-); (h) stimulated transition probability σ_{01} map.

In Figure 2.5(c), the reconstructed state is understood as a constant current topography at j_1. Since the residence time for the ON current level is too brief to take a topography scan (taking, at a minimum with decent resolution, 30 seconds), we used the height of the switch, δj–the switching map– and the measured constant current image at j_0 (seen in Figure 2.5(a)), in order to obtain $j_1 = \delta j + j_0$. Figure 2.5(d) shows the overall frequency of the switching activity, while (e) and (f) break it down by r_+ and r_-. The duty cycle, the ratio between the pulse duration and the period of a square wave, is visualized in (g) and given by r_+/r_-. Finally, Figure 2.5(h) shows the scattering cross section as determined by the slope.

We explain the stimulated transition probability via spin-flip, induced by the scattering of tunneling electron near the dianion resonance. In the same subfigure, we see that there is a 4:1 scattering probability. Triplet and singlet scattering occurs on the SL and only singlet scattering occurs on the BL. These maps can be used as wiring diagrams for control of the single electron switch.

2.3.3 Angular Cross-correlation of EL and switching maps

We also set out to quantify the disparity between the switching map and the topographic map. The STM topography of the molecule studied is shown in the white circle in Figure 2.6. It has a clear saddle shape and bright electroluminescence, as seen in the close-up, part (b) of the same figure. The EL map of 2.6(a), shown in 2.6(c), and its closer-up (part (d)) show that, as stated, not all molecules electroluminesce and that the photons predominantly originate from the smaller lobes, labeled 1 and 3 in 2.6(b). To analyze the angular cross-correlation between these two pathways, first we normalized th EL map by the maximum difference in intensities, shown in 2.6(e). The switching map (Figure 2.6(f)) was normalized in a similar manner, and the "center" found (red dot in 2.6(e) and (f)). The switching map is rotated with about this point, and the switching amplitude is multiplied by the normalized EL map as a function of this rotation. The sum of the resultant intensity is then added pixel-by-pixel.

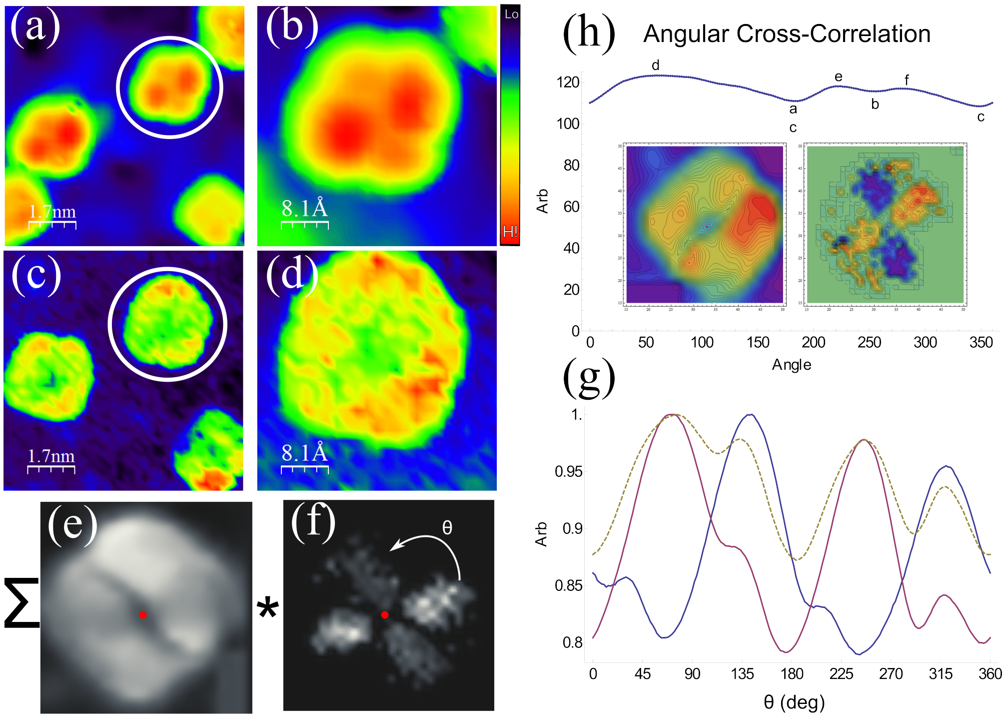

Figure 2.6: (a) STM topography of ZEP on NiAl(110) oxide and (b) detail of a single ZEP molecule. (c) and (d) are the corresponding EL maps. (e) Normalized EL map, used for correlation (f) Normalized switching map (g) Sum of correlation, positive and negative switching (h) result of angular cross-correlation.

When the positive and negative switching cross-correlation is plotted separately and compared to their sum, as in Fig 2.6(g), we note that the negative switching behavior dominates the correlation. Each lobe, regardless of switching polarity, exhibits a global minimum at horizontal depression highlighted in Figure 2.6(e), and a local minimum at the diagonal node, indicated by a red dot. In the sum of the contributions from negative and positive switching, the dominant minimum comes from the negative switching.

Focusing on the sum of the correlation behavior (gold, dashed line), we observe local minima at 112 and 290°, and local maxima at 184 and 358°. The least amount of correlation between the EL and switching maps occurs at ~ 0 and $\sim 180°$, which indicated that the two mechanism are spatially anti-correlated with a C_2 rotational symmetry.

2.4 Discussion

Our discussion begins by recognizing that an STM topography is a representation of the electron density of the molecule. The constant current STM topography of the OFF state can be measured directly–it is the static STM image. The ON state, which we see via a conductance switch, is transient, and exists for too short a time in for a traditional scan. We re-construct the ON state by recognizing that the additional splitting of the vibronic states is due to the phase accumulated with the electron orbiting about a singularity.

For any opposing reaction mechanism in equilibrium, we have the requirement

$$r_+[0]_{eq} = r_-[1]_{eq} \tag{2.6}$$

which means that equilibrium behavior is described by:

$$\frac{r_+}{r_-} = \frac{j_0\sigma_{01} + k_{01}}{j_1\sigma_{10} + k_{10}} \tag{2.7}$$

and the limit behavior further described by:

$$\text{as} \quad j \to \infty \quad \frac{r_+}{r_-} \to \frac{\sigma_{01}}{\sigma_{10}} \tag{2.8}$$

$$\text{as} \quad j \to 0 \quad \frac{r_+}{r_-} \to \frac{k_{01}}{k_{10}} \tag{2.9}$$

Consider now the spontaneous portion of the rate constant and its limit:

$$\lim_{j\to 0} \frac{r_+}{r_-} = \frac{k_{01}}{k_{10}} = e^{\frac{-(E_1-E_0)}{k_BT}} \tag{2.10}$$

The spontaneous switching rates are extracted from the intercepts of the linear fits to the observed on- and off- rates. Recasting this equation, and noting that the measurements are carried out at $T = 4\ K$, we obtain:

$$\Delta E = -k_B T \ln\left(\frac{k_{01}}{k_{10}}\right) \sim 1\text{meV} \tag{2.11}$$

The small energy difference ($\sim$ 1 meV) and the long lifetime of the switches may seem contradictory. However, here is where we build on the previous knowledge introduced in Section 2.1. The dynamic JT effect and vibronic coupling introduced energy levels described by half-integer angular momenta (l). In light atoms, which is the case for an electron in π orbitals, spin–vibronic coupling is weak. The observed 1 meV splitting is quite sensible for the effect. Previous calculations have estimated the zero–field splitting of ZnEtio anion at 0.1 meV [115]. Despite the small magnitude of the effect, the attendant change in topography is clearly observable through STM. This is the hallmark of topography determined by vibronic density.

The classical inversion of the spin–vibronic potential will yield a useful visualization of the ground and excited states (OFF and ON in the language of our kinetic analysis). The form of V is established and given explicitly in Equation 2.12 [116]:

$$V = \frac{1}{2}k_1 Q_1^2 + \frac{1}{2}k_2 Q_2^2 + cQ_1Q_2 + aQ_1 + bQ_2 \pm \sqrt{\lambda^2\left(c_1Q_1 + \frac{\delta_1}{2}\right)^2 + \left(c_2Q_2 + \frac{\delta_2}{2}\right)^2} \tag{2.12}$$

in which $c_{1,2}$ and $\delta_{1,2}$ represent the JT–coupling and crystal field splitting parameters, respectively. The coupling between modes is given by the parameter cQ_1Q_2, and accurately describes the observed chirality of the density. The tilt of the conical intersection is controlled by the slopes given by the parameters a and b. The energy scale is established by the active vibrations, through the force constants, $k_{1,2}$. The vibronic eigenstates are the doubly degenerate pseudo spin states $\Psi = \psi \exp^{im\phi}$ with $m = (1/2, 3/2, \ldots)$ as derived originally [84]. With the parameters given in Table 2.2, we are able to reproduce the potential energy surfaces and density of the 0 and 1 states (Figure 2.7)

Table 2.2: Fitting parameters extracted from the topography fit via potential surface generation for Figure 2.7

	k_1	k_2	c	a	b	c_1	c_2	δ_1	δ_2	λ
Ground (0 state)	1.08	1.10	0.06	0.18	0.36	7.19	6.33	7.33	4.53	23.80
Excited (1 state)	1.01	1.11	0.08	0.03	0.41	6.44	6.23	-0.53	2.48	24.55

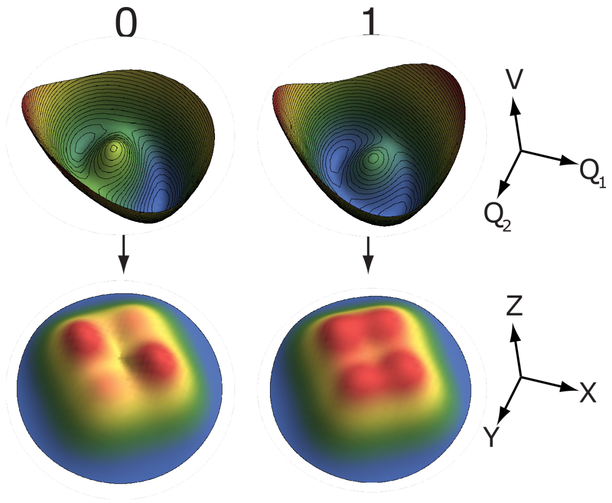

Figure 2.7: Adiabatic potential energy surfaces and density of the spin-vibronic states along the vibrational coordinates (Q1,Q2), and the observable electron densities they sustain along Cartesian coordinates.

We may conclude from our analysis that the spin-flip transition is resonantly induced by electrons that scatter on the dianion states. From a group theoretical perspective, we can also justify our conclusion by recognizing that the accessible dianion states are $E_g \otimes E_g =^1 A_{1g} +^1 B_{1g} +^1 B_{2g} +^3 A_{2g}$ given by the $2E_g$ parentage of the spin-aligned electron [117]. While the triplet state preserves spin alignment, scattering via the singlet states does not, as depicted in Figure 2.8(a). In the prior analysis of the EL, we derived the propensity rule that the injection of a second electron in the BLs leads to states of double occupancy, $e_g^2 e_g$, while injection in the SLs leads to JT-inactive states of single occupancy $e_g e_g$ [113]. Based on this statistical consideration, the spin-flip probability of 5:1 between BLs and SLs is in near quantitative agreement with the 4:1 ratio observed in the switching probability map $\sigma_{01}(x, y)$ in Figure 2.5(h). The small yield of the process, $\sim 10^7$ per tunneling electron, aptly describes the random telegraph noise character of switching.

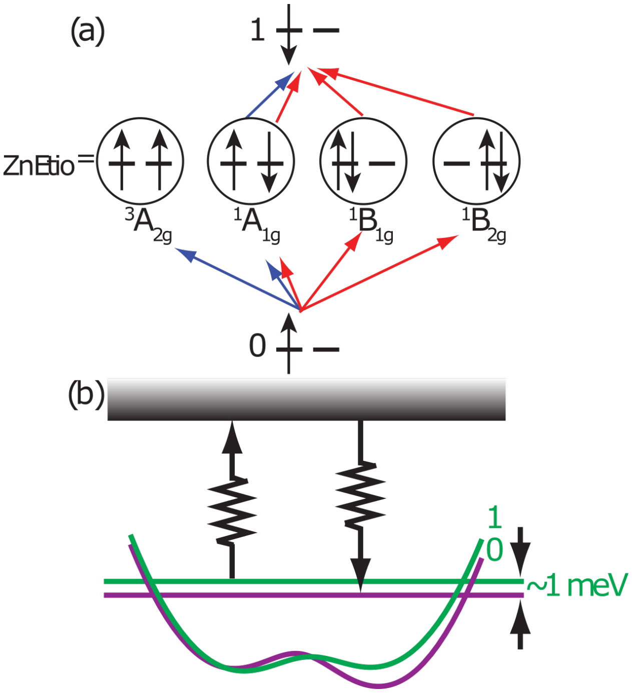

Figure 2.8: (a) Spin-flipping via scattering of tunneling electrons on the dianion resonance. Triplet/singlet scattering chan- nels on SL are indicated by blue arrows, and singlet scattering channels on BL are indicated by red arrows. (b) Spontaneous transition through the Orbach process.

Finally, we note that the spontaneous switching transitions, which dominate the 1 → 0 spin-flip relaxation, are expected to proceed without dissipation. Given the phonon bottleneck at 1 meV, the spin-lattice relaxation is forced *via* the Orbach process depicted in Figure 2.8(b). The two-phonon process involves resonant absorption and emission, with optical phonons of the oxide substrate most likely to serve as the resonance.

Chapter 3

STM as a tool for analyzing molecular motion

3.1 Background

The ability of STM to not just image molecules, but induce motion and chemistry on surfaces, is well-documented. Initially, studies used the tip to physically push atoms and molecules laterally across the sample surface [118, 119]. Meanwhile, theoretical treatments have revelead the dynamics and different modes of atom and molecule translation [120]. The surface science of adhesion too has been readily converted to an experimental standard for STM [121]. The effects of molecular and atom motion on the appearance of the STM image have also been investigated [122, 123]. Study in this area has also yielded numerous results by various groups has captured molecular rotation prompted by high-voltage pulses in STM [124, 125]. Active sites are distinguished from the otherwise homogeneous crystal surface by the rotational motion of the molecules. Early efforts using inelastic electron transmission spectroscopy (IETS) results have been able to differentiate between one- and multiple-electron process which mediate the coupling of a vibrational mode to the unhindered rotational motion [55].

Our own foray into this field has focused on the mechanics of motion of [4-(phenylazo)phenoxy] hexane-1-thiol (ABT) on Au(111). Our particular flavor of azobenzene thiol consists of an azobenzene polar hard (two benzene groups stitched together by an azo bond) with a long thiolalkane tether (Figure 3.1).

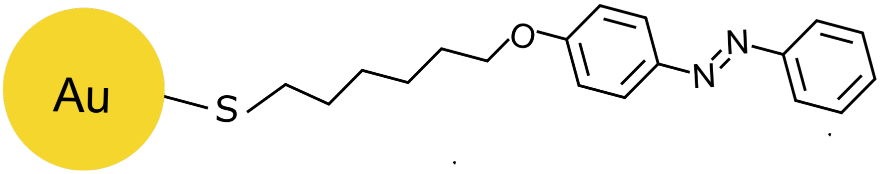

Figure 3.1: ABT shown with terminating gold atom

The general class of azobenzene thiols are well-studied azobenzene derivative, and is of particular interest in the field of molecular electronics [126, 127]. Rotation of thioether linkers can be actuated both thermally and mechanically [128], and temperature-dependent studies have quantified the rotational activation barrier [129]. Studies on single thioether molecular rotors have further characterized the rotational barrier to include contributions from steric hindrance [130] and van der Waals interactions [131]. Time-resolved studies on both thermal and electrical rotation find that the STM tip is an adequate, and greatly controllable external energy source to couple to molecular rotors [132]. Theoretical treatments have also been used to determine rotational barriers for small thioether molecules, in addition to minimum energy adsorption sites, and rotation mechanisms [133].

Clearly, to induce motion in an otherwise stationary state, the molecule must be energized above the restraining potential barrier, and the controlled activation of such motion represents the rudiments of molecular motors [134]. There is now extensive literature on such motors and action spectroscopy to characterize mechanisms at work [124, 135, 136, 137, 138]. The anchor is also important to consider: studies have found that both the length and conjugation of the tether affect the photoisomerization and other optical properties [139, 140].

In this chapter, I add another mechanism to the existing collection, in which low bias STM scanning induces rotation of ABT about its thioether linker. A previously stationary molecule on the elbows of the Au(111) "herringbone" reconstruction is set in motion as the sample bias is lowered near zero, prompting a new model for rotation. Based on previous work on lattice gases physisorption potentials on Au(111) [141], we have determined that the potential of the STM tip as it is lowered to the surface affects the overall potential landscape experienced by the molecule, thereby inducing hindered rotation. It is noteworthy that molecules assume very different states when sandwiched between surfaces, and the hovering state suggests that thiolated alkanes can minimize friction between gliding surfaces when unhindered by intermolecular interactions. Twirling can serve as a 2D bearing, whereby the molecular volume is extended from a rod to a disk. We demonstrate this distinct mechanism as an alternate design principle for molecular motors and suggest it as an approach to lubrication of interfaces that can be applied in nanomechanics [142].

3.2 Experimental Details

The experiments are carried out in a low-temperature ultrahigh vacuum (LT-UHV) STM, at $T = 80$K. The Au(111) crystal substrate was prepared by cycles of Ne+ ion sputtering (1.0 keV/ 14μA) for 15 minutes followed by 2 hour annealing periods at $T = 950$K, and generally prepared by the techniques described in Section 2.2. The ABT molecules were provided by Professor H. Kumar Wickramasinghe. We dosed ABT by heating to 83 ℃, and exposing the sample for 3 seconds.

3.3 Key Observations

3.3.1 ABT adsorption and apparent "hovering" on Au(111)

The sputtering and annealing cycles leads to the familiar 22 × $\sqrt{3}$, or herringbone, reconstruction [143]. The dark trenches between the soliton walls are alternating hcp and fcc regions, as specified in Figure 3.2(e) .

At high coverage, ABT will lock onto the herringbone superstructure, as seen in Figure 3.2(a). Upon closer examination, we learn that ABT molecules will link together to extend the azo moiety medial to lateral; two sulfur bonds share a single Au adatom. The molecules are kept flat on the surface due to intermolecular interactions. In areas of little interaction, interesting shapes arise (Figure 3.2(b)).

At low coverage, ABT decorates the elbows of the herringbone (Figure 3.2(c)). A common logic applied to hetereogeneous catalysis is that defects are highly reactive sites, so this particular surface distribution is line with the common wisdom, particularly for the reconstructed Au(111) surface [144]. Despite the similarity in chemisorption sites, the molecule can be seen to assume a variety of orientational states, as seen in Figure 3.2(e). The straight molecules are aligned normal to the bisector of the herringbone elbows. In certain instances, it takes on a hexagon shape, reflecting the six-fold symmetry of Au(111) surface (Figure 3.2(b) and (d)). Several of them appear three-tined, reflecting hopping among three wells oriented at 60° relative to each other, arising from one half of a hexagonal unit. Clearly, these molecules encounter a potential barrier barring it from accessing all six wells. The intact ABT spans the width of the hexagonal domain, while the transition between the domains acts as a barrier to reorientation. There can be seen a few examples that complete the circle, or flip flop between wells that span a larger angular distribution, and one can immediately conclude that these are sites where there either point defects, or faults. The hexagons are shorter than the stationary ABT with a length more consistent with a truncated molecule consisting of just the azobenzene moiety. Evidently, some molecules decomposed while on the surface. The alkyl tails of these fragments form locked rafts that are shown in Figure 3.2(f).

In all these cases, the different orientational minima are thermally accessed, without the need to activate via electron scattering. There is range of biases in which these structures remain stationary, and at high enough bias it is possible to move a stationary molecule into one that traps in multiple minima as previously reported.

The distal benzene- medial benzene distance in ABT on Au(111) has been experimentally observed to be between 7 and 8 Å [145], stretched by as much as 27% relative to its value in the crystalline state. A full ABT molecule has a length of ~ 2 nm. This distance is seen in the tines and the rings, verified by line cuts across several shapes taken in Gwyddion visualization/analysis software. However, the spinners were about half a nanometer shorter. In Figure 3.3(c), the profile also shows a distinctive bump atop the molecular profile, indicating that there is a part of the molecule that is also taller than expected. We have concluded that this is most readily explained by having the proximal benzene is tilted with respect to the distal benzene group. In effect, in the dynamic state, the AB head group has decoupled from the Au surface. This we have termed "hovering," to indicate that the bias-dependent rotation occurs when the AB moiety lifts from the surface.

3.3.2 Bias-dependent apparent "twirling"

We investigated the bias dependence of the various shapes to study the role of the potential energy landscape in producing STM images. We sought to know the relationship between the dynamical information afforded by the STM, and the image observed. In Figure 3.3(a) and (b), we show a side-by-side comparison of the same area imaged at 250 mV and 5 mV.

Initially stationary ABT molecules will now appear as concentric disks. A line cut across the stationary molecules shows that these are the length of an entire ABT molecule. Specifically, the length of the rotating molecule from the middle protrusion to the edge is consistent with the length of an ABT molecule on Au(111), and the benzenebenzene distance is $\sim$ 5.2Å. The proximal benzene appears $\sim$ 0.3Å shorter than the distal benzene, which we conclude means that the molecule is no longer lying completely flat on the surface (Figure 3.3(d)).

The concentric rings can therefore be assigned to ABT molecules anchored at the sulfur bond while their AB headgroup traces a circle, and the benzenes stand on edge. To differentiate between the spectroscopic definition of molecular rotation, which requires motion about a rotational inertial axis, we have termed this motion “twirling.”

In contrast, the three-tined image becomes a filled-in disk upon dropping the bias from 500 mV to 50 mV and 5 mV (Figure 3.3(e–g)). In this case, we have captured an ABT molecule in which the benzenes remain flat while the molecule attempts to twirl. The orientational images follow principles of motional averaging, and are distinct depending on their hovering state.

3.3.3 Morse potential model reveals minimum energy adsorption geometry

Induction of motion by reducing bias at constant current (15 pA) cannot be attributed to kinetic activation, since inelastic electron scattering would necessarily scale with flux (current) and energy (bias) of tunneling electrons. We must conclude that the mechanism involves the lowering of orientational barriers, or, as commonly known to the chemist, catalysis. As noted in Section 3.1, the activation barrier to rotation on the surface has already been estimated and measured [132]. However, these measurements neglected to estimate the barrier at very small biases. Recall that the relationship is between tunneling current and tip-sample distance is given by Equation 1.1. Contained within the constant κ is the term $\sqrt{E - U_z}$, which roughly contained the sample bias. As bias drops, the tip approaches the surface.

We modeled the sample-tip region as two Morse potentials slowly converging. How the combined system make affects the orientation of the molecule with respect to the sample surface and therefore the potential it experiences can be thought of similarly to a lattice gas on the surface of gold. From this starting point, we defined the Morse potential for an atom-surface interaction where the zero of energy is arbitrary in Equation 3.1:

$$V = V_0[\mathrm{e}^{-2\beta(z-z_0)} - 2\mathrm{e}^{-\beta(z-z_0)}] \tag{3.1}$$

with exponential range parameter $\beta = 1\,\text{Å}^{-1}$, binding energy $V_0 = 0.8(0.4)$ eV and equilibrium distance $z_0 = 3.4(4;5)\,\text{Å}$ for flat and on-edge adsorption. The difference in z_0 is principally due the dimensions of benzene. Since we are concerned with the tip-molecule distance, and in STM we measure presumably from the sample, we take into account the fact that the distance as measured from the middle of the benzene ring to the tip will be different in these adsorption geometries. In the flat geometry, z_0 is the Au-C distance, and in the on-edge geometry z_0 is measured from the center of the benzene ring. The computed binding energy of 0.8 eV is known to overestimate the experimental value of 0.62 eV [141]. We construct the potential of the sandwiched molecule as a simple sum of $V(z)$ as shown in Equation 3.1 and $V(d-z)$ where d in the inter-plane separation.

In Figure 3.4, the black curve is the modified Morse potential described by Eqt 3.1 and describes the potential experienced by the azo head group when laying flat on the surface (parallel on surface). The left side of the curve is the metal sample, the right is the metal tip. Both are described by the same equation in this schematic, but approaching from opposite sides of the abscissa. The orange curve is the potential well benzene falls into, describing when it is standing on its edge ("on-edge"), perpendicular to the metal surface. This is the higher-energy orientation when the tip-sample potential interaction is low. Benzene lies flat on the sample at large (greater than ~ 1.2 nm) tip-sample distances.

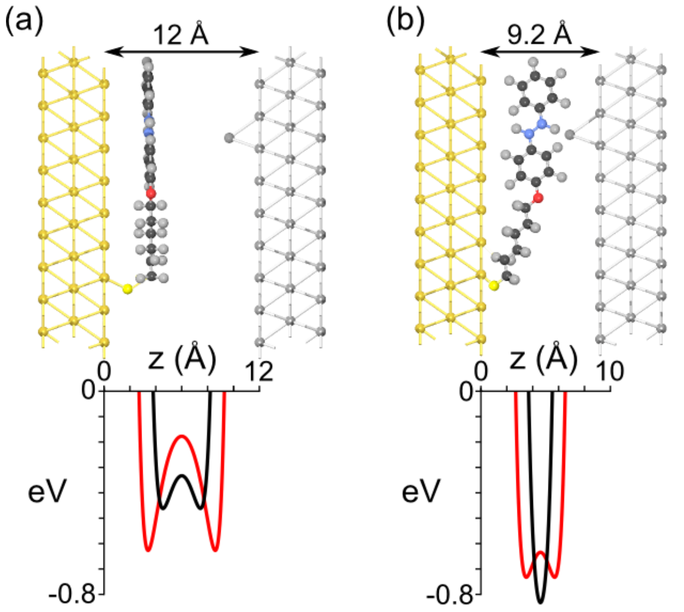

Figure 3.4: (a) When far apart, the molecule lies flat on the Au surface (red potential). (b) Upon reaching a separation of 1 nm, the molecule lifts to its on-edge geometry (black potential) and falls in the hovering well, consistent with the concentric rings seen in Figure 3.2(b). The same Morse potentials are assumed for physisorption on either surface, and to be consistent with observations, the binding energies are adjusted to $V_\circ = 0.62$ eV and 0.52 eV for flat and on-edge adsorption, respectively.

At large separations between the planes, $d >> \beta^{-1}$, benzene lies flat on Au(111), at a height $z_0 = 3.4\,\text{Å}$ from the Au surface. In this limit, the theoretical energy difference between flat and on-edge adsorption is 0.4 eV ($58\,k_BT$ at 80 K); therefore, the molecule is strictly in the flat stationary state. Moreover, the potential for flat physisorption remains the global minimum, independent of the separation between the two surfaces. However, if we use the experimental binding energy of 0.62 eV for flat adsorption and retain all other parameters, the standing state becomes the global minimum for $9\text{Å} < d < 10\text{Å}$. This holds over the curved surface of the tip, for typical apex cone radii $R > 10$ nm[1]. A more consistent picture is obtained by reducing the difference in the Morse minima to 0.1 eV, by setting $V_0 = 0.62$ eV and 0.52 eV for flat and on-edge adsorption Equation 3.1. With this modification, the molecule hovers at a height of $z = 3.4 - 8\text{Å}$ from either surface for a significant range of gaps, $8.4\text{Å} < d < 11.5\text{Å}$ (Figure 3.4(b)). All lateral potential corrugation is eliminated at such a height, as evidenced by the subsequent twirling.

---

[1] The gap range Δd over which the on-edge potential is lower in energy is given by $\Delta d/2 > R(1 - \cos(\tan -1(L/R)))$, where L = 3 nm is the length of the molecule

3.3.4 Analysis of STM images

Fit to hexagonal wells

The trapping potential of the hexagons and three-tined molecules can be extracted by the classical inversion of the observed density, by fitting to :

$$\rho(\theta) = N \exp[-(V_6(\cos(6\theta + \phi) + 1) + V_3 \cos(3\theta + \phi + \pi/3))] \tag{3.2}$$

where N is a normalization constant, and the potential heights, $V_{6/3} \equiv V/k_BT$. The STM images are normalized such that the Au metal surface is set to 0 nm. A circular cut around the circumference of the hexagon is taken and fit to Equation 3.1. The extracted values of the potential heights are averaged by stratified radial cuts. The entire data set stems from fits of 11 separate hexagons each with 3 to 10 values of radii for a total of 47 data points. The data extraction and fitting procedure is illustrated in Figure 3.5.

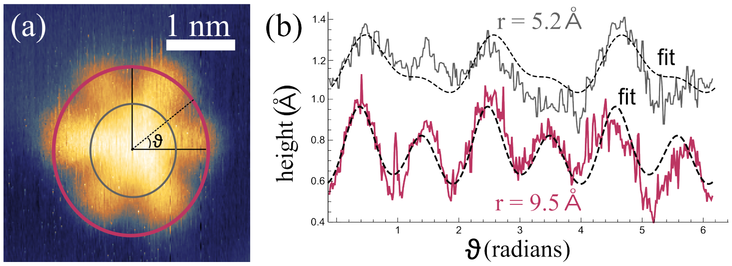

Figure 3.5: (a) The topographic image of the hexagon and (b) its angular profile at $r = 9.5$Å (pink trace) and $r = 9.5$Å (grey trace), and fit to Equation 3.2 (dashed black trace).

The particular radii 9.5 and 5.2 Å were chosen due to the consistency of the data. Not all data points had physical meaning as well. Some of the lower resolution scans had a signal-to-noise ratio (SNR) that predicted negative values of $V_{6/3}$. Those data points that were unphysical or had substantial errors associated with them based on adjusted R^2 values were excluded.

The most informative part of Equation 3.2 is the ratio in the argument of the exponent: $V_{6/3} = V/k_BT$. If V/k_BT is very large ($V >> k_BT$), then the potential experienced by the molecule is so large that we would not expect to see any movement on a timescale similar to the scanning times of the STM. Similarly, a very small value of $V/k_BT \rightarrow V << k_BT$, and therefore we would expect the molecule to appear "delocalized" over the surface, instead of in discrete wells. From the data set culled from the larger data set, the fits at $r = 9.5$ and 5.2Å yield average values of $V_6 = 0.16 \pm 0.03\, k_BT$ and $V_3 = 0.08 \pm 0.02\, k_BT$ (Table 3.1).

Table 3.1: Summary of values for $V_{6/3}$ in k_BT for six hexagons with common radii, which yield an average of 1.5 k_BT

radius	V_6	V_3
5.2Å	0.17	0.11
	0.22	0.10
	0.25	0.10
	0.17	0.062
	0.15	0.062
	0.12	0.10
9.5Å	0.11	0.04
	0.17	0.07
	0.15	0.10
	0.13	0.09
	0.12	0.08
	0.16	0.08
mean (mean dev)	0.16 (0.03)	0.08 (0.02)

Forward simulation of Gaussian convolution

A significant convolution of the tip profile and the molecule would obscure the true value of V/k_BT. We set out to determine if the apparent density captured in the STM image is the real density, or if the density has been significantly widened by the effect of the tip.

An example of a possible result is shown in Figure 3.6.

$$\underbrace{f(x)}_{\text{“true” image}} \diamond \overbrace{g(x)}^{\text{Gaussian function}} = \underbrace{\int_{-\infty}^{\infty} f(x)g(x-y)\mathrm{d}x}_{\text{STM convolution}} \tag{3.3}$$

In order to reproduce this convolution, an average of 3 line profiles from the STM images of stationary ABT molecule were modeled as $g(x)$ in Equation 3.3 :

$$g(x) = \frac{1}{\sigma\sqrt{2\pi}} \times \exp^{-(x-\mu)^2/2\sigma^2} + c \tag{3.4}$$

where σ is the full width of the Gaussian at half max (fwhm), and c is an offset that alleviates the constraint of having the Gaussian go to zero on both sides. To create a kernel with which to convolve, lists were created using various values of σ (increasingly wider Gaussian functions), and by introducing initial and final values of x, along with its increment.

For a forward simulation, a simplified version of Equation 3.2 was used:

$$f(\theta) = \mathrm{e}^{[-v(\cos(6\theta+A)+1)]} \tag{3.5}$$

and a similar list was created by choosing initial values of A and v that modeled the data. According to the convolution theorem, the convolution of $f(\theta)$ and $g(x)$ are related by their Fourier transforms:

$$\mathcal{F}^{-1}\left[\mathcal{F}\{f(\theta)\} \times \mathcal{F}\{g(y)\}\right] = f(\theta) \diamond g(y) \tag{3.6}$$

However, since the Fourier transform of the simplified equation is not analytical, the convolution must be done numerically. This was accomplished by using the ListConvolve command in Mathematica. The Gaussian list will be used as a kernel, K_r to convolve with the list generated by the sample equation, a_{s-r} and $\sum_r K_r a_{s-r}$ is computed.

In the forward simulation, I take the fwhm of the average Gaussian profiles, and convolute with the trial function in Equation 3.5. However, no matter how sharp the assumed trial function was made, the experimental topography could be generated. In fact, the same apparent density in the experimental STM topography can be generated by assuming $V = V_0\delta[\theta - n\pi/3]$ where δ denotes a delta function that occurs periodically with a six-fold potential, and convolving with a Gaussian of fwhm = 1.1 nm for the tip-molecule shape function. This determines that the width of hexagonal potentials is strictly determined by tip-sample convolution. Therefore, the potential energy landscape cannot be extracted from the hexagons.

Classical inversion of potential

Since the potential could not be extracted from fitting the hexagons, a different method had to be applied in order to make a quanitative statement about the potential overcome by the hovering molecules. We start by recognizing that STM images provide the probability distribution. The fact that we image density in all six wells means that all the wells are accessible, and that we see the distribution of molecules over these minima. We begin by recalling that to find the probability that a system is in some state, P_i, we need the occupancy numbers for all i (a_i) and the total number of systems (A). That is:

$$P_i = \frac{a_i}{A} \tag{3.7}$$

The task is the find the distribution of a_i that maximizes entropy, given the constraints of conservation of energy ($\sum_i a_i E_i = E_{total}$)and conservation of mass ($\sum_i a_i = A$). One finds:

$$P_i = \sum_i \frac{a_i}{A} = \frac{\mathrm{e}^{-E_i/k_B T}}{\sum_i \mathrm{e}^{-E_i/k_B T}} \tag{3.8}$$

Equation 3.8 is the probability that the state E_i is occupied, which is familiar as the Boltzmann distribution. The denominator is the sum over all probability. As mentioned, we see the molecule in the potential minima (*i.e.* highest density) and in the process of hopping over the barrier. Let us say the minimum of the potential is given by i and the largest inter-well barrier is given by j. The ratio of these probabilities would be given by $P_j/P_i = \mathrm{e}^{-(E_j-E_i)/k_B T}$. We note that the difference between the energies, $E_j - E_i$ is the depth of the potential given the amount of thermal energy available in $k_B T$. Since we capture in our STM image all six thermally accessible wells, we can in principle extract the minimum and maximum of the potential, V, by inverting the probability density:

$$V = -k_B T \ln(\rho/N) \tag{3.9}$$

where ρ is the density imaged by STM, and N is given by $\int \rho(x,y)\mathrm{d}x\mathrm{d}y$. We inverted the STM images of the tines, instead of the hexagons, since the wider angular separation of the tines makes the convolution effect less severe. In Figure 3.7, we show the apparent potential energy surface obtained by inverting the observed density (Equation 3.9). The difference between minimum and largest inter-well barrier is the observed corrugation of the potential, and is given by $E_j - E_i$ in the language used above to motivate the classical inversion. As seen in Figure 3.7, $E_i = -0.6\,k_BT$, and the largest barrier is $E_j = 0.9\,k_BT$. Therefore, $V = E_j - E_i = 1.5k_BT$. Indeed, the corrugation cannot be much larger, since benzene remains a lattice gas at much lower temperatures [146]. It is notable that the potential inversion yields a value of V 10 times the value we found by fitting the hexagons. Evidently, we are limited by the sharpness of the tip.

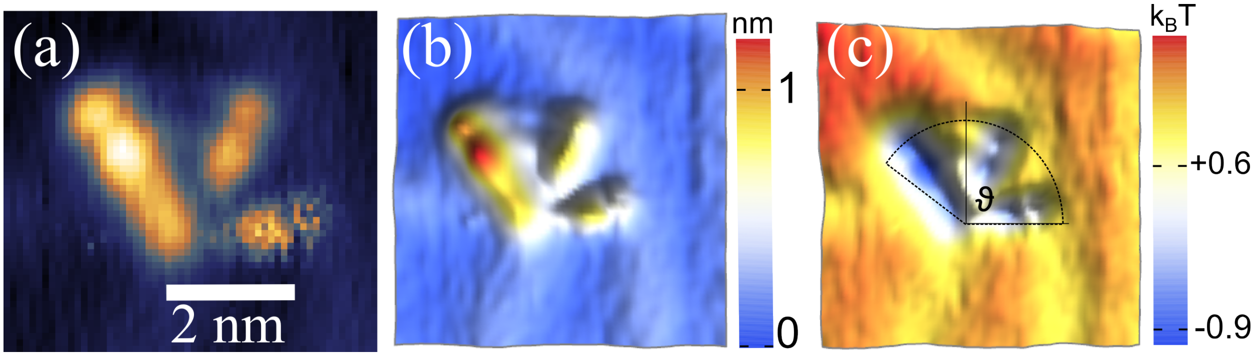

Figure 3.7: (a) The topographic image of the three-tined state, (b) its 3D rendering, and (b) its inversion, according to Equation 3.9, to highlight the corrugation of the potential energy surface, which reaches $1.5\,k_BT$. In the scale bar, the value of the minimum (-0.6 k_BT) and the largest inter-well barrier (0.9 k_BT) are explicitly indicated.

In conclusion, we identify twirling of long, tethered molecules induced by a competing Morse potential, which arises between surfaces that reach a separation $d \approx 1$ nm, equal to twice the physisorption height. In the specific case of ABT, we take advantage of the additional observation that the benzene rings stand up in the hovering state to characterize the potential. A rather soft potential is suggested by the Morse model, with a thermally accessible hovering range of $2 - 3\,\text{Å}$. A larger range is expected using a more realistic molecule-surface (*i.e.* Hamaker) potential, which scales as z^3 [147]. In effect, the present approach can be used to characterize van der Waals forces that are otherwise difficult to compute.

3.4 Proposed follow-up experiment

We used a Besocke (beetle)-type STM, which is mechanically stable with shear stacked piezoelectric elements [148]. Therefore, it would be interesting to conduct the following experiment: hover over a stationary ABT molecule at 250 mV sample bias and 20 pA tunneling current. Once the tip has stabilized, turn off feedback and observe change in current. With the feedback off, the tip experiences a change of distance when the molecule rotates or shifts under it, but the tip itself has not moved to compensate. Now, we can do the same bias dependent study by gently lowering the sample bias, and from the current trace, obtain a rotational rate as a function of tip approach. We can compare this to other measurements done in this field. Ostensibly the rate will change with alkyl chain length [131].

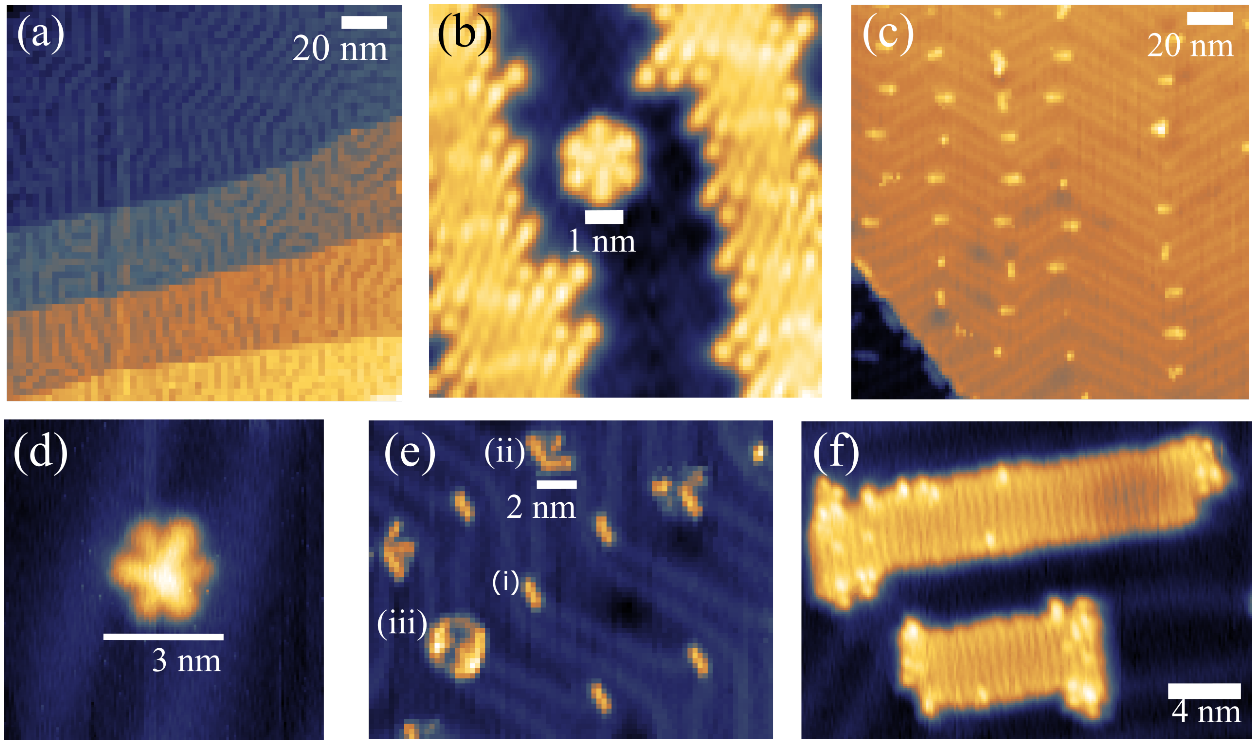

Figure 3.2: Topographic STM images of Au(111) decorated with AB thiol molecules. (a) Large-scale ($80\times80\,\mathrm{nm}^2$) scan at high coverage, where ABT forms an ordered phase locked on the herringbone superstructure. Lateral interactions eliminate motion and the molecules lie flat in the trans configuration. (b) An $8\times8\,\mathrm{nm}^2$ image in which the six-point star (hexagon) can be identified as an AB molecule hopping between six equivalent potential minima. (c) An $80\times80\,\mathrm{nm}^2$ image at low coverage showing ABT adsorbed at the herringbone elbows. (d) An $8\times8\,\mathrm{nm}^2$ scan of a different AB fragment seen at low coverage. (e) A $14\times10\,\mathrm{nm}^2$ image to highlight the variety of orientational states that coexist due to small variations in the landscape of the local adsorption site. These include (i) stationary linear molecules, (ii) the three-tined state of intact molecules that only sample three of the wells available on the hexagonal mesh, apparently blocked by the domain edge, and (iii) disks, in which the molecule is a nearly free rotor. (f) A $20\times14\,\mathrm{nm}^2$ image of rafts formed by the alkane tails cleaved from ABT. Sample bias = 0.25 V and tunneling current = 15 pA in all images.

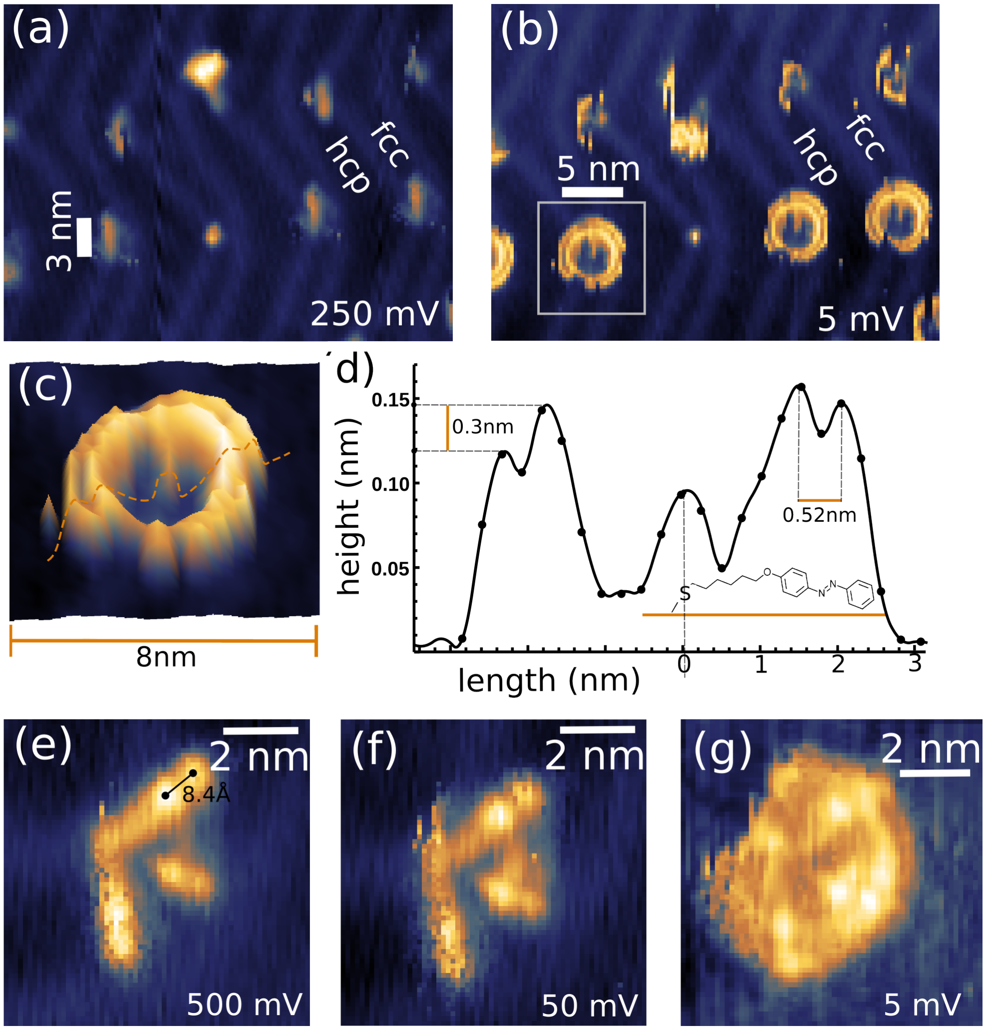

Figure 3.3: Topographic images recorded at constant current (15 pA) show the evolution of motion as a function of bias: (a) A stationary straight molecule imaged at 250 mV and constant current (15 pA) turns into (b) concentric rings at 5 mV, which is shown with 3D topographic detail in (c). (d) The cross-sectional profile of the dynamic state can be matched with the dimensions of an ABT molecule in which the benzenes are standing up. (e) The three-tined image at 500 mV begins to smear at (f) 50 mV, finally becoming a disk at (g) 5 mV.

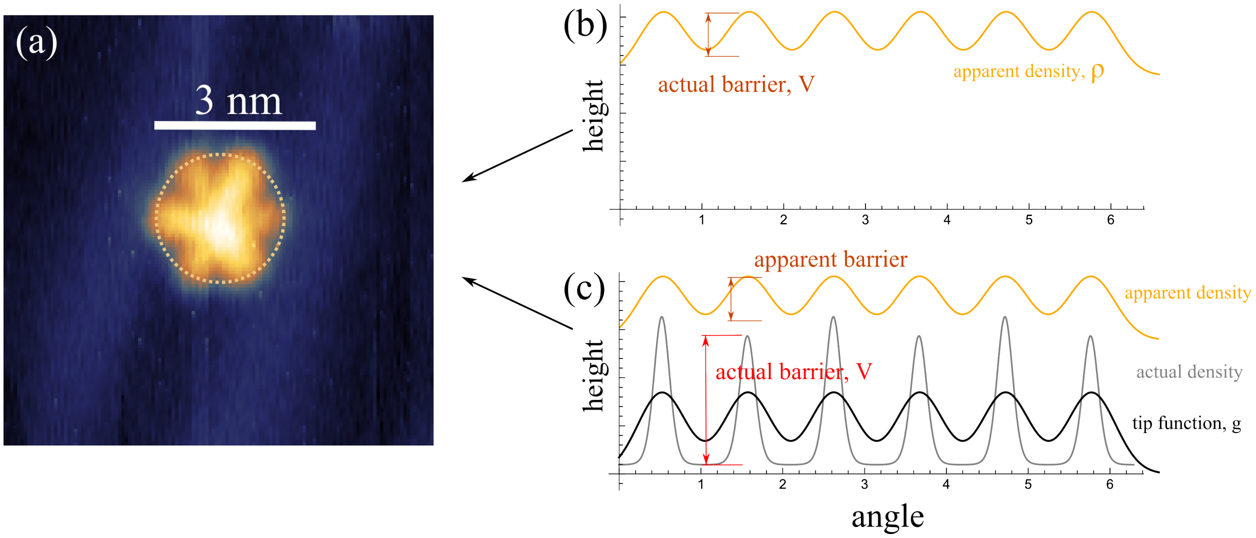

Figure 3.6: (a) An STM image of a hexagon that was analyzed shows a cut at 9.5 Å. The apparent density of the hexagon could be the actual density shown in (b), with a straightforwardly extractable barrier. However, in (c) the same apparent density can be created by convolving a much thinner actual density with a broad tip function. The difference between what we would obtain as the barrier, versus the real barrier, is illustrated. This motivates the forward simulation so we can determine how much we are limited by the sharpness of the tip.

Chapter 4

Single molecule isomerization: a study in two-level systems

4.1 Background

Following the initial musings present in Section 1.1.1, one may also consider the type of reaction necessary to stitch together the trajectory of a single molecule (random walker) based on a chemical reaction. For this, we require a repeatable, and ideally controllable reaction between two states. Immediately, the chemist lands on a structural (*e.g.* trans-cis) isomerization. For the appropriate molecule, the Raman spectrum should be distinct, and the lifetime of the process would be on the order of seconds, which can be captured by our CCD.

However, the physicist, in search of universalities, asks "Why?" In this case, the realm of photocatalysis lends an answer. The photocatalyzed trans-cis isomerization of ABT (Figure 3.1) has been studied in STM on a variety of surfaces and phases. In solution, isomerization of azobenzene (AB) occurs readily under UV irridation [149]. However, on coinage metals, a complex isomerization reaction pathway emerges. AB on Au(100) does not isomerize under the same conditions as in solution; but, isomerization is still observed if the coinage metal is Au(111). If we modify AB to include bulky tert-butyl groups adorning the outer edges of the pyridine constituents, the Au surface does not prevent its isomerization, but Ag(110) will [150] (Figure 4.1).

The curious case of the photoisomerization of AB and its thiolated derivatives on coinage metals ia an area of active research. Early on, the differences even between the types of substrates indicated that an enhancement mechanism plays a role in the reaction. Studies of AB-derivative films on planar and colloidal (*i.e.* nanoparticle) gold surfaces showed that single-component monolayer films prompts no reaction, but self-assembled monolayers (SAMs) and nanoparticle solutions do [151]. Further, SERS-active Au(111) surfaces have been shown to enhance photoswitching rates of AB [152]. The enhancement was characterized by monitoring the peak areas of the cis and trans isomers as a function of the light exposure time of both 364 and 450 nm sources. Both configurations exhibit a triplet near 1500 cm^{-1}, but have distinct intensity ratios. It has also been shown by IR reflection absorption spectroscopy that the lifetime of the cis configuration of AB moieties were reduced when retained on Au [153]. It is also possible to induce trans-cis isomerization of AB on an insulating surface using inelastically tunneling electrons [154]. The mechanism is attributed to the binding of the multipolar molecule to the ionic NaCl layer atop Ag(111). Generally, there are too many studies and conclusions to name: I recommend the interested reader seek a decent review by Bandara [155].

Because AB is promising for molecular electronics, many groups have studied its reaction pathways as a way to understand and manipulate the structure-activity relationship. For example, there are reports of molecular machines such as “molecular hinges” [156] and “molecular shuttles” [157] driven primarily by the trans-cis isomerization of an AB moiety embedded in large organic macrocycles. The rise of polymer materials has embraced large SAMs and materials made of AB-bsed materials [158]. For plasmonically active gold substrates, the energy transfer across the structure AB during photoisomerization has been shown to reversibly and controllably shift the wavelength of the LSP resonance [159].

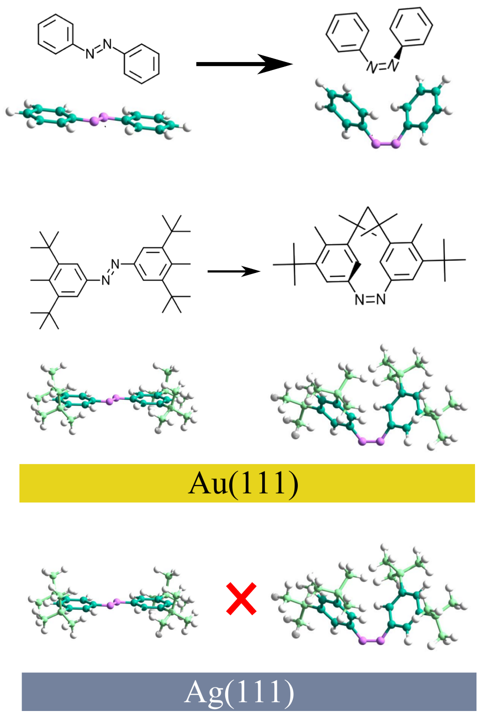

Figure 4.1: Photoisomerization azobenzene differs on coinage metal substrates

More fundamental, mechanistic studies have been simultaneously undertaken to bolster the application of AB-based materials. The trans-cis isomerization is instigated by mechanical stress [160], or electrostatic stimulation [161] in addition to photocatalysis. The cis-trans isomerzation occurs thermally due to the thermodynamic favorability of the trans isomer [126]. Early studies on matrix-isolated AB found that the thermal cis-trans isomerization of AB in the rigid monolayer film follow the same first-order kinetics as in solution phase [162]. The kinetics of the reaction was further elucidated by transient absorption spectroscopy, which determined that the thermal decay of the cis-isomers can be fitted by a sum of two first-order reactions with different rate constants [163]. The results were interpreted by balancing the contribution of the rotational and translational relaxation processes of alkyl chain segments of AB alkyl SAMs. The decay constants for S_0, S_1 and T_1 (lowest electronic states) were determined in 2004 [164, 165], and further refinement of conversion mechanisms were undertaken in matrix-isolated systems [166].

Early on, a pure Franck-Condon model for resonant Raman scattering on trans-AB was proposed to explain excited state molecular properties, but there remained disagreement between experiment and theory [167]. With new technologies, the excited state nuclear dynamics could be directly probed by analyzing resonance Raman line intensities. Trans-cis isomerization was found to proceed rapidly *via* rotation about the azo bond, whereas the cis-trans isomerization occurs primarily through inversion [168, 169]. Most importantly, our exact molecule, ABT had been shown to have nearly a billion-fold enhancement in Raman signal under stimulated Raman conditions in an AFM with 633 nm excitation laser [170]. Therefore, we expected to see a substantial Raman signal in a TERS geometry.

Based on the vastness of previous studies on surface-assisted photoisomerization of AB and its derivatives, we expected to obtain monolayers that stand vertically from the surface, thus fulfilling the requirement that the transition dipole be oriented along the tip dipole. We also expected to observe Raman spectra at 633 nm. But as most things in this realm, we did not get exactly what we expected.

4.2 Experimental Details

To obtain the Raman spectrum, we used the same parabolic mirror collection with 45° laser excitation (Figure 2.1). Around this time, we introduced two new aligning techniques. We added a pinhole to the spatial filter used to isolate the radiation scattered exclusively from the tip-sample junction. To align the excitation line, the telescope was modified with an XY adjustor to eliminate hitting the junction at a lateral angle. It is interesting to note that alignment after introduction with the XY adjustor yielded the data set for part of this chapter and also for Chapter 3. We sublime ABT molecules at $T = 353$ K and in UHV for 2 seconds onto the room-temperaure Au(111) substrate. The ABT-covered gold sample is then transferred to the STM. Over the course of approximately 2 hours, ABT settles on the surface and transforms into the self-assembled striped phase. The sample is then cooled to $T = 80$ K, allowing for high-resolution imaging of the striped phase surface.

To orient ourselves, I took a Raman spectrum of ABT in ethanol at 405 nm and 532 nm using

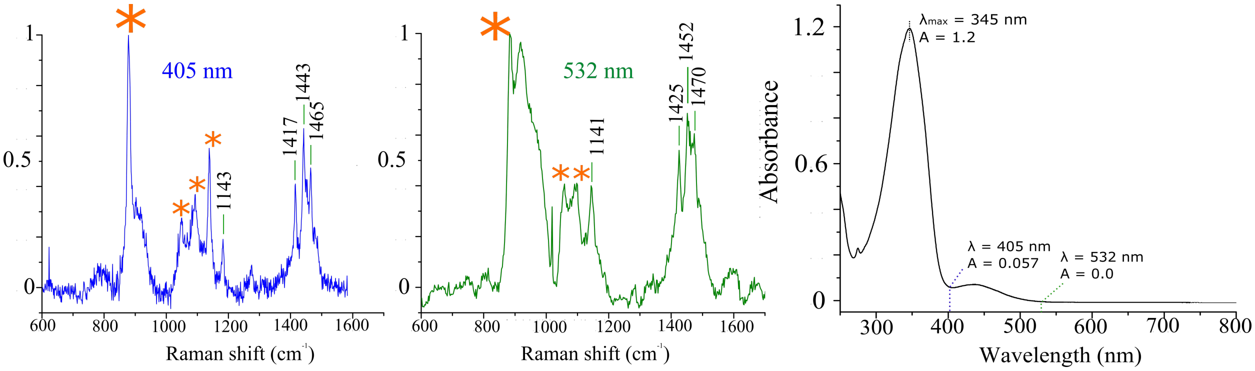

Figure 4.2: Raman spectra for ABT in EtOH note the expected line positions. UV-vis affirms that 532 nm is preresonant. The orange asterisks denote the solvent lines.

a Renishaw Raman microscope. The ABT spectrum matched the literature, and so affirmed the integrity of our sample. We also verified that we are presonant using 532 nm light by taking a UV-visible absorption spectrum with a Shimadzu UV-vis spectrometer (Figure 4.2).

4.3 Key Observations

4.3.1 Anatomy of ABT on Au(111) at high coverage

Overall, the anatomy of ABT on Au(111) was unexpected, and the fact that it ultimately did not stand vertically was cause for concern. ABT forms sub-monolayers that closely follow the herringbone reconstruction of the Au(111) surface using our dosing conditions. Even at high density, ABT lies flat on the surface, contrary to our expectation. The ABT molcules attached with their thiol tethers and extend outwards. At a bias of 3.1 V, the appearance of the common gold adatoms reinforces that the Au-S bond strongly tethers the molecule to the surface. Lateral dispersion interactions with molecular neighbors cause this snaking coverage of ABT on Au(111) (Figure 4.3).

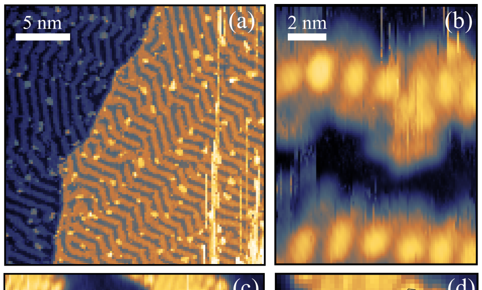

We used both 532 nm and 633 nm cw lasers. We did not necessarily expect photochemistry in the isolated molecule since 532 nm is preresonant; however, the d-s interband transition is accessible at 532 nm, and thus hole-mediated chemistry, or metal-molecule charge transfer induced chemistry, can be expected [171]. In addition, we are evidently sampling a huge number of molecules. From the molecule density per STM image size, we estimate that about 100 molecules are imaged in the larger scans. Through various days of experimentation, during which we changed laser excitation wavelength from 532 nm to 633 nm (and back), tried various laser powers, and excitation geometries, we were unable to capture the Raman spectrum of ABT on Au(111).

4.3.2 Stochastic spectral fluctuations

For much of the experiment, Raman signal remains elusive. Suddenly, without experimental prompting (*i.e.* sample bias change, current change, lateral or perpendicular motions of tip over sample), a wildly fluctuating Raman spectrum appeared. The fluctuations occur both in intensity and line positions.

Qualitatively, we observe several behaviors. In one instance, a line position appears to abruptly meander; in another, a line position blinks on and off; and finally, a strong line disappears altogether for the remainder of the trajectory. These behaviors are shown explicitly in the extracted portions of a trajectory in Figure 4.4.

For a more quantitative assessment, a trajectory recorded over a period of 1 minute shows

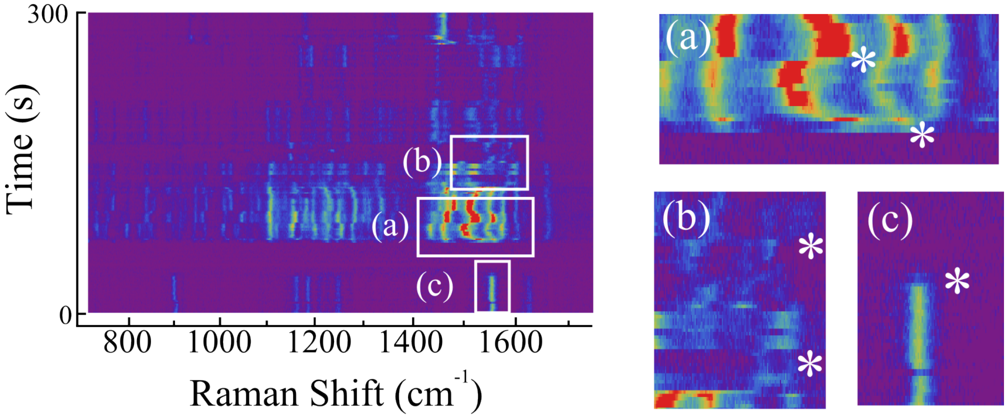

Figure 4.4: A Raman trajectory recorded for 300 second shows several abrupt, stochastic changes, indicated by white asterisks in extracted portions (a), (b) and (c).

the variety of spectra that can occur in rapid succession, particularly when zoomed into the 1500 cm^{-1} range (Figure 4.5(a) and (b)). Initially, we sought to establish that the spectral lines are indeed shifting substantially ("meandering"), and not within the noise expected of a vibrational spectrum. To do this, we use the linewidth of the spectral lines to provide a basis for understanding: if the wavenumber shift between two lines (pink $\Delta\nu$ in Figure 4.5) is larger than the linewidth (blue Γ_a), we say the peak has meandered.

There are two possibilities for such dramatic shifts: one, the normal modes which give rise to the spectrum have been altered by stiffening or loosening chemical bonds, indicating that we are observing a charge transfer process, or another process by which the bonds are changed; and two, the molecule is decomposing and changing as we observe the spectrum. The latter possibility is less likely, as it would require an initial spectrum that has many spectral lines that blink on and off. The bulk solid spectrum does not indicate that such a busy spectrum exists for this molecule.

On the other hand, fluctuating *intensities* in a spectrum indicate that the orientation of the molecule with respect to the local electric field is changing. If we are sensitive to this change, we must therefore be sensitive to the orientation of a single molecule in the local electric field of the STM junction. At this juncture, we also verified that the spectrum was tip-enhanced

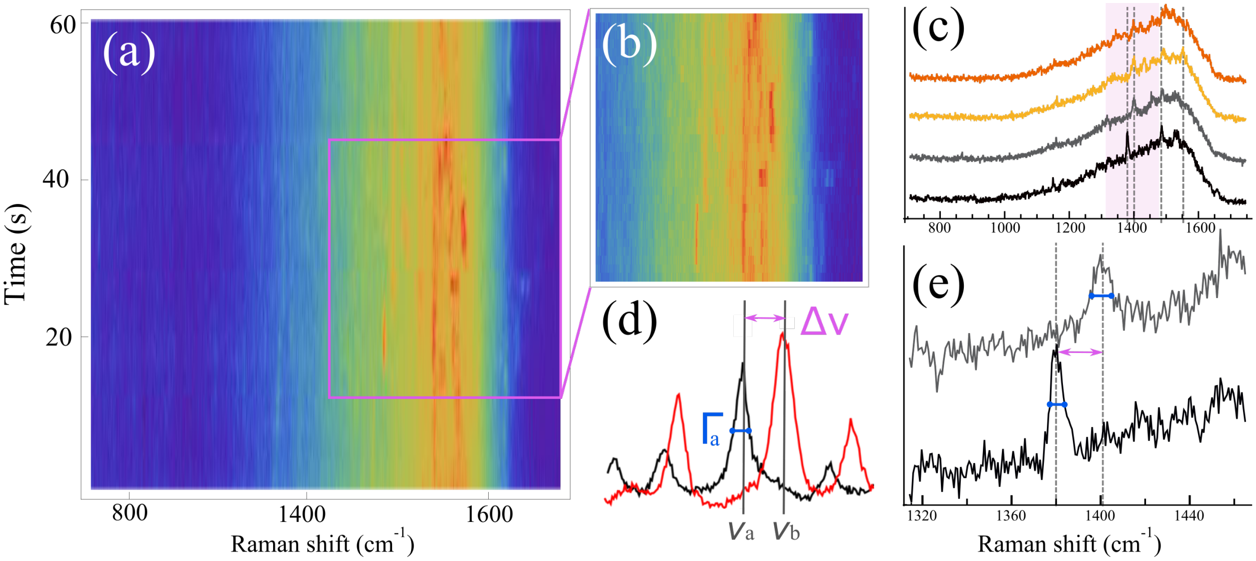

Figure 4.5: (a) A Raman trajectory taken at tunneling current = , sample bias =, laser wavelength = 633 nm and (b) a zoom in of a particularly active area. (c) Extracted spectra taken at 20, 25, 30, and 40 seconds showing the meandering of the Raman peaks. The gray lines denote the line positions at 1380, 1401, 1485, 1553 cm^{-1} The illustration in (d) defines "meanderer" and (e) shows the explicit meandering of the 1380 cm^{-1}.

(Figure 4.6). This indicates that the molecule we captured was susceptible to enhancement mechanisms.

The suddenness with which the spectra arrived smacks of hetereogeneous catalysis. The exact mechanism by which a huge number of completely reticent molecules would suddenly become quite vocal would have to be prompted by an event. The proposed explanation for this curious observation will be described after I continue to catalog the experimental observations (for the punchline, please refer to Section 4.4.3).

4.3.3 Bimodal spectral fluctuations

A second type of spectrum arose, in which it became qualitatively apparent that two apparently mutually exclusive spectra appeared stochastically. The figure is shown in black-and-white to better detail the two distinct spectra. With this aid, qualitatively we observe

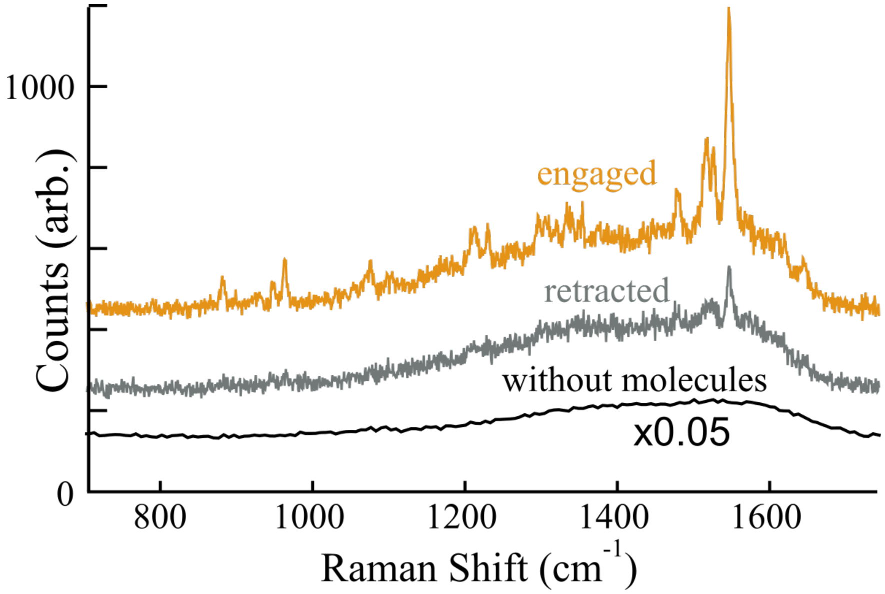

Figure 4.6: TERS of ABT evident by the strength of the line intensities in the engaged (orange) spectrum. This spectrum is taken while in the tunneling regime. To test the tip-enhancement, we retracted to about 100 nm from the surface, as which point the intensity dropped dramatically (grey). Finally, for comparison, what the magnified spectral intensity is before dosing with molecules is shown in black.

a spectrum with a strong doublet near 1500 cm^{-1}, and one with a strong mode near 1150 cm^{-1}. The trajectory and associated spectra are shown in Figure 4.7(a) and (b).

4.4 Analysis and Calculations

4.4.1 Statistics of bimodal spectral fluctuations

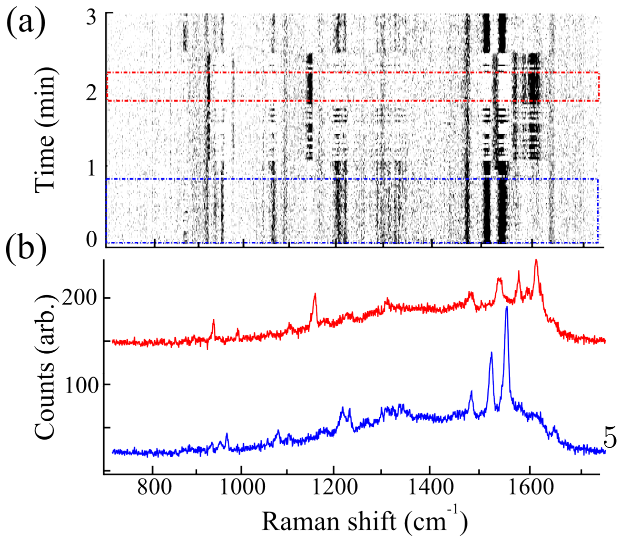

For Raman trajectories that appeared bimodal, we set out to assert this as fact by calculating discriminator lines following a similar formulation described in Section 2.3. The intensity of two distinctive lines – 1160 cm^{-1} and 1524 cm^{-1} – was tracked for the entire trajectory, and it was observed that when one spectral line was present, the other was completely silent. That is, the two spectra heralded by their characteristic lines occur in mutual exclusivity, or, are anti-correlated. Further, the histograms indicate a bimodal distribution for the two lines, or, a two-level system.

Discrete on- and off-levels to generate the histograms were determined by first calculating the means of the respective Gaussian distributions (x_{on} and x_{off}). Also required was the contrast between levels, n, given by the respective standard deviations, σ_{on} and σ_{off} (Equation 4.1).

$$n = (x_{on} - x_{off}) = (\sigma_{off} + \sigma_{on}) \tag{4.1}$$

The contrast n serves as a gauge of the certainty in state assignment. For the trajectory shown, the smallest value found was $n = 1.4$, which corresponds to 88% certainty. Two peculiar instances of switching states are the lines at 1484 and 1539 cm^{-1}. The line at 1484 cm^{-1} is shared by the two spectra; however, the histogram remains bimodal because the line is stronger in the blue state. The vibration at 1539 cm^{-1}, unlike other modes, is activated just prior to the rapid switching events and turns off once the switching ceases. The nature of this vibration is intriguing, since it appears to be connected to the trigger that drives the switching activity. Nearly all observed vibrational lines switch in synchrony, as illustrated by the Raman trajectory in Figure 4.8. The summarized analysis indicates that the spectra are bistable and anticorrelated, strongly suggesting a two-level system of a single molecule. Just as fluctuating intensity indicate a single molecule whose orientation relative to the local electric field is changing, so does a two-level system strongly specify a single molecule in two distinct states.

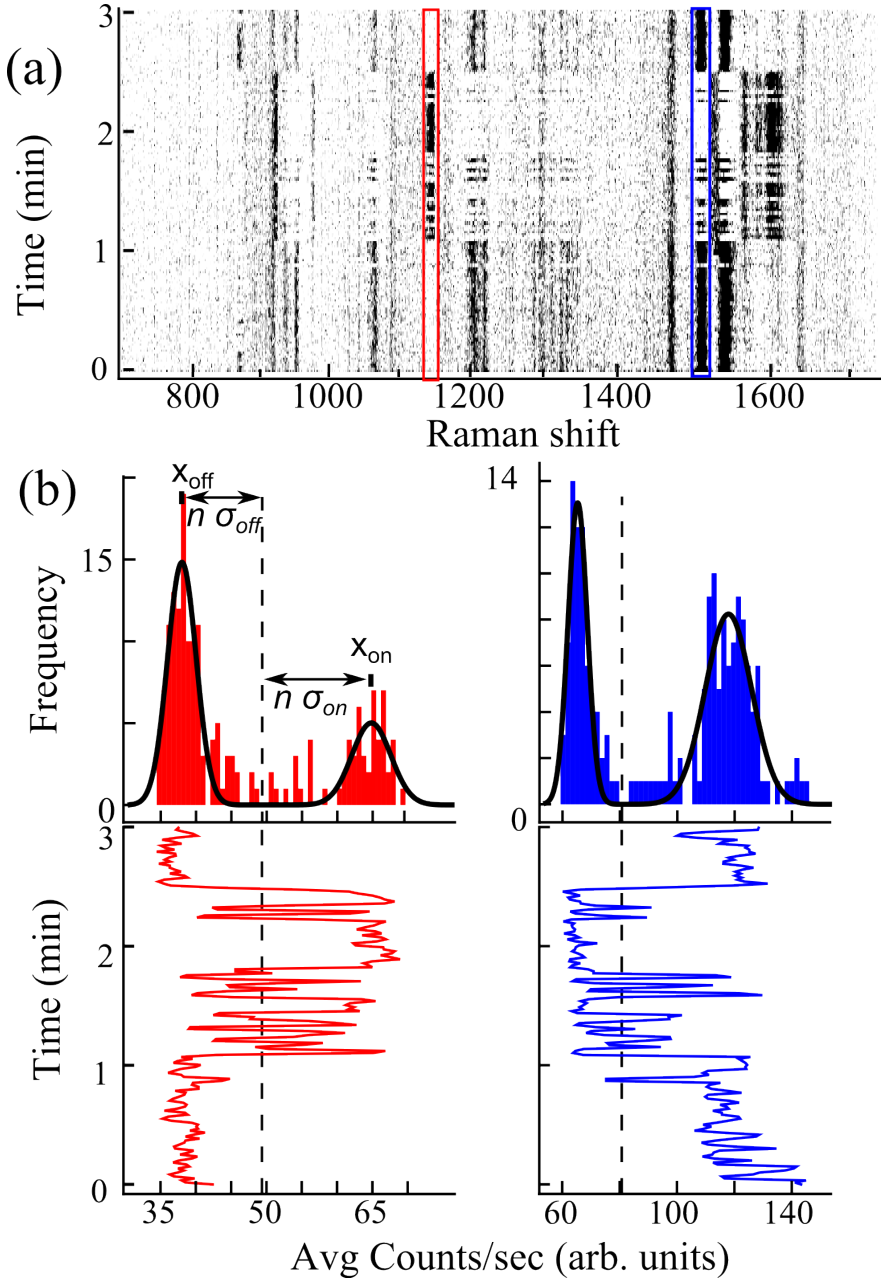

Figure 4.8: We created a bimodal intensity distribution of characteristic lines 1160 cm^{-1} and 1524 cm^{-1} using the same trajectory from Figure 4.7. We now outfit it with vertical red and blue boxes to exactly show the line positions. The bimodal distribution and discriminator lines are evident in (b). Below, a plot of the intensities over time show that they are anticorrelated.

A single, isomerizing molecule will exhibit random walk type of behavior, where it will stay in one state (isomer) for some time before hopping into the next state. In an ensemble measurement, we will end up averaging over all the random walks of each molecule, we will not be able to see the molecule in any particular state. When this experiment is narrowed down to a single molecule, we cannot see any state other than the one it currently is in. A two-level system can therefore only be expressed by a single molecule. Most generally, this study shows just how important it is to realize that the information contained in the time-averaged and ensemble-averaged results is fundamentally different from a single molecule. We conclude that all spectral features (save the two common to both spectra) above the noise floor belong to one of two anticorrelated states. Additionally, the off-level in both spectra corresponds to the zero baseline with greater than 95% certainty in nine of 13 observed lines. Therefore, with statistical certainty, only one of two observed spectra is present at any given time, and this holds for trajectories recorded over the period of a day.

Since the observed state lifetimes is anywhere from seconds to hours, the two spectra must be assigned to structural isomers of the same molecule. A different type of reaction would occur much faster. The red spectrum contains a strong peak at 1160 cm^{-1} and a triplet at 1536, 1574, and 1608 cm^{-1}. This pattern parallels the bulk trans-ABT spectrum, which contains a strong peak at 1144 cm^{-1} and a triplet at 1416, 1442, 1465 cm^{-1}. Therefore, we tentatively assign the red spectrum to the trans-ABT isomer, with ~ 100 cm^{-1} shift of the triplet in the chemisorbed state. The dramatic shift suggests that the chemisorption involves charge transfer between the AB headgroup and the metal substrate, directly modifying the charge density localized on the azo bond. By default, the blue spectrum must belong to the cis isomer.

The zero time delay cross-correlation map of these spectra is shown in Figure 4.9. The bimodal distribution, familiar to us from the single electron switch, immediately points to a single molecule undergoing a change between two distinct states. It also shows that the covariance based on the full statistics of the trajectory, underscoring the dichotomous nature of the process. All of these observations together can only be compatible with the isomerization of one molecule.

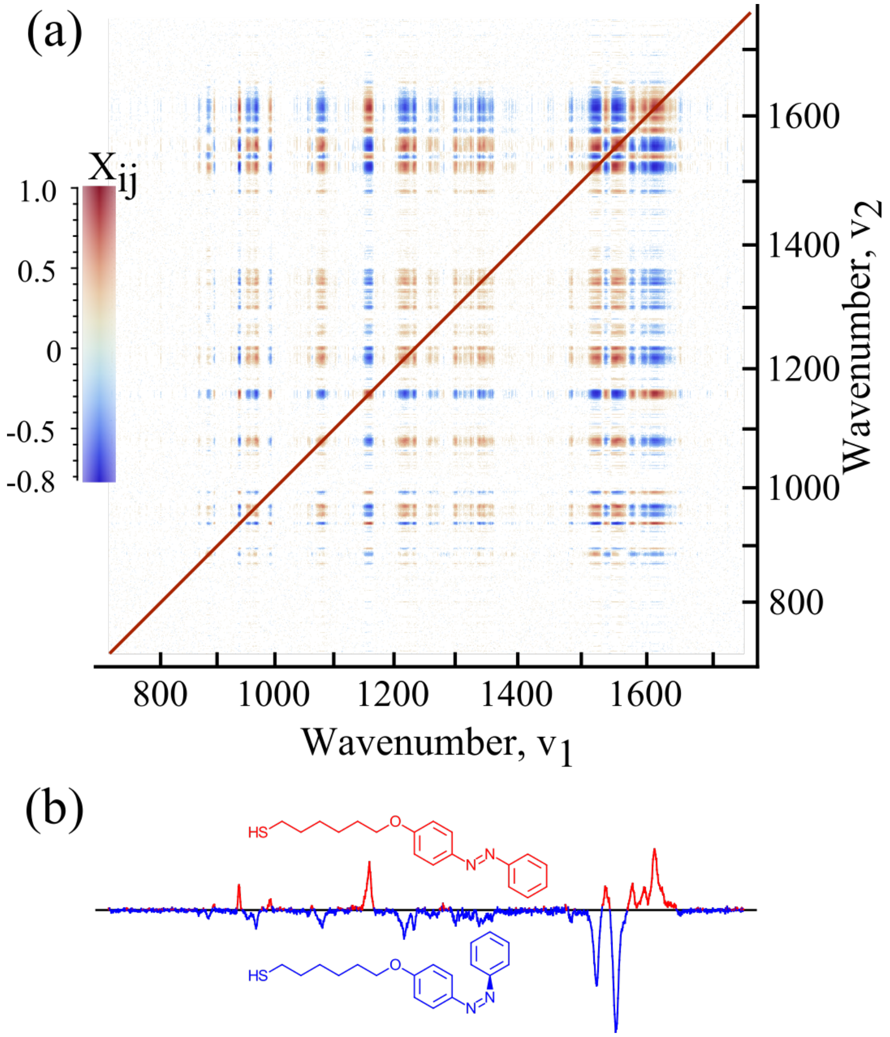

Figure 4.9: (a) The zero time delay 2D cross-correlation (X_{ij}) of the trajectory in Figure 4.7. Correlations that are not statistically significant (with less than 1 % probability of occurring by random chance) are colored white. (b) The zero time delay covariance, σ_{ij}, where $i = 1160\,\mathrm{cm}^1$ and $j = 1524\,\mathrm{cm}^1$, which shows the strict anticorrelation.

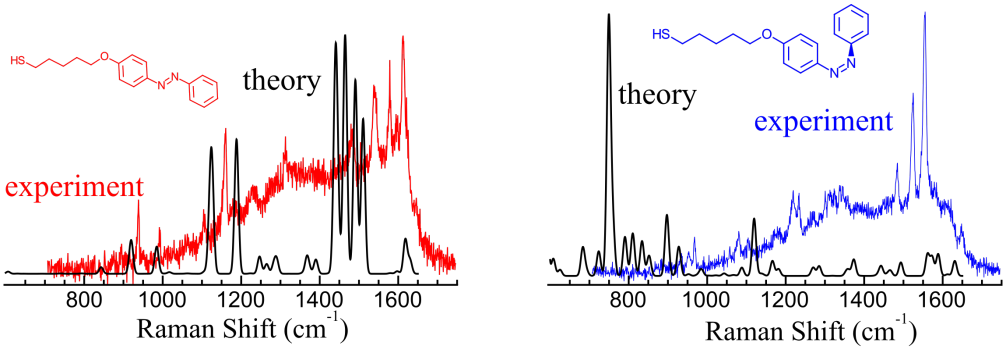

Figure 4.10: The calculated Raman spectrum generated by Turbomole did not agree well with the spectra we saw in Figure 4.7

.

4.4.2 DFT and polarizability calculations

To test our assignments, we turned to DFT for verification. The spectrum shown in blue does not neatly represent a currently known structural isomer of ABT. cis-ABT has several low modes at 540,595, 621, and 778 cm^{-1}. Notably, the blue spectrum does not have these modes, and instead carries just the characteristic high wavenumber modes. Evidently, we are sampling an isomer in an unexpected configuration. Initially, I used Turbomole 7.0 with 6-31G* basis set and and PBE functional to calculate the spectra, and ran several calculations with a positive/negative charge. However, localizing a charged is tricky in DFT, and yielded no significantly useful results (Figure 4.10).

It would be interesting to apply similar searches for contributing structures and charged species in the meandering spectra in order to reverse engineer a structure trajectory of how the molecule was shifting as we were observing its Raman spectrum.

4.4.3 Interpretation of Results

Such a stark contrast between the experimental control parameters and the initiation of fluctuating/meandering spectra indicate a process that underwent catalysis. Indeed, hetereogeneous catalyst by Ag atoms is not unheard [172, 173]. In particular, Ag atoms are known to be mobile even and LN_2 temperatures, and so it stands to reason that a Ag atom on the tip might have served as the necessary catalytic component to prompt a single molecule isomerization [174]. A single atom on a tip has also been proposed to act as a sort of “picocavity”, which may intensify generally weak Raman signals [21].

Therefore, to be able to explain all the experimental observations, we have concluded that a single ABT molecule was able to tether itself to the Ag STM tip, which served as a site of intense catalytic activity. This is why we observed characteristic single molecule behavior whilst hovering above a sea of Raman-inert ABT molecules.

Chapter 5

Combination bands in single molecule TERS

5.1 Background

In 2013, Zhang et al. [175] published a major breakthrough for the TERS community: Å-resolved Raman mapping for a single molecule. In their figure of merit, they found that their sharp EL spectrum with a maximum in the 1400-1600 cm^{-1} region is the crucial component to making this experiment work. The experimental success clearly indicated that, despite misgivings, spatially resolved chemistry is a concrete, attainable goal.

At a conference, I once heard a rallying cry of "Still not enough" when researchers attempted to explain submolecular resolution with regards to the enhancement needed. Traditionally, one can describe the overall enhancement achieved by TERS by first considering the "lightning rod" effect of the singularity of the STM tip apex. The quantification of this effect was first derived by Gersten and Nitzan; they concluded that ideal conditions would amplify the Raman scattered field by a factor of 10^2–10^3 [176]. A related enhancement mechanism occurs in TERS due to the strong spatial confinement of the localized surface plasmon (LSP). In a direct analogy to SERS, the external EM field of the laser couples to surface plasmons of the metal with dimensions less than the wavelength of light. The resultant plasmon resonance at the tip apex creates strong fields which amplify the scattered Raman field. To maximize the plasmon field at the junction, the LSP wavelength can be excited resonantly [177]. The overall enhancement of the Raman signal is proportional to the ratio of the near-field and far-field electric-field intensity to the fourth power. Overall, the EM mechanisms account for up to 10^{11} enhancement.

However, classical EM does *not* currently explain sub-nm resolved TERS, since the size of the plasmon, and therefore the extent the plasmon mode is localized under the tip, is roughly proportional to $\sqrt{2Rd}$ where R is the radius of curvature of the tip and d is the distance between the tip and the surface [178]. For a tip-sample distance of 1 nm (tunneling regime), and for a superbly sharp tip with $R = 10$ nm, the predicted resolution would be ≈ 4.5 nm. Indeed, 4 Å resolution based on this premise alone could be achieved if the tip were hovering 1 Å away from the surface, and had $R = 1$ nm. Alternatively, one could keep $d = 1$ nm in order to not damage the molecule, and sharpen the tip such that $R = 1$ Å. Either one would need an unreasonably sharp tip, or be stabbing the molecule with the tip in order to achieve the reported resolution.

For simple Raman visibility of a single molecule, classical EM is sufficient. However, without a quantitative working model for spatially-resolved TERS, the single molecule TERS community is now trying to fill in gaps with theory and other experimental findings to pinpoint the physical mechanism by which this occurred. The major theoretical thrust undertaken by Aizpurua and his group proposes that a single atom, potentially on the STM tip, at cryogenic temperatures may produce a so-called picocavity, in which light is further localized to a 1 nm region. They claim that quantum electrodynamics, not classical electrodynamics, is the key to resolving the dynamics of individual bonds.

In the latest set of experiments, CoTPP (cobalt (II) tetraphenylporphyrin) was dosed along with BPE (bipyridyl ethylene) on Au(111). The goal was to axially coordinate BPE with the cobalt atom, which would serve as a flag in both STM image and in its spectral signature. Trajectories show fluctuations in both intensity and wavenumber, which is not unprecedented for single or few-molecule experiments [179], nor particularly surprising to us. At this juncture, dosing conditions for both BPE and CoTPP were unoptimized, which rendered the STM topographies unable to pinpoint from which molecule the Raman signal came from. In a strange turn of events, it was within this nebulous experimental regime that we captured spatially-dependent Raman spectra with nanometer resolution.

In another twist, Raman trajectories and maps also exhibited overtones and combination bands. Typically, higher order Raman processes are present only under resonant conditions, when the incident wavelength is the same as an electronic transition. Transitions from $v = 0 \rightarrow v = 1$ are fundamental transitions, and from $0 \rightarrow n$, $(n > 1)$ are overtones. Combination bands occur when two or more fundamental vibrations are simultaneously excited. Combination bands are also subject to symmetry requirements [117].

In 1968, Koningstein published a theory of combination bands and overtones in the context of higher–order Raman processes [180]. The basis of his theory was the scattering Raman tensor due to vibronic coupling in the electronic waveunctions. The same effect on the depolarization ratio of resonant Raman intensities was similarly studied [181]. These early studies served as a jumping-off point for a quantitative evaluation of the intensities of fundamentals, overtone and combination bands in terms of the overlap of the time-dependent wave packet with the final Raman wave function as a function of time [182]. For our purposes, where it is unclear from which molecular or part of the molecule the spectrum arises, it is useful to look back on what group theory predicts. The excitation profiles of combination and overtones of CuTPP (same symmetry group D_{4h} as CoTPP) while under Q-band resonance were fully explained and assigned by Aramaki [183]. Interestingly, combination bands appear much more intense than the fundamentals in this work, a pattern which we also observe periodically.

How surface-enhancement mechanisms alter combination bands was studied as early as 1985 [184]. Initially, the appearance of combination bands in nonresonant molcules was explained by a similar charge transfer mechanism used to explain the enhancement itself. Charge transfer between the surface and molecule created a real excited state, which would in turn allow for evolution of the time-dependent wavepack. How SERS affects electronic resonances was studied using nickel (II) porphine [185]. For the resonant case, single molecule SERRS of perylenetetracarboxylic diimides (PTCD) in Langmuir-Blodgett films found similar depolarization ratios, but background contributions from the silver substrate prohibited exact isolation of single molecule spectra [186]

5.2 Experimental details

We operated these experiments at LN_2 temperatures ($T = 80$ K) and at UHV ($P = 4 \times 10^{-11}$ torr). To prepare the tip (#31, for reference) we sputtered for 10 minutes at 80 V bias, and ramped the current from 14 to 10.5 μA using back-filled conditions (Appendix). We sputtered Au(111) for 5 minutes, biased at –1 kV, and finally annealed Au(111) at 605℃ (10-9 μA) for an hour. Next, we dosed CoTPP at 18.5℃ with a 5 second exposure. We annealed the entire sample at 3.5 A for 3 minutes. After baking the chamber for a day, we dosed BPE by holding the crucible at 100℃ and watching the pressure rise on the baratron. Two more rounds of CoTPP dosing at 190℃ and 200℃ respectively, and two more rounds of BPE at 118 and 120℃ for 10 minutes finish up the sample preparation. Both 532 nm and 633 nm cw lasers were used.

5.3 Key Observations

5.3.1 Experiment and theory/literature

An absorption spectrum of CoTPP in toluene ($\approx$ 1 mM) shows a Soret band at 410 nm and the broad Q bands at 530 nm. Our incident laser operates at 532 nm, so resonant mechanisms may be at play here. The absorption spectrum was taken with a Shimadzu UV-1700 absorption spectrometer. The spectrum of toluene was already subtracted in Figure 5.1.

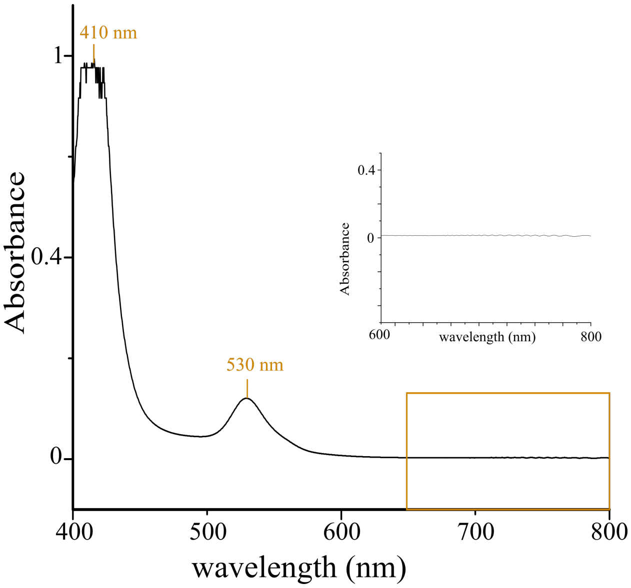

Figure 5.1: Absorption spectrum of 1mM Cobalt (II) tetraphenyl porphryin solution in toluene. The inset is a close up of the 650 - 800 nm region, which shows no features in the region where the second Q band is typically present.

In Figure 5.2, calculated and experimental spectra of CoTPP and BPE will serve as a guide for the Raman maps. I calculated the BPE spectrum using a B3LYP functional and 6-31G* basis set in Turbomole 7.1. The experimental BPE spectrum is part of a trajectory taken on Au(111). The CoTPP spectrum was taken by Domke and Pettinger [187]. Apparently, this spectrum also contains combination bands and overtones.

Figure 5.2: The spectrum of cobalt (II) tetraphenyl porphyrin (CoTPP) taken from Reference [187] is shown along with the calculated and experimental spectra of BPE (dashed and solid black respectively). The orange vertical lines correspond to the experimental wavenumber positions (in cm^{-1}): 976, 1184, 1019, 1524, 1552, 1594, 1610.

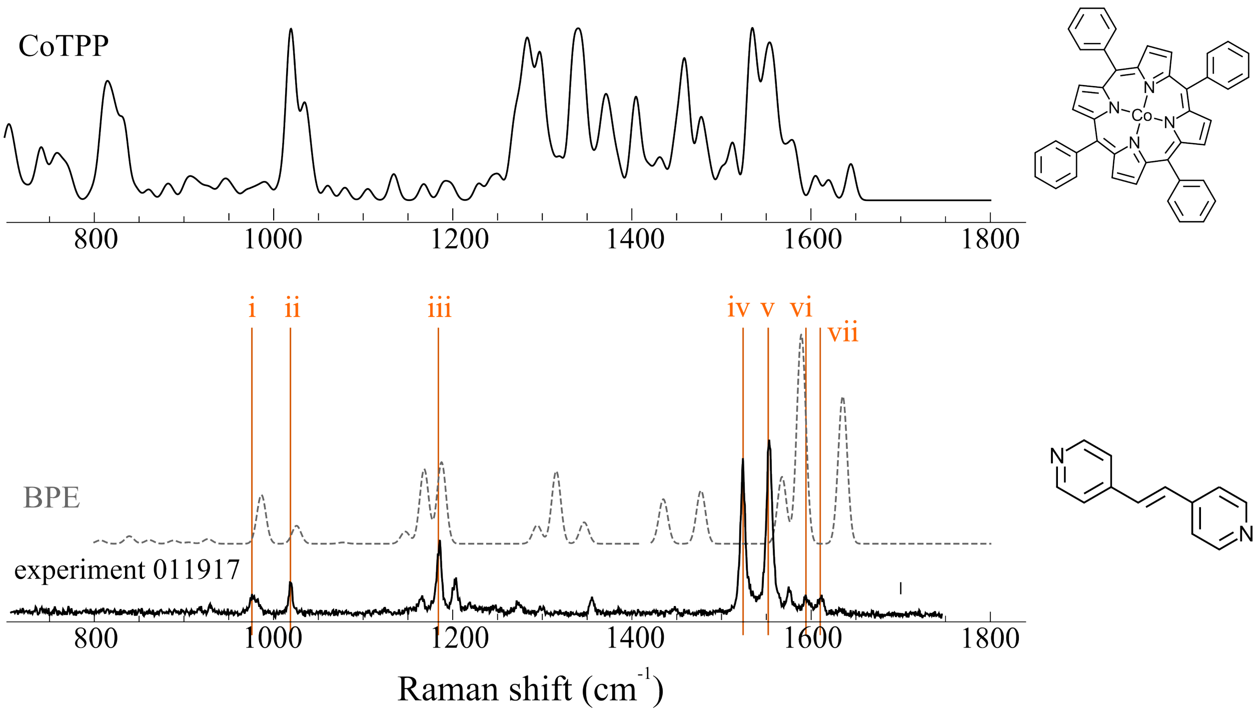

The strongest lines of BPE at 1524 and 1552 cm^{-1} appear blue–shifted in the calculated spectrum. Comparison of the grey and black spectra in Figure 5.2 show qualitative agreement in the $\sim$ 1500 cm^{-1} region and near 1200 cm^{-1}.

The spectrum in Figure 5.3(a) was taken where the red dot is shown in the corresponding STM image. There are no distinguishable molecular features in the image, but the spectrum is distinctly molecular. On a separate occasion, not much later, a distinct molecular spectrum was captured, along with three broad modes, and hints of combination bands and overtones, as detailed in the gray dashed lines in Figure 5.3(b). Once again, its accompanying STM image did not offer an immediate solution, even though unresolved features hint at a light covering of molecules. There is no record of where the tip was when the spectrum was recorded. The spectra and topographies were taken at I_t = 0.3 nA and V_B = 1.5 V. The topography in Figure 5.3(a) is 54 nm × 54 nm, whereas in (b) it is 108 nm × 108 nm, so the issue cannot be overall resolution.

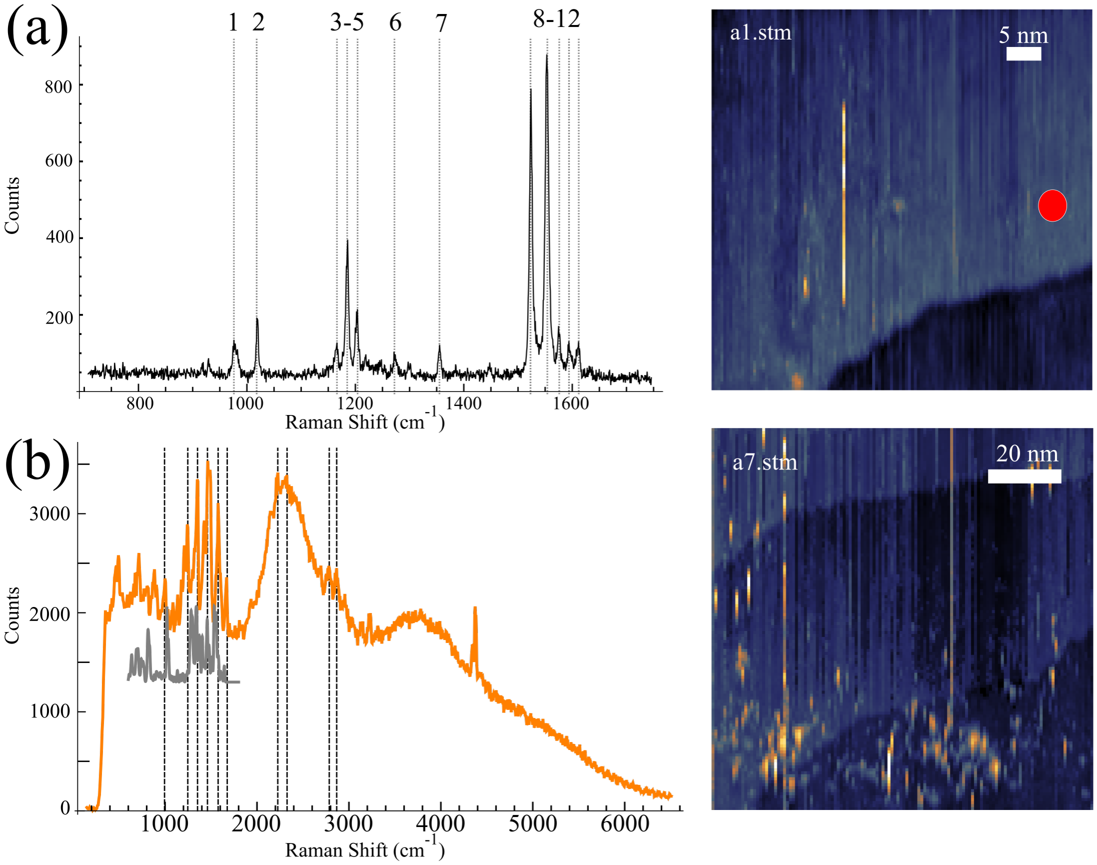

Figure 5.3: (a) BPE spectrum taken at the location of red dot. The peak positions labeled 1-12 are 976, 1018, 1166, 1185, 1204, 1272, 1355, 1523, 1554, 1576, 1594, 1612 cm^{-1} (b) CoTPP spectrum, without obvious molecular features in the STM topography. The peak positions labeled by the gray dashed lines are 994, 1247, 1353, 1461, 1577, 1676, 2226, 2327, 2786, 2867 cm^{-1}

5.3.2 Spatial resolution of Raman spectra

The distinct spectra also show a spatial variation. The STM images show areas with BPE spectra, and spectra with three broad modes. In Figure 5.4, the spectral variation is observed spatially varying over the STM topography. The Raman map is integrated over the entire spectrum, and is 64 × 64 Å, $V_b = 1$ V, and $I_t = 20$ pA.

The STM topography, while lacking the resolution to image the molecule, offers important clues, especially when combined with the Raman map. For six extracted spectra, the map shows that a BPE spectrum is confined to the right edge of the overall spectral intensity (Figure 5.4). We note that the spectra are taken only a few angstroms away from each other, but still contain significant differences in the low wavenumber region, highlighted below in Figure 5.4. This tells that we have spatial sensitivity on the order of a few angstroms.

In the map, the purple background are areas with no Raman signal, and match with the metal surface we have imaged. The more intense Raman signals seem to be localized to either side of a streak in the STM topography. The streak may be an artifact, or an actual break in the molecule.

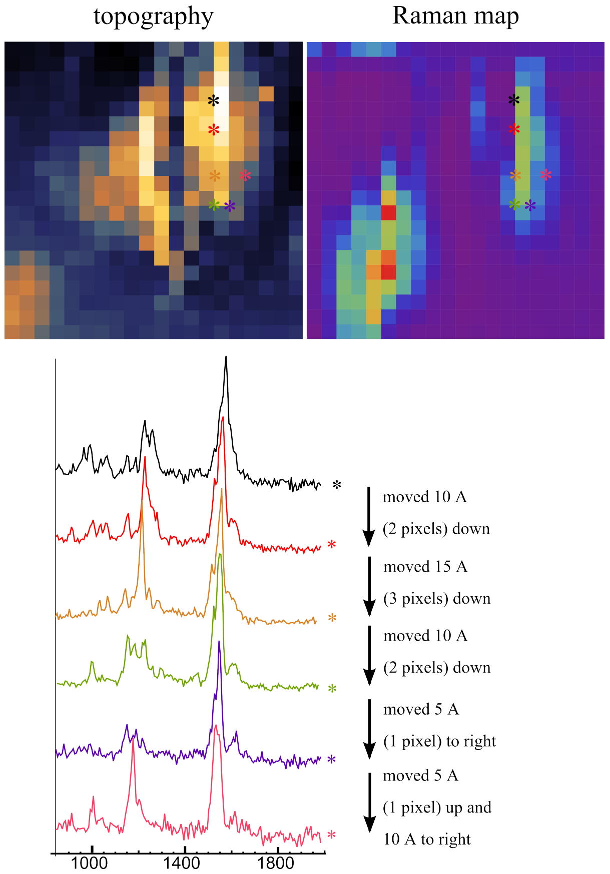

Figure 5.4: A single molecule is imaged with STM in the top left, and Raman in the top right. From where the six spectra were extracted are indicated with colored asterisks, and serve as the legend for the spectra below. To highlight the major spectral differences, only a portion of the Raman spectrum is plotted.

One may note the intense Raman activity seemingly located where the topography shows no molecule. In a distinct map, but in similar regions, very broad bands are observed while scanning over the pyrrole macrostructure. There appears to be two types of these broad mode spectra–one with peaks centered at 2204, 3360, and 4585 cm^{-1} (603, 645 and 703 nm, at 532 nm laser excitation), and one with two peaks around 2795 and 4113 cm^{-1}. Both types can shift up to 200 cm^{-1}. The physical mechanism prompting the rolling background is still under investigation. Like the molecular Raman spectra, the rolling background spectra vary spatially, with few-angstrom to nm resolution.

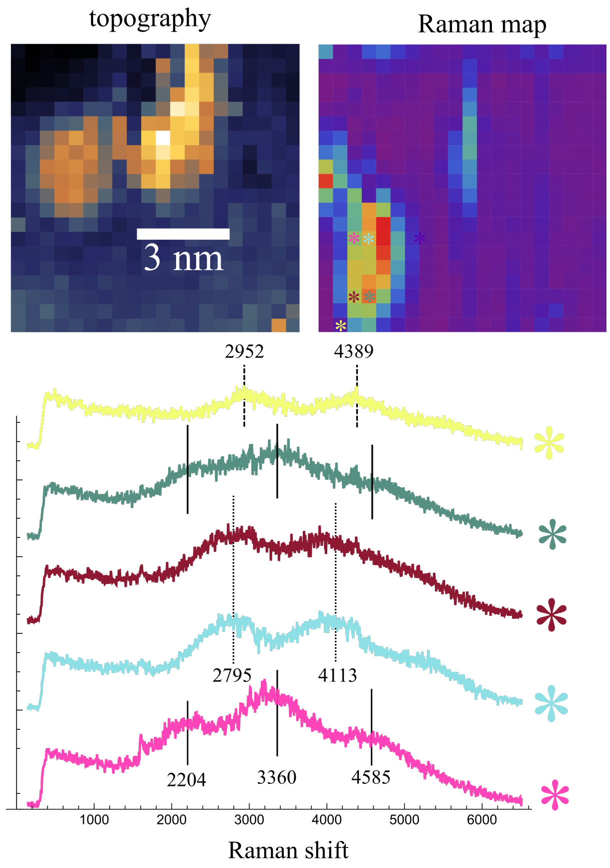

Figure 5.5: Similar map as Figure 5.4 with broad mode spectra extracted. The background also exhibits sub-nm spatial variation.

In the entire trajectory from which Figure 5.5 is extracted, these broad modes rise in and out of the spectrum. In other spectra, the rolling background heralds molecular Raman signal as well. To see if the intensity or positions of the molecular Raman are affected by the increase in the the rolling background, three consistent peaks were extracted corresponding roughly to the 2204, 3360, and 4585 cm^{-1} modes. The intensity of this peak is linear with the background. Further, the integrated intensity of a separate peak at 857 cm^{-1} is is also linear with the integrated intensity of the broad modes. Clearly, the background modes somehow enhance the overall and integrated molecular peaks. This observation is notable due to the missing puzzle piece in spatially resolved TERS. The fact that the background heralds the molecular spectra, and enhance its intensity, is worth further investigation.

5.3.3 Combination and overtone bands of CoTPP/BPE

During the Raman maps, combination and overtones are also observed. For CoTPP, we may expect to see combination bands since 532 nm is resonant with the molecule. However, BPE is nonresonant at these wavelengths, so we need to invoke another mechanism for creating a real excited state. Assigning the bands and noting their deviations from expected arithmetic (anharmonicities) will help us establish the governing selection rules for this peculiar system.

For the simplest case where two states are excited simultaneously, one expects to see the two fundamental bands corresponding to $\Delta\nu = \pm 1$ for both states, and all the combinations of ν_1 and ν_2: $2\nu_1$, $\nu_1 + \nu_2$, and $2\nu_2$. We see this case when mapping over a BPE molecule. In most cases, two very strong fundamental bands are seen, with various others with fluctuating intensities. The less intense modes tend to meander (Figure 5.4). A triplet appears in the overtone region. This triplet mirrors the intensity ratio of the parent bands, evident in Figure 5.6(a).

Figure 5.6: (a) Combination bands are present and observed when scanning and measuring over the molecule CoTPP/BPE over a 300 BLZ grating. The dashed gray lines correspond to (i) $\nu_1 = 1151$, (ii) $\nu_2 = 1544$, (iii) $2\nu_1 = 2302$, (iv) $\nu_1 + \nu_2 = 2676$, (v) $2\nu_2 = 3040$. (b) Broad modes taken over the TPP part of the ligand-molecule complex. The gray dashed line in this series correspond to (i)2302cm^{-1} (610 nm), (ii) 3507 cm^{-1} (656 nm), (iii) 4712cm^{-1} (710 nm).

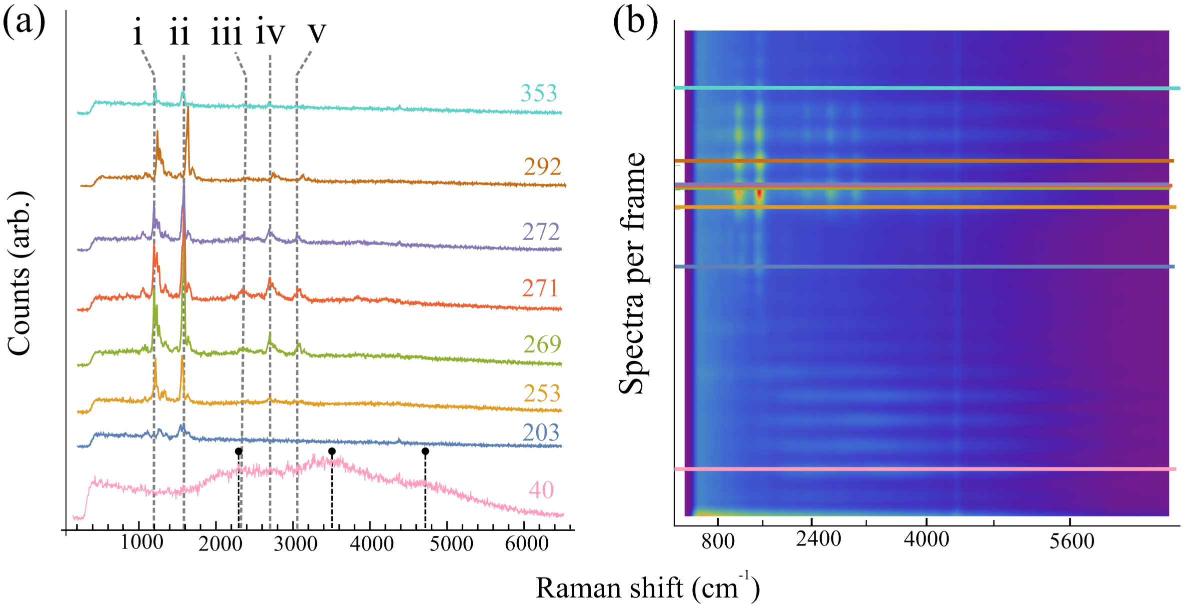

Evidently, the broad modes once again herald the molecular spectra, but in this case, there is no rolling background.

There are also stationary (*i.e.* not scanning or mapping simultaneously) Raman trajectories that contain combination bands and overtones. In one instance, a straightforwardly assignable spectrum emerges (Figure 5.7(a)). The assignments and anharmonic shifts are contained in Table 5.1. Comparison to Table 5.2 shows that the spectra easily identified with two fundamental bands and their combination bands/overtones have anharmonicities that appear fairly consistent. This observation remains true even for the maps where the tip scans over the molecule. We must also recall that combination bands and overtones tell us slightly different things. Because overtones constitute transitions $\Delta\nu = 2$, their deviations from the calculated line positions tell us about the extent how far the potential deviates from a true parabolic potential. Thus, we may surmise that the combination bands/overtones are due to vibrational anharmonicity, not to a nonlinear dipole or polarizability, or an electronic change the molecule may experience in the tip-sample junction.

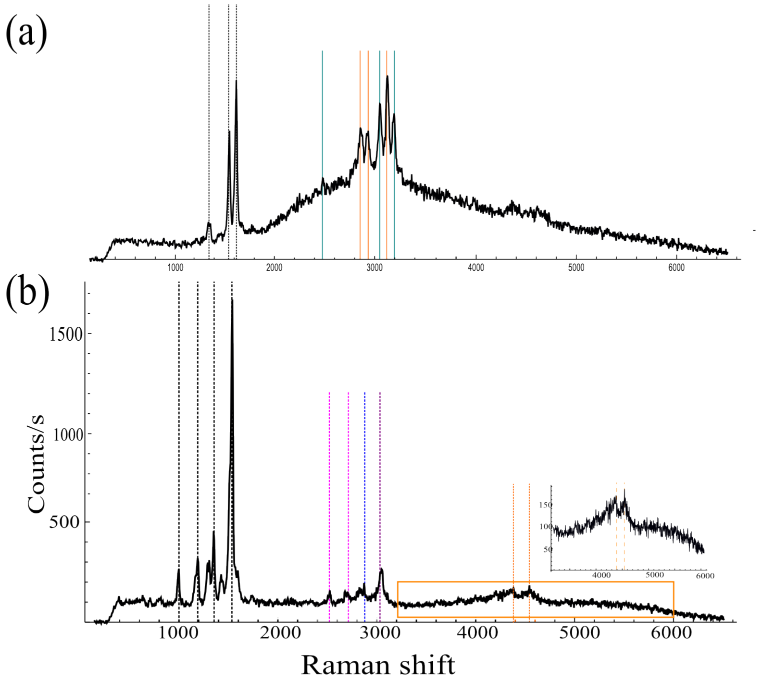

Figure 5.7: Combination bands and overtones for two spectra: one is straightforward, the other appears to implicate a rigid coupling to the strongest fundamental

There are several spectra and trajectories that show a more complicated spectrum than captured in the maps. These spectra also exhibit all combinations of the fundamental peaks.

In certain cases, not all the fundamentals are seen due to the low intensity and relatively low SNR. The complication arises from the fact that the combination band/overtone region can also be explained by each fundamental combining with the strongest mode at 1535 cm^{-1}. This interpretation is less straightforwards, as it indicates a rigid coupling to the most intense mode. It would be an interesting exercise to use a local-mode coordinate approach, often used for highly vibrational excited molecules, to calculate the spectrum [188, 189]. The assignments and their anharmonicities for both cases are contained in Table 5.1.

Table 5.1: Tabulated line positions and anharmonicities for spectra in Figure 5.7

Spectrum (Figure 5.7	Line assignment	Experimental line position	Calculated line position	Difference (anharmonicities)
(a)	a	1332	–	–
	b	1556	–	–
	c	1622	–	–
	2a	2513	2664	151
	a+b	2838	2888	47
	a+c	2902	2954	52
	2b	3050	3112	62
	b+c	3120	3178	58
	2c	3196	3244	48
(b)	1	1000	–	–
	2	1190	–	–
	3	1355	–	–
	4	1535	–	–
	2 + 3 (1 + 4)	2522	2545 (2535)	23 (13)
	3 + 3 (2 + 4)	2713	2710 (2725)	3 (12)
	3 + 4	2878	2890	12
	4 + 4	3031	3070	39
	3 + 4 + 4	4396	4425	29
	4 + 4 + 4	4540	4605	65

The following table summarizes the findings from the first data set where the combination bands appeared. The columns marked “trajectory” were taken with a stationary tip and those marked “maps” denote spectra extracted from Raman maps. We also find that there are three instances with a negative anharmonicity in Table 5.2 (*i.e.* a measured combination band that is slightly higher in wavenumber than the calculated line position), but considering that there is appreciable noise in some of the spectra, these instances should not be unduly weighted in the view of such extensive data that shows a more consistent picture. In any case, a negative anharmonicity is explained by a quartic instead of a cubic term in the potential energy surface. Where an overtone or combination band repeats from spectrum to spectrum, the anharmonicity is regular. Again, this indicates an anharmonicity in the molecular potential, not one induced by the perturbative environment of the STM junction.

Table 5.2: Summarized tabulation of anharmonicities for extracted spectra from first data set.

Line position (calculated)	map	map	map	traj	traj	traj	traj	Anharmoniticies
a	1377	1223	1151	1392	1165	1148	1429	–
b	1595	1568	1544	1613	1530	1546	1588	–
2a	2741 (2686)	2404 (2446)	2302 (2302)	2760 (2784)	2310 (2330)	2288 (2296)	2888 (2858)	-55/42/0 24/20/8/-30
a+b	2938 (2972)	2758 (2791)	2676 (2695)	2977 (3005)	2670 (2695)	2674 (2694)	3017 (3017)	34/33/19 28/25/20/0
2b	3150 (3190)	3080 (3136)	3040 (3088)	3206 (3226)	3032 (3080)	3049 (3092)	3209 (3175)	40/56/48 20/48/43/-34

Here, a control experiment is proposed. If D_4h symmetry is assumed for CoTPP, then we know that the only Raman active vibrations belong to the a_{le}, a_{2g}, b_{1g}, b_{2g}. In the case of the Q band resonance, only the in-plane electronic transitions Q and B can contribute to the vibrational Raman intensities. With this symmetry restriction, the depolarization ratios would immediately detail how the intensity of combination bands and fundamentals are correlated. Since Raman intensities in TERS geometries have a variety of confounding variables, this would be a difficult experiment, but can prove useful.

As is, the intensity information is not useful due to a SNR of 1.5:1. As a work-around, I averaged several frames from trajectories with appropriate error propagation in order to obtain a better SNR. However, this had to be done with care; in several trajectories, the tip was not stationary (*i.e* we were searching the STM surface for a more distinctive single

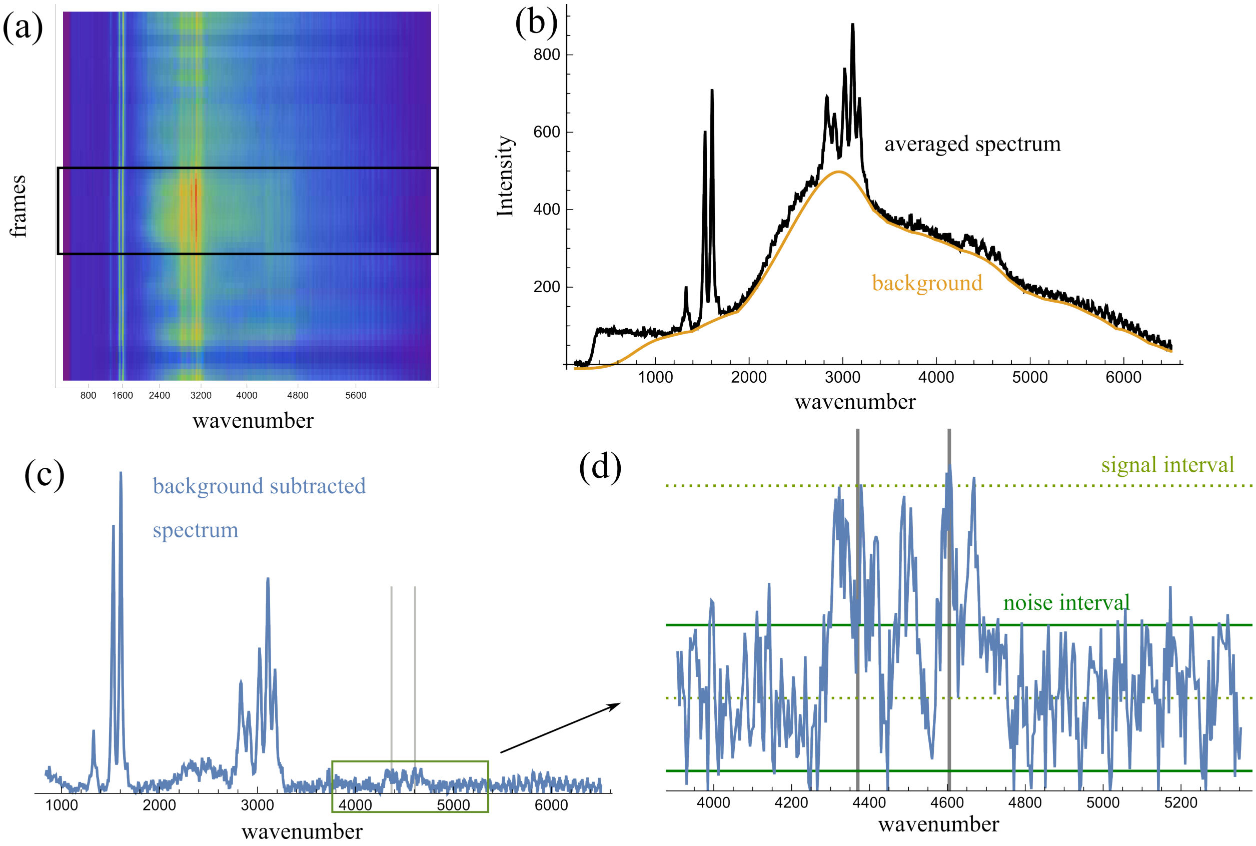

Figure 5.8: (a) A stable portion of a stationary Raman trajectory is averaged, (b) and the background (cavity spectrum) is subtracted in order to determine SNR in (c). (d) The $\Delta\nu = \pm 3$ region is zoomed in, and SNR is calculated to be as high as 2:1 and as low as 1.5:1

molecule signature), so frames could only be averaged where the tip was in one location.

Unfortunately, this was still unable to recover a SNR $> 3:1$. Further experiments can be done with long accumulations to increase the SNR in the $\Delta\nu = \pm 3$ region, which would allow the anharmonic shifts and its patterns more obvious. Whether the anharmonicities meander would also be a useful piece of the puzzle. To analyze this, several overtone regions are required, so the same averaging was used to obtain a better SNR in the 4000-6000 cm^{-1} region. In general, higher SNR spectra will answer many questions. A physical understanding of the rolling background, and of the governing selection rules for this peculiar case, may add another block of knowledge in the quest to understand the complexities of spatially resolved, single molecule dynamics.

Bibliography

[1] W. E. Moerner and L. Kador. Optical detection and spectroscopy of single molecules in a solid. *Physical Review Letters*, 62(21):2535–2538, 1989.

[2] W. P. Ambrose and W. E. Moerner. Fluorescence spectroscopy and spectral diffusion of single impurity molecules in a crystal. *Nature*, 349(6306):225–227, 1991.

[3] W. E. Moerner. A dozen years of single-molecule spectroscopy in physics, chemistry, and biophysics. *Journal of Physical Chemistry B*, 106(5):910–927, 2002.

[4] Chris Groves, Obadiah G. Reid, and David S. Ginger. Heterogeneity in Polymer Solar Cells: Local Morphology and Performance in Organic Photovoltaics Studied with Scanning Probe Microscopy. *Accounts of Chemical Research*, 43(5):612–620, 2010.

[5] Rahul Roy, Sungchul Hohng, and Taekjip Ha. A practical guide to single-molecule FRET. *Nature Methods*, 5(6):507–516, 2008.

[6] X Zhuang, T. Ha, H. D. Kim, T. Centner, S. Labeit, and S. Chu. Fluorescence quenching: A tool for single-molecule protein-folding study. *Proceedings of the National Academy of Sciences of the United States of America*, 97(26):14241–4, 2000.

[7] Timothy D Craggs. Cool and dynamic: single-molecule fluorescence-based structural biology. *Nature Methods*, 14(2):123–124, 2017.

[8] David Z. Keifer and Martin F. Jarrold. Single-molecule mass spectrometry. *Mass Spectrometry Reviews*, pages 1–19, 2016.

[9] Jordanka Zlatanova and Kensal van Holde. Single-molecule biology: what is it and how does it work? *Molecular Cell*, 24(3):317–29, 2006.

[10] D.A. Long. *Raman Spectroscopy.* McGraw-Hill International Book Company, New York, 1977.

[11] Lawrence D Ziegler. On the difference between resonance Raman scattering and resonance fluorescence in molecules: an experimental view. *Accounts of Chemical Research*, 27(1):1–8, 1994.

[12] C. V. Raman. A new radiation. *Proceedings of the Indian Academy of Sciences - Section A*, 37(3):333–341, 1953.

[13] S.A. Soper, E.B. Shera, and J.C. Martin. Single-molecule detection of rhodamine 6G in ethanolic solutions using continuous wave laser excitation. *Analytical Chemistry*, 437(31):432–437, 1991.

[14] Tobias Guenther, Christoph Lienau, Thomas Elsaesser, Markus Glanemann, Vollrath Martin Axt, Tilmann Kuhn, Soheyla Eshlaghi, and Andreas D. Wieck. Coherent nonlinear optical response of single quantum dots studied by ultrafast near-field spectroscopy. *Physical Review Letters*, 89(5):057401, 2002.

[15] Erik M. H. P. van Dijk, Jordi Hernando, Juan-José García-López, Mercedes Crego-Calama, David N. Reinhoudt, Laurens Kuipers, María F. García-Parajó, and Niek F. van Hulst. Single-molecule pump-probe detection resolves ultrafast pathways in individual and coupled quantum systems. *Physical Review Letters*, 94(7):078302, 2005.

[16] X. S. Xie and J. K. Trautman. Optical studies of single molecules at room temperature. *Annual Review of Physical Chemistry, Vol 62*, 49(1):441–480, 1998.

[17] Lukasz Piatkowski, Esther Gellings, and Niek F. van Hulst. Broadband single-molecule excitation spectroscopy. *Nature Communications*, 7:10411, 2016.

[18] Lukasz Piatkowski, Nicolò Accanto, and Niek F. van Hulst. Ultrafast Meets ultrasmall: controlling nanoantennas and molecules. *ACS Photonics*, 3(8):1401–1414, 2016.

[19] Jordan M. Klingsporn, Matthew D. Sonntag, Tamar Seideman, and Richard P. Van Duyne. Tip-enhanced Raman spectroscopy with picosecond pulses. *The Journal of Physical Chemistry Letters*, 5:106–110, 2014.

[20] Matthew D. Sonntag, Jordan M. Klingsporn, Luis K. Garibay, John M. Roberts, Jon a. Dieringer, Tamar Seideman, Karl a. Scheidt, Lasse Jensen, George C. Schatz, and Richard P. Van Duyne. Single-Molecule Tip-Enhanced Raman Spectroscopy. *The Journal of Physical Chemistry C*, 116(1):478–483, jan 2012.

[21] Felix Benz, Mikolaj K. Schmidt, Alexander Dreismann, Rohit Chikkaraddy, Yao Zhang, Angela Demetriadou, Cloudy Carnegie, Hamid Ohadi, Bart de Nijs, Ruben Esteban, Javier Aizpurua, and Jeremy J. Baumberg. Single-molecule optomechanics in "picocavities". *Science*, 354(6313):726–729, 2016.

[22] M. Barbry, P. Koval, F. Marchesin, R. Esteban, A. G. Borisov, J. Aizpurua, and D. Sánchez-Portal. Atomistic near-field nanoplasmonics: Reaching atomic-scale resolution in nanooptics. *Nano Letters*, 15(5):3410–3419, 2015.

[23] Wenqi Zhu and Kenneth B Crozier. Quantum mechanical limit to plasmonic enhancement as observed by surface-enhanced Raman scattering. *Nature Communications*, 5:5228:1–8, 2014.

[24] Peter Liljeroth. Single-molecule chemistry: Knowing your neighbours. *Nature Chemistry*, 6(1):8–10, 2013.

[25] M Fleischmann, P.J. Hendra, and A.J. McQuillan. Raman spectra of pyridine adsorbed at a silver electrode. *Chemical Physics Letters*, 26(2):163–166, 1974.

[26] M. Grant Albrecht and J. Alan Creighton. Anomalously intense Raman spectra of pyridine at a silver electrode. *Journal of the American Chemical Society*, 99:5215–5217, 1977.

[27] David L. Jeanmaire and Richard P. Van Duyne. Surface raman spectroelectrochemistryPart I. Heterocyclic, aromatic, and aliphatic amines adsorbed on the anodized silver electrode. *Journal of Electroanalytical Chemistry*, 84(1):1–20, 1977.

[28] Bernardo Laks and D. Mills. Photon emission from slightly roughened tunnel junctions. *Physical Review B*, 20(12):4962–4980, dec 1979.

[29] Frederick W. King, Richard P. Van Duyne, and George C. Schatz. Theory of Raman scattering by molecules adsorbed on electrode surfaces. *The Journal of Chemical Physics*, 69(10):4472, 1978.

[30] Craig S. Allen and Richard P. Van Duyne. Orientational specificity of Raman scattering from molecules adsorbed on silver electrodes. *Chemical Physics Letters*, 63(3):455–459, 1979.

[31] George C. Schatz and Richard P. Van Duyne. Image field theory of enhanced Raman scattering by molecules adsorbed on metal surfaces detailed comparison with experimental results. 101:425–438, 1980.

[32] G. Pofahl, J. Barthelmes, and W. Plieth. A pH-dependent surface-enhanced Raman spectroscopy investigation of the adsorption of 3-acetylpyridine. *Journal of Electroanalytical Chemistry*, 329(1-2):329–338, 1992.

[33] George C. Schatz and Richard P Van Duyne. Electromagnetic Mechanism of Surface-enhanced Spectroscopy. *Surface-enhanced Vibrational Spectroscopy*, pages 1–16, 2002.

[34] H. Ueba, S. Ichimura, and H. Yamada. Where are we in the study of SERS? Role of chemisorption and charge transfer. *Surface Science*, 119(2-3):433–448, 1982.

[35] Tamitake Itoh, Kenichi Yoshida, Vasudevanpillai Biju, Yasuo Kikkawa, Mitsuru Ishikawa, and Yukihiro Ozaki. Second enhancement in surface-enhanced resonance Raman scattering revealed by an analysis of anti-Stokes and Stokes Raman spectra. *Physical Review B*, 76(8):085405, 2007.

[36] P. F. Liao. Lightning rod effect in surface enhanced Raman scattering. *The Journal of Chemical Physics*, 76(1):751, 1982.

[37] Martin Moskovits. Surface-enhanced spectroscopy. *Reviews of Modern Physics*, 57(3):783–826, 1985.

[38] John Wessel. Surface-enhanced optical microscopy. *Journal of the Optical Society of America B*, 2(9):1538, 1985.

[39] Uzi Landman and W. D. Luedtke. Nanomechanics and dynamics of tip-substrate interactions. *Journal of Vacuum Science & Technology B: Microelectronics and Nanometer Structures*, 9(2):414, 1991.

[40] J. U. Ahamed, S. Katano, and Y. Uehara. STM-induced light emission from vacuum-evaporated gold film. *Bulletin of Materials Science*, 38(5):1271–1276, 2015.

[41] Jens Steidtner and Bruno Pettinger. High-resolution microscope for tip-enhanced optical processes in ultrahigh vacuum. *Review of Scientific Instruments*, 78(10), 2007.

[42] Raoul M. Stöckle, Yung Doug Suh, Volker Deckert, and Renato Zenobi. Nanoscale chemical analysis by tip-enhanced Raman spectroscopy. *Chemical Physics Letters*, 318(1-3):131–136, 2000.

[43] Aeneas Wiener, Antonio I. Fernández-Domínguez, Andrew P. Horsfield, John B. Pendry, and Stefan A. Maier. Nonlocal effects in the nanofocusing performance of plasmonic tips. *Nano Letters*, 12(6):3308–14, 2012.

[44] J. Aizpurua, S. Apell, and R. Berndt. Role of tip shape in light emission from the scanning tunneling microscope. *Physical Review B*, 62(3):2065–2073, 2000.

[45] Mengtao Sun, Yurui Fang, Zhilin Yang, and Hongxing Xu. Chemical and electromagnetic mechanisms of tip-enhanced Raman scattering. *Physical Chemistry Chemical Physics*, 11(41):9412–9419, 2009.

[46] D. Richards, R. G. Milner, F. Huang, and F. Festy. Tip-enhanced Raman microscopy: Practicalities and limitations. *Journal of Raman Spectroscopy*, 34(9):663–667, 2003.

[47] Sai Duan, Guangjun Tian, Yongfei Ji, Jiushu Shao, Zhenchao Dong, and Yi Luo. Theoretical modeling of plasmon-enhanced Raman images of a single molecule with subnanometer resolution. *Journal of the American Chemical Society*, 137(30):9515–9518, 2015.

[48] Katrin F. Domke, Dai Zhang, and Bruno Pettinger. Enhanced Raman spectroscopy: Single molecules or carbon? *The Journal of Physical Chemistry C*, 111(24):8611–8616, 2007.

[49] Yasuhiko Fujita, Peter Walke, Steven De Feyter, and Hiroshi Uji-i. Tip-enhanced Raman scattering microscopy: Recent advance in tip production. *Japanese Journal of Applied Physics*, 55(8S1):08NA02, 2016.

[50] G Binnig and H. Rohrer. Scanning tunneling microscopy. *Surface Science*, 126(126):236–244, 1982.

[51] C. Julian Chen. *Introduction to Scanning Tunneling Microscopy*. Oxford University Press, 1st edition, 1993.

[52] G. Meyer, B. Neu, and K. H. Rieder. Controlled lateral manipulation of single molecules with the scanning tunneling microscope. *Applied Physics A Materials Science & Processing*, 60(3):343–345, 1995.

[53] Björn Neu, Gerhard Meyer, and Karl-Heinz Rieder. Controlled vertical and lateral manipulation of single atoms and molecules with the scanning tunneling microscope. *Modern Physics Letters B*, 09(15):963–969, 1995.

[54] Ungdon Ham and Wilson Ho. Spin Splitting Unconstrained by Electron Pairing: The Spin-Vibronic States. *Physical Review Letters*, 108(10):106803, mar 2012.

[55] B. C. Stipe, M. A. Rezaei, and Wilson Ho. Coupling of vibrational excitation to the rotational motion of a single adsorbed molecule. *Physical Review Letters*, 81(6):1263–1266, 1998.

[56] Randall M. Feenstra. Scanning tunneling spectroscopy. *Surface Science*, 299-300:965–979, 1994.

[57] Paul K. Hansma and Jerry Tersoff. Scanning tunneling microscopy. *Journal of Applied Physics*, 61(2), 1987.

[58] Jerry Tersoff and D. R. Hamann. Theory of the scanning tunneling microscope. *Physical Review B*, 31(2):805–813, 1985.

[59] William Sacks. Tip orbitals and the atomic corrugation of metal surfaces in scanning tunneling microscopy. *Physical Review B*, 61(11):7656–7668, 2000.

[60] C. Bai. *Scanning tunneling microsopy and its applications*. Springer Verlag, New York, 2000.

[61] Catalin Neacsu, Jens Dreyer, Nicolas Behr, and Markus Raschke. Scanning-probe Raman spectroscopy with single-molecule sensitivity. *Physical Review B*, 73(19):193406, 2006.

[62] S. S. Kharintsev, G. G. Hoffmann, A. I. Fishman, and M. Kh. Salakhov. Plasmonic optical antenna design for performing tip-enhanced Raman spectroscopy and microscopy. *Journal of Physics D: Applied Physics*, 46(14):145501, 2013.

[63] Andreas Velten, Ramesh Raskar, Di Wu, Belen Masia, Adrian Jarabo, Christopher Barsi, Chinmaya Joshi, Everett Lawson, Moungi Bawendi, and Diego Gutierrez. Imaging the propagation of light through scenes at picosecond resolution. *Communications of the ACM*, 59(9):79–86, 2016.

[64] R. Schoenlein, L. Peteanu, R. Mathies, and C. Shank. The first step in vision: femtosecond isomerization of rhodopsin. *Science*, 254(5030):412–415, 1991.

[65] O. A. Smitienko, M. N. Mozgovaya, I. V. Shelaev, F. E. Gostev, T. B. Feldman, V. A. Nadtochenko, O. M. Sarkisov, and M. A. Ostrovsky. Femtosecond formation dynamics of primary photoproducts of visual pigment rhodopsin. *Biochemistry*, 75(1):25–35, 2010.

[66] Theodore H. Maiman. U.S. Patent 3353115 A, 1967.

[67] F. J. McClung and R. W. Hellwarth. Giant optical pulsations from ruby. *Journal of Applied Physics*, 33(3):828–829, 1962.

[68] A. J. Demaria, D. A. Stetser, and H. Heynau. Self mode-locking of lasers with saturable absorbers. *Applied Physics Letters*, 8(7):174–176, 1966.

[69] D. E. Spence, P. N. Kean, and W. Sibbett. 60-fsec pulse generation from a self-mode-locked Ti:sapphire laser. *Optics Letters*, 16(1):42, 1991.

[70] A. Baltuska, Z. Wei, M. S. Pshenichnikov, and D. A. Wiersma. Optical pulse compression to 5 fs at a 1-MHz repetition rate. *Optics Letters*, 22(2):102–104, 1997.

[71] Douglas Magde and Maurice W. Windsor. Picosecond internal conversion in crystal violet. *Chemical Physics Letters*, 24(1):144–148, 1974.

[72] T. L. Netzel, P. M. Rentzepis, and J. Leigh. Picosecond kinetics of reaction centers containing bacteriochlorophyll. *Science*, 182(4109):238–241, 1973.

[73] Ahmed H Zewail. Femtochemistry: Past, present, and future. *Pure and Applied Chemistry*, 72(12):2219–2231, 2000.

[74] Steven Yampolsky, Dmitry A. Fishman, Shirshendu Dey, Eero Hulkko, Mayukh Banik, Eric O. Potma, and V. A. Apkarian. Seeing a single molecule vibrate through time-resolved coherent anti-Stokes Raman scattering. *Nature Photonics*, 8(8):650–656, 2014.

[75] W. Kaiser, editor. *Ultrashort Laser Pulses: Generation and Applications.* Springer-Verlag, Berlin, 1993.

[76] Zhifeng Huang, Fang Chen, Roberto D'agosta, Peter A. Bennett, Massimiliano Di Ventra, and Nongjian Tao. Local ionic and electron heating in single-molecule junctions. *Nature Nanotechnology*, 2(11):698–703, 2007.

[77] Natalie L. Gruenke, M. Fernanda Cardinal, Michael O. McAnally, Renee R. Frontiera, George C. Schatz, and Richard P. Van Duyne. Ultrafast and nonlinear surface-enhanced Raman spectroscopy. *Chemical Society Reviews*, 45(8):2263–2290, 2016.

[78] W. Zhang, B.S. Yeo, T. Schmid, and R. Zenobi. Single molecule tip-enhanced Raman spectroscopy with silver tips. *Journal of Physical Chemistry C*, 111(4):1733–1738, 2007.

[79] A. V. Malkovskiy, V. I. Malkovsky, A. M. Kisliuk, C. A. Barrios, M. D. Foster, and A. P. Sokolov. Tip-induced heating in apertureless near-field optics. *Journal of Raman Spectroscopy*, 40(10):1349–1354, 2009.

[80] D. Ward, N. J. Halas, J. Ciszek, J. Tour, Y. Wu, P. Nordlander, and D. Natelson. Simultaneous measurement of electronic conduction and Raman response in molecular junctions. *Nano Letters*, 8:919–924, 2008.

[81] Daniel R. Ward, David A. Corley, James M. Tour, and Douglas Natelson. Vibrational and electronic heating in nanoscale junctions. *Nature Nanotechnology Letters*, 6:33–38, 2011.

[82] T.L. Cocker, Vedran Jelic, and Manisha Gupta. An ultrafast terahertz scanning tunnelling microscope. *Nature Photonics*, 7(8):620–625, 2013.

[83] T.L. Cocker, Dominik Peller, Ping Yu, Jascha Repp, and Rupert Huber. Tracking the ultrafast motion of a single molecule by femtosecond orbital imaging. *Nature*, 539(7628):263–267, 2016.

[84] Joonhee Lee, Shawn M. Perdue, Alejandro Rodriguez Perez, Patrick Z. El-Khoury, Karoliina Honkala, and V. A. Apkarian. Orbiting orbitals: visualization of vibronic motion at a conical intersection. *The Journal of Physical Chemistry A*, 117(46):11655–11664, 2013.

[85] Ivar Ugi, Dieter Marquarding, Hans Klusacek, Paul Gillespie, and Fausto Ramirez. Berry pseudorotation and turnstile rotation. *Accounts of Chemical Research*, 4(8):288–296, 1971.

[86] C. Alden Mead. Electronic spin-orbit interaction and the molecular Aharonov-Bohm effect. *Chemical Physics*, 49(1):33–38, 1980.

[87] Y. Aharonov and D. Bohm. Significance of electromagnetic potentials in the quantum theory. *Physical Review*, 115(3):485–491, 1959.

[88] Karen Johnston and Vagelis Harmandaris. Properties of benzene confined between two Au(111) surfaces using a combined density functional theory and classical molecular dynamics approach. *The Journal of Physical Chemistry C*, 115(30):14707–14717, 2011.

[89] Laura Rios, Joonhee Lee, Nicholas Tallarida, and V. Ara Apkarian. Hovering and twirling of tethered molecules by confinement between surfaces. *Journal of Physical Chemistry Letters*, 7(13):2461–2464, 2016.

[90] Evan J. Blackie, Eric C. Le Ru, and Pablo G. Etchegoin. Single-molecule surface-enhanced Raman spectroscopy of nonresonant molecules. *Journal of the American Chemical Society*, 131(40):14466–72, 2009.

[91] A. von Hippel. Molecular engineering. *Science*, 123(3191):315–317, 1956.

[92] Andrei Kolmakov and Martin Moskovits. Chemical sensing and catalysis by one-dimensional metal-oxide nanostructures. *Annual Review of Materials Research*, 34(1):151–180, 2004.

[93] Sara A. DiBenedetto, Irina Paci, Antonio Facchetti, Tobin J. Marks, and Mark A. Ratner. High-capacitance organic nanodielectrics: Effective medium models of their response. *The Journal of Physical Chemistry B*, 110(45):22394–22399, 2006.

[94] Reetu Raj Pandey, Minoru Fukumori, Amin TermehYousefi, Masanori Eguchi, Daisuke Tanaka, Takuji Ogawa, and Hirofumi Tanaka. Tuning the electrical property of a single layer graphene nanoribbon by adsorption of planar molecular nanoparticles. *Nanotechnology*, 28(17):175704, apr 2017.

[95] Avijit Kumar, Kaustuv Banerjee, and Peter Liljeroth. Molecular assembly on two-dimensional materials. *Nanotechnology*, 28(8):082001, feb 2017.

[96] Ayelet Vilan and David Cahen. Chemical modification of semiconductor surfaces for molecular electronics. *Chemical Reviews*, 117(5):4624–4666, 2017.

[97] Dmitri B. Strukov, Gregory S. Snider, Duncan R. Stewart, and R. Stanley Williams. The missing memristor found. *Nature*, 453(7191):80–83, 2008.

[98] I.A. Shanks. Liquid-crystal displays: an established example of molecular electronics. *IEE Proceedings I Solid State and Electron Devices*, 130(5):198, 1983.

[99] Kun Peng Dou and Chao-Cheng Kaun. Conductance switching of a phthalocyanine molecule on an insulating surface. *Frontiers of Physics*, 12(4):127303, 2017.

[100] Fekadu Gochole Aga, Jiyong Woo, Jeonghwan Song, Jaehyuk Park, Seokjae Lim, Changhyuck Sung, and Hyunsang Hwang. Controllable quantized conductance for multilevel data storage applications using conductive bridge random access memory. *Nanotechnology*, 28(11):115707, 2017.

[101] Ryuji Kawano, Nao Horike, Yuh Hijikata, Mio Kondo, Arnau Carné-Sánchez, Patrick Larpent, Shuya Ikemura, Toshihisa Osaki, Koki Kamiya, Susumu Kitagawa, Shoji Takeuchi, and Shuhei Furukawa. Metal-organic cuboctahedra for synthetic ion channels with multiple conductance states. *Chem*, 2(3):393–403, 2017.

[102] M. Reed, C. Zhou, C.J. Muller, T.P. Burgin, and J.M. Tour. Conductance of a molecular junction. *Science*, 278(5336):252–254, oct 1997.

[103] Y. Yang, J.-Y. Liu, Z.-B. Chen, J.-H. Tian, X. Jin, B. Liu, X. Li, Z.-Z. Luo, M. Lu, F.-Z. Yang, N. Tao, and Z.-Q. Tian. Conductance histogram evolution of an EC-MCBJ fabricated Au atomic point contact. *Nanotechnology*, 22(27):275313, 2011.

[104] Jiwoong Park, Abhay N. Pasupathy, and Jonas I. Goldsmith. Coulomb blockade and the Kondo effect in single-atom transistors. *Nature*, 417(722), 2002.

[105] J. Chen, M. A. Reed, A. M. Rawlett, and J. M. Tour. Large on-off ratios and negative differential resistance in a molecular electronic device. *Science*, 286(5444):1550–1552, 1999.

[106] Yasuhisa Naitoh, Tatsuhiko Ohata, Ryuji Matsushita, Eri Okawa, Masayo Horikawa, Makiko Oyama, Masakazu Mukaida, Dong F Wang, Manabu Kiguchi, Kazuhito Tsukagoshi, and Takao Ishida. Self-Aligned formation of sub 1 nm gaps utilizing electromigration during metal deposition. *ACS Applied Materials & Interfaces*, 5(24):12869–12875, 2013.

[107] Hongkun Park. Molecular electronics: Charges feel the heat. *Nature Materials*, 6(5):330–331, 2007.

[108] Amy S. Blum, James G. Kushmerick, David P. Long, Charles H. Patterson, John C. Yang, Jay C. Henderson, Yuxing Yao, James M. Tour, Ranganathan Shashidhar, and Banahalli R. Ratna. Molecularly inherent voltage-controlled conductance switching. *Nature Materials*, 4(2):167–72, 2005.

[109] R. Stephen Berry. Correlation of rates of intramolecular tunneling orocesses, with application to some Group V compounds. *The Journal of Chemical Physics*, 32(3), 1960.

[110] M. V. Berry. Quantal phase factors accompanying adiabatic changes. *Proceedings of the Royal Society A: Mathematical, Physical and Engineering Sciences*, 392(1802):45–57, 1984.

[111] S Pancharatnam. Generalized theory of interference, and its applications. *Proceedings of the Indian Academy of Sciences - Section A*, 44(5):247–262, 1956.

[112] H C Longuet-Higgins, U Opik, M H L Pryce, and R A Sack. Studies of the Jahn-Teller effect: The dynamical problem. *Proceedings of the Royal Society A: Mathematical, Physical and Engineering Sciences*, 244(1236):1–16, 1958.

[113] Joonhee Lee, Shawn M Perdue, Alejandro Rodriguez Perez, and V. A. Apkarian. Vibronic motion with joint angstrom-femtosecond resolution observed through Fano progressions recorded within one molecule. *ACS Nano*, 8(1):54–63, 2013.

[114] M. Jaeger, H. Kuhlenbeck, J. Freund, M. Wuttig, W. Hoffmann, R. Franchy, and H. Ibach. Formation of a well-ordered by oxidation of NiAl(110). *Surface Science*, 259:235–252, 1991.

[115] Martin Gouterman. Zero-field splitting of the triplet state in zinc etioporphyrin. *The Journal of Chemical Physics*, 56(8):4073, 1972.

[116] Brian M. Hoffman and Mark A. Ratner. Jahn-Teller effects in metalloporphyrins and other four-fold symmetric systems. *Molecular Physics*, 35(4):901–925, 1978.

[117] F. Albert Cotton. *Chemical Applications of Group Theory*. WILEYVCH Verlag Berlin GmbH, New York, 3rd edition, 1990.

[118] T. A. Jung, R. R. Schlittler, J. K. Gimzewski, H. Tang, and C. Joachim. Controlled Room-Temperature Positioning of Individual Molecules: Molecular Flexure and Motion. *Science*, 271(5246):181–184, 1996.

[119] A. Buldum, S. Ciraci, and S. Erkoc. Lateral translation of an Xe atom on metal surfaces. *Journal of Physics: Condensed Matter*, 7(45):8487–8496, 1995.

[120] A. Buldum and S. Ciraci. Controlled lateral and perpendicular motion of atoms on metal surfaces. *Physical Review B: Condensed matter*, 54(3):2175–2183, 1996.

[121] G.A. Somorjai. The molecular surface science of adhesion. In *First international Congress on adhesion science and technology*, pages 3–20, Leiden, 1998. VSP BV-C/O BRILL ACAD PUBL.

[122] Matthias Böhringer, Wolf-Dieter Schneider, and Richard Berndt. Scanning tunneling microscope-induced molecular motion and its effect on the image formation. *Surface Science*, 408(1-3):72–85, 1998.

[123] Matthias Böhringer, Karina Morgenstern, Wolf Dieter Schneider, and Richard Berndt. Reversed surface corrugation in STM images on Au(111) by field-induced lateral motion of adsorbed molecules. *Surface Science*, 457(1):37–50, 2000.

[124] Hyo Won Kim, M. Han, H.-J. Shin, S. Lim, Y. Oh, K. Tamada, M. Hara, Y. Kim, M. Kawai, and Young Kuk. Control of molecular rotors by selection of anchoring sites. *Physical Review Letters*, 106(14):146101, 2011.

[125] François Grey, Dehuan Huang, and Masakazu Aono. The sound of one atom hopping: Atomic manipulation on silicon surfaces by STM. *Philosophical Magazine Part B*, 70(3):711–720, 1994.

[126] Petra Tegeder. Optically and thermally induced molecular switching processes at metal surfaces. *Journal of Physics: Condensed Matter*, 24(39):394001, 2012.

[127] Karina Morgenstern. Switching individual molecules by light and electrons: From isomerisation to chirality flip. *Progress in Surface Science*, 86(5-8):115–161, 2011.

[128] M. J. Comstock, Jongweon Cho, A. Kirakosian, and M. F. Crommie. Manipulation of azobenzene molecules on Au(111) using scanning tunneling microscopy. *Physical Review B*, 72(15):153414, 2005.

[129] M. Wahl, M. Stöhr, H. Spillmann, T. A. Jung, and L. H. Gade. Rotation-libration in a hierarchic supramolecular rotor-stator system: Arrhenius activation and retardation by local interaction. *Chemical Communications*, 2(13):1349–1351, 2007.

[130] Gennaro Picardi, Marc Chaigneau, Razvigor Ossikovski, Christophe Licitra, and Guillame Delapierre. Tip enhanced Raman spectroscopy on azobenzene thiol self-assembled monolayers on Au(111). *Journal of Raman Spectroscopy*, 40(10):1407–1412, 2009.

[131] Ashleigh E. Baber, Heather L. Tierney, and E. C H Sykes. A quantitative single-molecule study of thioether molecular rotors. *ACS Nano*, 2(11):2385–2391, 2008.

[132] April D. Jewell, Heather L. Tierney, Ashleigh E. Baber, Erin V. Iski, Michael M. Laha, and E. Charles H. Sykes. Time-resolved studies of individual molecular rotors. *Journal of Physics: Condensed Matter*, 22(26):264006, 2010.

[133] Heather L. Tierney, Camilo E. Calderon, Ashleigh E. Baber, E. Charles H Sykes, and Feng Wang. Understanding the rotational mechanism of a single molecule: STM and DFT investigations of dimethyl sulfide molecular rotors on Au(111). *Journal of Physical Chemistry C*, 114(7):3152–3155, 2010.

[134] Bala Krishna Pathem, Shelley A. Claridge, Yue Bing Zheng, and Paul S. Weiss. Molecular switches and motors on surfaces. *Annual Review of Physical Chemistry*, 64:605–30, 2013.

[135] Dennis Lensen and Johannes A. A. W. Elemans. Artificial molecular rotors and motors on surfaces: STM reveals and triggers. *Soft Matter*, 8(35):9053, 2012.

[136] Tibor Kudernac, Nopporn Ruangsupapichat, Manfred Parschau, Beatriz Maciá, Nathalie Katsonis, Syuzanna R. Harutyunyan, Karl-Heinz Ernst, and Ben L. Feringa. Electrically driven directional motion of a four-wheeled molecule on a metal surface. *Nature*, 479(7372):208–211, 2011.

[137] Zhang Hai-gang, Mao Jin-hai, Liu Qi, and Jiang Nan. Manipulation and control of a single molecular rotor on Au (111) surface . *Chinese Physics B*, 19(1):018105, 2010.

[138] Tamar Seideman. Current-driven dynamics in molecular-scale devices. *Journal of Physics: Condensed Matter*, 15(14):R521–R549, 2003.

[139] Jongweon Cho, Niv Levy, Armen Kirakosian, Matthew J. Comstock, Frank Lauterwasser, Jean M. J. Fchet, and Michael F. Crommie. Surface anchoring and dynamics of thiolated azobenzene molecules on Au(111). *Journal of Chemical Physics*, 131(111), 2009.

[140] Bala Krishna Pathem, Yue Bing Zheng, John L. Payton, Tze-Bin Song, Byung-Chan Yu, James M. Tour, Yang Yang, Lasse Jensen, and Paul S. Weiss. Effect of tether conductivity on the efficiency of photoisomerization of azobenzene-functionalized molecules on Au(111). *The Journal of Physical Chemistry Letters*, 3(17):2388–2394, 2012.

[141] P. A. Thompson and S. M. Troian. A general boundary condition for liquid flow at solid surfaces. *Nature*, 389:360–362, 1997.

[142] Pil Seung Chung, Myung S. Jhon, and Hyoung Jin Choi. Molecularly thin fluoropolymeric nanolubricant films: tribology, rheology, morphology, and applications. *Soft Matter*, 12(11):2816–2825, 2016.

[143] J. V. Barth, H. Brune, G. Ertl, and R. J. Behm. Scanning tunneling microscopy observations on the reconstructed Au(111) surface: Atomic structure, long-range superstructure, rotational domains, and surface defects. *Physical Review B*, 42(15):9307–9318, 1990.

[144] Felix Hanke and Jonas Björk. Structure and local reactivity of the Au(111) surface reconstruction. *Physical Review B*, 87(23):235422, jun 2013.

[145] A. Kirakosian, M. J. Comstock, Jongweon Cho, and M. F. Crommie. Molecular commensurability with a surface reconstruction: STM study of azobenzene on Au(111). *Physical Review B - Condensed Matter and Materials Physics*, 71(11):1–4, 2005.

[146] Patrick Han, Brent A. Mantooth, E. Charles H. Sykes, Zachary J. Donhauser, and Paul S. Weiss. Benzene on Au{111} at 4 K: Monolayer growth and tip-induced molecular cascades. *Journal of the American Chemical Society*, 126(34):10787–10793, 2004.

[147] B. N. J. Persson and A. I. Volokitin. Electronic friction of physisorbed molecules. *The Journal of Chemical Physics*, 103(19):8679–8683, 1995.

[148] N. Pertaya, K.-F. Braun, and K.-H. Rieder. On the stability of Besocke-type scanners. *Review of Scientific Instruments*, 75(8):2608–2612, 2004.

[149] Erik R. McNellis, Christopher Bronner, Jörg Meyer, Martin Weinelt, Petra Tegeder, and Karsten Reuter. Azobenzene versus 3,3,5,5-tetra-tert-butyl-azobenzene (TBA) at Au(111): characterizing the role of spacer groups. *Physical Chemistry Chemical Physics*, 12(24):6404, 2010.

[150] Micol Alemani, Maike V. Peters, Stefan Hecht, Karl-Heinz Rieder, Francesca Moresco, and Leonhard Grill. Electric field-induced isomerization of azobenzene by STM. *Journal of the American Chemical Society*, 128:14446–14447, 2006.

[151] S.D. Evans, S.R. Johnson, and H. Ringsdorf. Photoswitching of azobenzene derivatives formed on planar and colloidal gold surfaces. *Langmuir*, 14(12):6436–6440, 1998.

[152] Yue Bing Zheng, John L. Payton, Choong-Heui Chung, Rong Liu, Sarawut Cheunkar, Bala Krishna Pathem, Yang Yang, Lasse Jensen, and Paul S. Weiss. Surface-enhanced Raman spectroscopy to probe reversibly photoswitchable azobenzene in controlled nanoscale environments. *Nano letters*, 11(8):3447–52, aug 2011.

[153] Hanne Jacob, Sandra Ulrich, Ulrich Jung, Sonja Lemke, Talina Rusch, Christian Schütt, Finn Petersen, Thomas Strunskus, Olaf Magnussen, Rainer Herges, and Felix Tuczek. Monitoring the reversible photoisomerization of an azobenzene-functionalized molecular triazatriangulene platform on Au(111) by IRRAS. *Physical Chemistry Chemical Physics*, 16(41):22643–50, 2014.

[154] Ali Safiei, Jörg Henzl, and Karina Morgenstern. Isomerization of an azobenzene derivative on a thin insulating layer by inelastically tunneling electrons. *Physical Review Letters*, 104:1–4, 2010.

[155] H. M. Dhammika Bandara and Shawn C. Burdette. Photoisomerization in different classes of azobenzene. *Chemical Society Reviews*, 41(207890):1809, 2012.

[156] Yasuo Norikane and Nobuyuki Tamaoki. Light-driven molecular hinge: A new molecular machine showing a light-intensity-dependent photoresponse that utilizes the trans-cis isomerization of azobenzene. *Organic Letters*, 6(15):2595–2598, 2004.

[157] Hiroto Murakami, Atsushi Kawabuchi, Rika Matsumoto, Takeshi Ido, and Naotoshi Nakashima. A multi-mode-driven molecular shuttle: Photochemically and thermally reactive azobenzene rotaxanes. *Journal of the American Chemical Society*, 127(45):15891–15899, 2005.

[158] Yasser M. Riyad, Sergej Naumov, Jan Griebel, Christian Elsner, Ralf Hermann, Katrin R. Siefermann, and Bernd Abel. Optical switching of azophenol derivatives in solution and in polymer thin films : The role of chemical substitution and environment. *American Journal of Nano Research and Application*, 2:39–52, 2014.

[159] Gayatri K. Joshi, Karl N. Blodgett, Barry B. Muhoberac, Merrell A. Johnson, Kimberly A. Smith, and Rajesh Sardar. Ultrasensitive photoreversible molecular sensors of azobenzene- functionalized plasmonic nanoantennas. *Nano Letters*, 14:532–540, 2014.

[160] Robert Turansky, Martin Konopka, Nikos L. Doltsinis, Ivan Stich, and Dominik Marx. Switching of functionalized azobenzene suspended between gold tips by mechanochemical, photochemical, and opto-mechanical means. *Physical Chemistry Chemical Physics*, 12(42):13922–13932, 2010.

[161] Jörg Henzl, Michael Mehlhorn, Heiko Gawronski, Karl-Heinz Rieder, and Karina Morgenstern. Reversible cis-trans isomerization of a single azobenzene molecule. *Angewandte Chemie International Edition*, 45(4):603–606, 2006.

[162] Zhong Fan Liu, Kenichi Morigaki, Tadashi Enomoto, Kazuhito Hashimoto, and Akira Fujishima. Kinetic studies on the thermal cis-trans isomerization of an azo compound in the assembled monolayer film. *The Journal of Physical Chemistry*, 96(4):1875–1880, 1992.

[163] N. Böhm, A. Materny, W. Kiefer, H. Steins, M. M. Müller, and G. Schottner. Spectroscopic investigation of the thermal cis-trans isomerization of Disperse Red 1 in hybrid polymers. *Macromolecules*, 29(7):2599–2604, 1996.

[164] Alessandro Cembran, Fernando Bernardi, Marco Garavelli, Laura Gagliardi, and Giorgio Orlandi. On the mechanism of the cis-trans isomerization in the lowest electronic states of azobenzene: S_0, S_1, and T_1. *Journal of the American Chemical Society*, 126(10):3234–3243, 2004.

[165] Eric Wei-Guang Diau. A new trans-to-cis photoisomerization mechanism of azobenzene on the S1(n,π*) surface. *The Journal of Physical Chemistry A*, 108(6):950–956, 2004.

[166] Luís Duarte, Rui Fausto, and Igor Reva. Structural and spectroscopic characterization of E- and Z-isomers of azobenzene. *Physical Chemistry Chemical Physics*, 16(32):16919–30, 2014.

[167] A. Biancalana, E. Campani, G. Domenico, and G. Gorini. Resonance Raman investigation of trans-azobenzene in the lowest Energy ^1A_u Excited State. *Journal of Raman Spectroscopy*, 24:43–52, 1993.

[168] Christina M. Stuart, Renee R. Frontiera, and Richard A. Mathies. Excited-state structure and dynamics of cis- and trans-azobenzene from resonance Raman intensity analysis. *Journal of Physical Chemistry A*, 111:12072–12080, 2007.

[169] A. L. Dobryakov, M. Quick, I. N. Ioffe, A. A. Granovsky, N. P. Ernsting, and S. A. Kovalenko. Excited-state Raman spectroscopy with and without actinic excitation: S_1 Raman spectra of trans-azobenzene. *The Journal of Chemical Physics*, 140(18):184310, 2014.

[170] H. Kumar Wickramasinghe, Marc Chaigneau, Ryohei Yasukuni, Gennaro Picardi, and Razvigor Ossikovski. Billion-fold increase in tip-enhanced Raman signal. *ACS Nano*, 8(4):3421–6, 2014.

[171] Martin Wolf and Petra Tegeder. Reversible molecular switching at a metal surface: A case study of tetra-tert-butyl-azobenzene on Au(1 1 1). *Surface Science*, 603(10-12):1506–1517, 2009.

[172] Eric C. Tyo and Stefan Vajda. Catalysis by clusters with precise numbers of atoms. *Nature Nanotechnology*, 10(7):577–588, 2015.

[173] X. H. Chen and M. Moskovits. Observing catalysis through the agency of the participating electrons: Surface-chemistry-induced current changes in a tin oxide nanowire decorated with silver. *Nano Letters*, 7(3):807–812, 2007.

[174] Jing Liu, Xiangyu Fu, Qiwei Chen, Yajie Zhang, Yongfeng Wang, Dahui Zhao, Wei Chen, Guo Qin Xu, Peilin Liao, and Kai Wu. Stabilizing surface Ag adatoms into tunable single atom arrays by terminal alkyne assembly. *Chemical Communications*, 52(88):12944–12947, 2016.

[175] R. Zhang, Y. Zhang, Z. C. Dong, S. Jiang, C. Zhang, L. G. Chen, L. Zhang, Y. Liao, J. Aizpurua, Y. Luo, J. L. Yang, and J. G. Hou. Chemical mapping of a single molecule by plasmon-enhanced Raman scattering. *Nature*, 498(7452):82–6, jun 2013.

[176] J. Gersten and A. Nitzan. Electromagnetic theory of enhanced Raman scattering by molecules adsorbed on rough surfaces. *Journal of Chemical Physics*, 73(7):3023, 1980.

[177] A. Kawata and V.M. Shalaev. *Tip enhancement*. Elsevier, Amsterdam, 2007.

[178] R. Rendell, D. Scalapino, and B. Mühlschlegel. Role of local plasmon modes in light emission from small-particle tunnel junctions. *Physical Review Letters*, 41(25):1746–1750, 1978.

[179] Matthew D. Sonntag, Dhabih Chulhai, Tamar Seideman, Lasse Jensen, and Richard P. Van Duyne. The origin of relative intensity fluctuations in single-molecule tip-enhanced Raman spectroscopy. *Journal of the American Chemical Society*, 135(45):17187–17192, 2013.

[180] J.A. Koningstein. Theory of Raman scattering for overtone and combination bands in the vibrational Raman effect. *Journal of Molecular Spectroscopy*, 28(3):309–315, 1968.

[181] J.A. Koningstein. Depolarization ratio of overtone and combination bands of the vibrational raman effect. *Chemical Physics Letters*, 2(1):31–32, 1968.

[182] Kyeong Sook Kim Shin and Jeffrey I. Zink. Quantitative evaluation of the relationships between excited-state geometry and the intensities of fundamentals, overtones, and combination bands in resonance Raman spectra. *Inorganic Chemistry*, 28(24):4358–4366, 1989.

[183] Shinji Aramaki, Liiro-O Hamaguchi, and Mitsuo Tasumi. Resonance Raman scattering with a forbidden but vibronically allowed electronic transition: Excitation profiles of combination and overtones of copper tetraphenylporphyrin in the Q-band resonance. *Chemical Physics Letters*, 96(5):555–559, 1983.

[184] Machiko Takahashi, Masatoshi Goto, and Masatoki Ito. Surface-enhanced Raman scattering of phenazine: Large intensities of overtones and combination bands. *Chemical Physics Letters*, 121(4-5):458–463, 1985.

[185] Xiao-Yuan Li, Vladimir I. Petrov, Dongming Chen, and Nai-Teng Yu. Surface-enhanced resonance Raman spectroscopy of water-insoluble Ni(II) porphine adsorbed on aqueous silver sol: suppression of antisymmetric scattering, antiresonance effect and higher order scattering. *Journal of Raman Spectroscopy*, 32(6-7):503–519, 2001.

[186] Paul J. G. Goulet, Nicholas P. W. Pieczonka, and Ricardo F. Aroca. Overtones and combinations in single-molecule surface-enhanced resonance Raman scattering spectra. *Analytical Chemistry*, 75(8):1918–1923, 2003.

[187] Katrin F. Domke and Bruno Pettinger. In situ discrimination between axially complexed and ligand-free Co porphyrin on Au(111) with tip-enhanced Raman spectroscopy. *ChemPhysChem*, 10(11):1794–1798, 2009.

[188] Bryan R. Henry. Use of local modes in the description of highly vibrationally excited molecules. *Accounts of Chemical Research*, 10(6):207–213, 1977.

[189] Xiaolu Cheng and Ryan P. Steele. Efficient anharmonic vibrational spectroscopy for large molecules using local-mode coordinates. *The Journal of Chemical Physics*, 141(10):104105, 2014.